# The Sonoelectrochemical Synthesis of Silver Nanoparticles and their Applications to SERS


Thesis submitted in accordance with the requirements of the University of Liverpool for the degree of Doctor in Philosophy

by

David R. Ritson

Under the supervision of

Prof. David Schiffrin

Department of Chemistry, University of Liverpool

July 2008

I hereby declare that this submission is my own work and that, to the best of my knowledge and belief, it contains no material previously published or written by another person nor material which to a substantial extent has been accepted for the award of an other degree or diploma of a university or other institute of higher learning, except where due acknowledgment is made in the text.

*David R Ritson*

# Acknowledgements

First and foremost I would like to thank my supervisor, Prof David Schiffrin, for offering me the opportunity to undertake this project. His continued enthusiasm and support when things were not going right (believe me their were a few!) and his constant faith in me over the years is greatly appreciated. It has been a privilege to work with him.

I would also like to thank the many members of the electrochemistry research group, past and present whom I have had the pleasure of working with, the knowledge and insight you have given me I shall take with me forever. A special thanks, however, goes to Iluiana for always having time for a chat and to be taught some Geordie phrases and to Stijn Mertens for his initial guidance all those many years ago.

Many thanks also goes to everyone I have worked with within the Chemistry Department at the University of Liverpool (each of you own a small part of this Thesis in your own special way). With a special thanks going to Anne Spencer, who made demonstrating bearable...what ever will you do now that I'm gone?! And to Chris Clay, for always being up for a coffee and for someone I could go and moan to when things weren't working.

I would also like to thank my friends, whom have been there with me every step of the way and were only ever a phone call or a car ride away to cheer me up or lend an ear. I love you all dearly. To Will and Phil, the best friends a guy could ever ask for.

Last but my no means least, I'd like to thank my Mam and my Sister for your unconditional love and faith in me. Both of you know more than anyone else the ups and downs I have been through over the past four years and I can say with my hand on my heart that without your support (both mental and financial) I would not be sat here writing this today. For this and many, many other reasons I love you both very much. And to my Dad, I only wish you were here to see this achievement...guess your boy done good!

*David R Ritson 2008*

## Abstract

Due to the unique ability of metallic nanoparticles to change their optical properties depending on their size and morphology there is an ever increasing need to not only discover new methods for their anisotropic synthesis but also to understand more fully the processes which lead to this shape directed growth.

The aim of this research was both the wet chemical and the electrochemical synthesis of metallic nanoparticles and nanorods for the construction of films appropriate for their use in Surface Enhanced Raman Spectroscopy in analytical applications. For this, a controlled nucleation and growth strategy coupled to ultrasonic pulses has been investigated. The kinetics of the electrochemical phase transformation of silver onto both platinum and glassy carbon along with the influence of pulse parameters on current density in varying conditions were systematically studied by means of cyclic voltammetry and potential step experiments. Nucleation and growth were controlled independently and electrodeposited small clusters were dislodged using an ultrasonic pulse at an appropriate time of the nucleation-growth sequence. Monodisperse silver nanoparticles of varing sizes stabilised by polyvinylpyrrolidone have been synthesised and were characterised by UV-Vis Spectroscopy and Transmission Electron Microscopy.

Gold nanorods with an average aspect ratio of $\sim$3 have been successfully prepared by a seed mediated surfactant stabilised method. The as-prepared gold nanorods were electrostatically bound to a gold substrate through the use of the linker molecule 11-mercaptoundecanoic acid followed by the chemisorbed deposition of the Raman active molecule, 4-mercaptobenzioc acid at various values of pH. Layer deposition was characterised by ellipsometry. A linear increase in the SERS signal has been observed for increasing values of pH.

The mechanism of anisotropic growth of silver particles in the surfactant cetyltrimethylammonium nitrate (CTAN) has been investigated by UV-Vis spectroscopy. With this change in the counter ion, which should allow the formation of soluble silver nitrate, no nanorod formation was observed. Also, the influence of $Br^-$ concentration within the cetyltrimethylammonium bromide (CTAB) growth solution was investigated. Although increasing the $Br^-$ concentration resulted in a large increase in the total concentration of free silver in solution, a gradual disappearance of the longitudinal plasmon band was observed indicating the favoured formation of spherical silver nanoparticles.

# Contents

# List of Figures

# List of Tables

# Chapter 1

# Introduction

*"Anybody who has been seriously engaged in scientific work of any kind realises that over the entrance to the gates of the temple of science are written the words: 'Ye must have faith.' "*

MAX PLANCK, 1858-1947

## 1.1 Motivation

The development of nanoscale science cannot be underestimated and has been at the forefront of pioneering research for many years, yet, the ability to easily and reproducibly synthesise nanoscale structures of well defined sizes and morphology still poses a continued challenge to scientists. Since Intel co-founder Gordon E. Moore observed that the computational power of most computer processors had doubled, on average, every 2 years since their initial production, later to be coined Moore's Law, there has been a concern that at some point this would cease to be a realistic target to maintain. This is mainly attributed to expected limitations in the ability to manufacture electronic components which are small enough to allow for this predicted growth. New fields such as nanolithography and nanoelectronics offer a real solution to this problem as well as numerous other applications such

as the treatment of cancer [1], cleaner and more efficient sources of fuel [2] and those related to environmental issues [3].

A variety of diverse methods have been developed to synthesise nanosized materials, details of which will be given later in this Chapter, along with factors concerning their stability and their applications in todays world.

## 1.2 Small Metal Particles

Although there is no fully accepted definition for the term 'nanoparticle' it is generally considered to be a particle having one or more dimensions of the order of 100nm or less. Due to their size being greater than a typical molecule but considerably smaller than bulk materials, nanoparticles exhibit unique optical properties [4] which are both size and shape dependant, details of which will be discussed later in the Chapter. A colloid is formed when one substance is dispersed evenly throughout another. Colloidal dispersions can take many forms, for example, a gas within a liquid forms a foam, whereas a liquid dispersed within a liquid forms an emulsion and a solid dispersed within a liquid forms a suspension or sol. It is the latter with which we will be concerned with in this study.

### 1.2.1 Synthesis

The first preparation of a colloidal metal sol is often attributed to the work of Michael Faraday in 1857 [5] in which he prepared a deep red solution of colloidal gold by the reduction of aqueous chloroaurate ($AuCl_4^-$) by phosphorus. The use of colloidal gold as a decorative aid can be traced back, however, as far as the Lycurgus Cup from Roman times.

Since the work of Faraday, significant advances have been made in colloidal synthesis. With a greater understanding of the fundamental chemistry behind their formation and considerable breakthroughs in scientific techniques, nanopa-

rticles can be fashioned from many materials and can now be made with a wide functional diversity.

#### 1.2.1.1 Nanoparticles

The most common and simplest approach to colloidal gold synthesis is the direct reduction of the metal salt $HAuCl_4^-$ by sodium citrate in aqueous solution, first reported by Frens [6]. In this preparation, the size of the nanoparticles formed can be controlled by simple adjustment of the gold:citrate ratio.

The synthesis of Au nanoparticles developed by Schiffrin-Brust [7] involves the stabilisation of gold cores by alkanethiols. In this two phase sythesis, the gold salt is transfered from an aqueous phase into toluene using the phase-transfer reagent tetraoctylammonium bromide. Gold is then reduced by sodium borohydride in the presence of thiols to yield 1.5 - 3 nm sized nanoparticles stabilised by a surface monolayer of alkanethiols, which have been called monolayer-protected clusters (MPCs). This reaction scheme is shown in Figure 1.1. For a self-assembled thiol monolayer on a flat gold surface, one thiol occupies approximately 0.2 $nm^2$ of the surface [8], however, due to the curvature introduced by the edges and vertices of a small particle, the coverage density is increased [9]. The number of atoms in the core tends to follow a closed shell structure with a truncated octahedral equilibrium shape [10].

Further development of this synthesis by Brust et al. has lead to the preparation of MPC's stabilised by a variety of different functional thiol ligands [11]. Analogous to the method reported by Frens, different size clusters can be prepared by varying the thiol:gold ratio, with larger thiol:gold mole ratios giving smaller average sized cores [10].

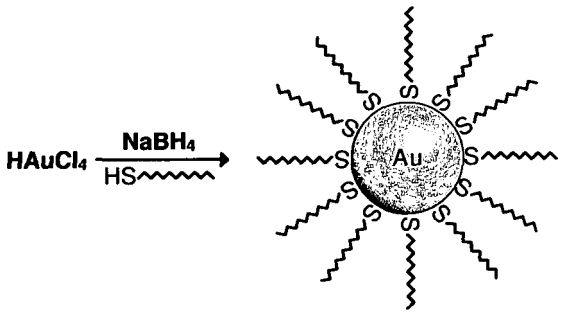


Figure 1.1: Formation of gold nanoparticles coated with organic shells by reduction of $Au^{III}$ compounds in the presence of thiols.

#### 1.2.1.2 Nanorods and Other Morphologies

The techniques and methods involved in the anisotropic formation of non-spherical nanoparticles are somewhat more complex than for spherical nanoparticles. Initial attempts at the synthesis of uniform metallic nanorods involved the use of an aluminium template which restricted the growth of the growing metal centres to one direction [12]. This technique, although very successful and reproducible, is laborious, involves a great deal of preparation and only allows for 1-D growth. Various other methods have been developed including electrochemical [13–15], photochemical conversion [16], microwave irradiation [17] and ultrasound (see Sections 1.3 and 1.4 for details).

However, the most widely used techniques employed in the formation of non-spherical nanoparticles involves the seed mediated growth of surfactant stabilised metallic nanorods. This approach, pioneered by the work of Jana, Gearheart and Murphy [18–25], involves the anisotropic growth of pre-formed metallic seeds within a growth solution. Typically, a metal salt of gold ($HAuCl_4$) or silver ($AgNO_3$) is initially reduced by a strong reducing agent such as sodium borohydride, to form small spherical seeds. These seeds are then added to a growth solution containing a mild reducing agent, more metal salts and, crucially, a high concentration of a surfactant. Although the exact mechanism for nanorod for-

mation is still not fully understood (see Chapter 4) the presence of the directing surfactant is critical to the synthesis of nanorods in a high yield [26]. The surfactant also chemisorbs upon the surface of the products formed leading to great stability. The benefit of this technique, for gold preparations, is its simplicity and reproducibility for producing uniform nanorods in high yield and under ambient conditions. Furthermore, by simply varying the synthesis parameters employed, a variety of sizes and shapes can be obtained, such as wires [18,21], dogbones [27], cubes [28] and triangular plates [29–31]. In contrast, silver does not behave in a similar way and preparations appear to be less reproducible.

A variety of other shape directing agents have been employed in the growth of non-spherical nanoparticles, such as PVP [32], DNA [33] and block copolymers [34].

### 1.2.2 Stability

In a bare state, nanoparticles are inherently thermodynamically unstable. With Brownian motion being the dominant force acting on a particle in a dispersion, theoretically, the dispersion should remain stable. However, due to their kinetic energy and attractive Van Der Waals forces, aggregation tends to occur. Therefore, to prevent this the particles must be stabilised in some way. This is usually achieved in two ways: electrostatically or sterically, as shown schematically in Figure 1.2.

Electrostatic stabilisation is achieved by the additions of a charged species, e.g. citrate [35] or a polyelectrolyte [36], which adsorbs onto the usually electrophilic surface of the metallic cluster, thus surrounding it with an electric double layer, Figure 1.2 (a). Hence, similarly charged particles will repel each other thus providing stabilisation in solution. Additionally, the functionality and charge of the electrostatically adsorbed species can bestow increased reactivity upon the MPC formed [37].

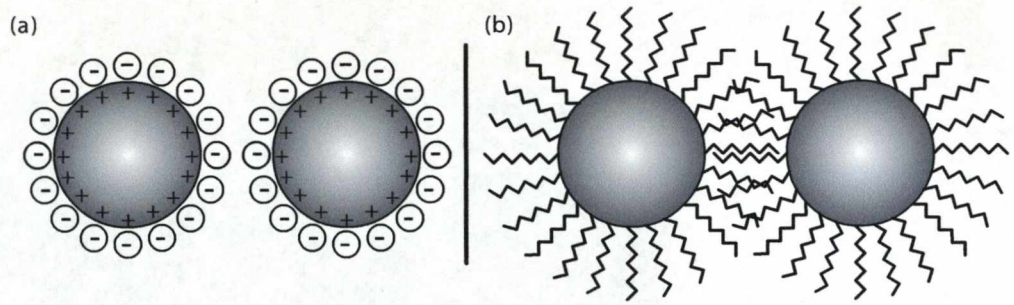


Figure 1.2: Schematic diagram showing the (a) electrostatic and (b) steric stabilisation of nanoparticles.

Steric stabilisation occurs through the use of sterically bulky ligands, such as polymers [38] or surfactants [39], bound to the surface of the metal centres. As interparticle distance decreases, the large adsorbates interweave creating a steric barrier which prevents the close contact of the metal cores, Figure 1.2 (b). This effect is entropically driven. With decreasing interparticle distance, the entropy decreases which in turn results in a increase in the Gibbs energy of the system, making their approach thermodynamically unfavorable.

In the synthesis of non-spherical nanoparticles the choice of surfactant has proved crucial in their formation [40–42]. Typically, the cationic surfactant cetyl trimethylammonium bromide (CTAB) is employed. Its role in anisotropic growth is discussed in greater detail in Chapter 4.

The surface composition of CTAB stabilised gold nanorods has been proposed to consist of a bi-layer structure with the cationic head group of the first CTAB monolayer facing the gold surface and the head group of the second layer in the aqueous solvent [43, 44]. Figure 1.3 shows the proposed bi-layer structure, where the straight black lines correspond to the long hydrophobic alkane chain and the green circles correspond to the hydrophilic cationic head.

This bi-layer formation is thought to be one of the main shape directing contributing factors in the anisotropic formation of the nanorods [44].

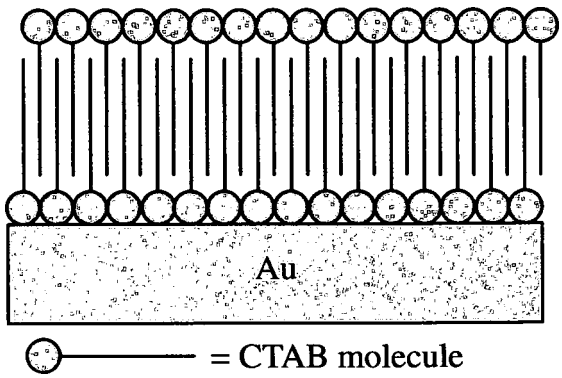


Figure 1.3: Scheme showing the CTAB bilayer structure on the surface of the synthesised gold nanorods.

### 1.2.3 Optical Properties

The optical properties of metals depend on their complex dielectric function. This is a physical quantity which describes how the polarisability of a material is affected by an electromagnetic field. In the case of solids, the complex dielectric function is closely related to their band structure. At an elementary level, electrons in a single atom occupy atomic orbitals, which form a set of discrete energy levels. As the number of atoms increases, forming a solid, their atomic orbitals overlap forming molecular orbitals, the number of which is proportional to the number of atoms. When we consider a large number of atoms, the number of energy levels is so large and the difference in energy between them so small, that we consider them as continuous energy bands. The periodic crystal lattice of a material defines the nature of its band structure.

For a metal, there is an overlap of valence and conduction bands which permits the continual movement of electrons, therefore leading to a very high conductivity. For semi-conductors and insulators a gap is present between the two bands, where fewer electrons are found, which effectively lowers their conductivity. Reducing the size of a material has a pronounced effect on the energy level spacing, and thus its optical properties, as the system becomes more confined. This reduction

in size to a nanoscale range results in the formation of a band gap between the valence and conductance bands for metallic nanoparticles.

In the seminal paper by Mie [45], a solution to Maxwell's equations, that describes the extinction spectra of spherical particles, was presented. This theoretical analysis of the extinction coefficient of small spherical nanoparticles in a solvent arises from scattering and absorption of light. However, when the core diameter is smaller than the wavelength of light, only absorption contributes to the extinction spectra. The absorption spectra of many metallic nanoparticles are characterised by a strong band that is absent in the spectra of the bulk material. When a spherical metallic nanoparticle is irradiated with light, the oscillating electromagnetic field causes an oscillation of the electrons in the conduction band of the particle. As the electron cloud is displaced, a restoring force arises between the electrons and the nuclei due to their coulombic attraction, which results in a collective oscillation of the electron cloud [46]. This leads to a specific and characteristic frequency at which the oscillations occur. This phenomenon is commonly referred to as a surface plasmon resonance. As particle size decreases the ratio of surface to core atoms increases and this goes someway to explaining why the position, the intensity and the width of the peaks in the spectra of small metal particles depend on the shape and size of the particles.

In 1915 Gans [47] extented Mie's original theory to cover the optical absorption spectra of prolate and oblate ellipsoids. In this model, the depolarisation factors along three axis A, B and C of the nanorod, where A<B=C, were considered, along with its aspect ratio [48]. Link and El-Sayed have performed a large amount of theoretical and experimental research on the optical properties of silver and gold nanorods [48–52] and based on the theoretical simulations and experimental TEM observations, found a linear relationship between the absorption maximum of the longitudinal plasmon resonance and the mean aspect ratio [53].

### 1.2.4 Applications

Nanomaterials are no longer merely limited to being a laboratory curiosity and have now reached a commercialised stage. This is apparent in the large number of companies which have been founded on the basis of many university based nanotechnological discoveries and their usefulness to everyday life will become increasingly apparent.

Probably one of the most important recent application of nanosized materials has been their role as a delivery agent for anti-cancer agents or as a source of concentrated and localised electromagnetic radiation. This has been achieved in a number of ways. Through the MRI directed delivery of superparamagnetic iron oxide nanoparticles functionalised by anti-cancer drugs Hanessian et al. [54] have observed increased specificity to regions of the body affected by tumor cells leading to more localised and focussed drug delivery. In a different approach, Cheng et al. [55] employed folate-conjugated gold nanorods monitored in real time by two-photon photoluminescence (TPL) microscopy. They were observed to be effective at inducing tumor cell necrosis when localized on the cell membrane through the resulting photothermal activity.

In the field of Surface Enhanced Raman Spectroscopy (SERS) both nanoparticles and nanorods have been employed to achieve extremely large degrees of Raman enhancement. This phenomenon was shown as early as 1982 where Lee at al. [56] observed a SERS spectra of various dyes dispersed in gold and silver hydrosols. However, it was Kneipp et al. [57] and Nie et al. [58] who first noticed that far greater enhancement was observed when molecules were attached to aggregates of large metal nanoparticles. With recent advances in experimental techniques, the detection of single molecules under optimised conditions when bound to an isolated nanoparticles surface is now possible [59–62]. The modification of metallic surfaces with immobilised nanoparticles has also been shown to give large enhancements [63–65]. Moreover, this has lead to the development

of various SERS based biophotonic sensors capable of determining such intricate biological parameters as intracellular pH [66] and DNA fragments [67] and the ability to detect simultaneously various biological components within a cell [68].

Various transition metal nanoparticles have also been successfully employed in many catalytic processes including the electrocatalytic oxidation of methanol [69], carbon monoxide [70] and glucose [71]. They are also proving to have huge applications in novel fuel cells [72–74].

### 1.2.5 Immobilisation and Assembly

The assembly of nanoparticles, either with respect to each other or to a surface, has important applications in various aspects of chemistry including catalysis, Surface Enhanced Raman Spectroscopy, nanoelectronics and electron transfer kinetics. The ability to create highly ordered, uniform structures is paramount and therefore, for this purpose, self assembled monolayers (SAMs) are excellent candidates. SAMs consist of a highly ordered single layer of molecules bound to a surface.

Glass substrates provide excellent surface functionality due to the formation of surface hydroxide groups upon acidic treatment. This, coupled with its low cost, makes glass a widely employed substrate for SAM formation. The hydroxylated surface is highly reactive to functionalised alkylsilanes, which form strong covalent Si-O-Si bonds [75]. Depending on the functionality of the alkylsilanes employed, the modified surface can then allow the adsorption of colloidal particles through either electrostatic interaction or covalent bonding, Figure 1.4 (a).

It is well-known that self-assembled monolayers (SAMs) can be formed from alkanethiols on the surface of gold [76–80]. Analogous to the self assembly of silanes discussed above, this method also involves the modification of a surface which can then be followed by the adsorption of colloidal particles by altering the functionality of the alkanethiol employed. This is shown schematically in

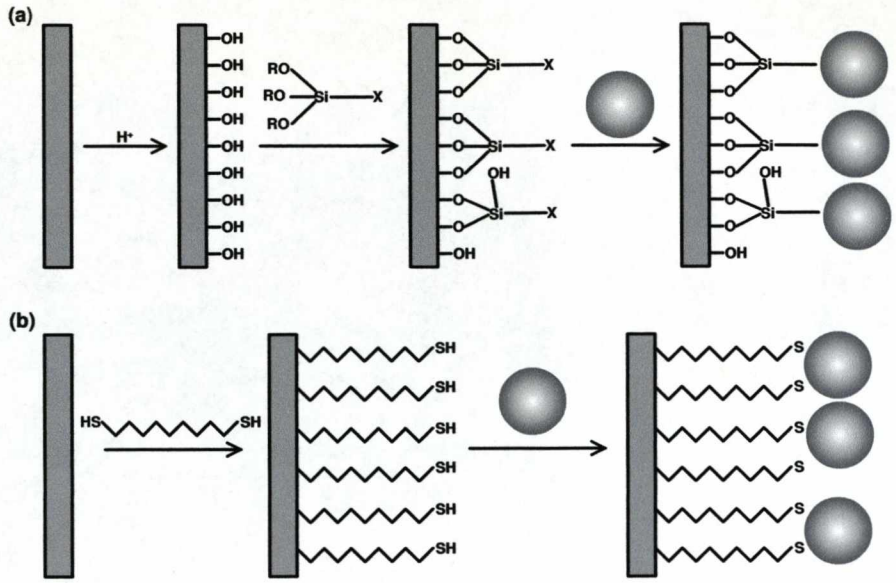


Figure 1.4: The construction of nanoparticle monolayers on (a) glass through the addition of alkylsilanes and (b) gold through the addition of alkanedithiols.

Figure 1.4 (b). The driving force for this assembly is the formation of a strong covalent bond between the sulphur of the thiol and the gold surface. The close packed alkanethiol SAM orientates itself at a 30° angle perpendicular to the gold surface [77].

Multilayer formation is also possible through the use of linker molecules, e.g. electrostatic polymers [81] or dithiols [82]. Dong et al. monitored, using UV-Vis spectroscopy, the multilayer formation of gold nanorods through electrostatic binding to charged polymers. Initially, an ITO substrate was modified with a positively charged polyelectrolyte and then subsequently treated with a negatively charged polymer. The cationic surfactant bound to the surface of the gold nanorods renders them positively charged and therefore, they easily self assemble due to strong electrostatic interactions. This process can be repeated until the desired number of multilayers is reached [81].

It is clear that, by careful control over the conditions employed and the functionality of the substrates and species used during the assembly of nanosized

materials, complex and specific nanostructured arrays can be obtained. This is expected to have great implications in nanoelectronics [83].

## 1.3 Sonochemistry

Sonochemistry refers to the field of research in which molecules undergo a chemical reaction in response to the application of ultrasonic irradiation. At specific frequencies,(20 kHz and 1 MHz), this radiation is capable of breaking strong covalent bonds. The fundamental principle on which sonochemistry is based is a process known as acoustic cavitation [84]. This phenomenon involves the creation, growth and eventual collapse of gas and vapour filled bubbles formed through high intensity ultrasonication of the surrounding medium. During the latter stage, the collapsing bubble concentrates the diffuse energy of sound and this compression generates heat. This heating occurs more rapidly then thermal diffusion in the surrounding liquid thus creating localised hot spots. Within these hot spots temperatures in excess of 5000 K, pressures of ~1000 atmospheres and heating and cooling rates above $10^{10}$ K/s can be found [84,85]. In addition, the subsequent rapid cooling hinders the reorganisation and recystallisation of the products formed. The extreme localised environments created by cavitation allows for high temperature, physical and chemical reactions to occur in otherwise ambient conditions of the bulk solution.

Ultrasound has been used in the synthesis of many different products. When dealing with volatile precursors, predominantly amorphous nanostructures are obtained. Whilst the formation of amorphous products can be well understood, due to the high heating and cooling rates, the formation of nanoparticles is not as clear. One possible explanation is that due to the small size of the microbubbles formed during cavitation, only a few nucleation centres can fit inside and their growth is limited by the bubble's short life cycle [86]. By simple control of the

surrounding medium and precursors employed, a variety of nanosized materials can be synthesised. Metallic nanoparticles of Fe [85], Ru [87], Au [88] and Ag [89] as well as metallic oxides such as $Fe_2O_3$ [90], $Cu_2O$ [91] and $TiO_2$ [92] have all been prepared under ultrasonic radiation. More recently, there has been considerable interest in the sonochemical synthesis of chalcogenides ($S^{-2}$, $Se^{-2}$ and $Te^{-2}$) [93–97] due to their semiconductor properties which have applications in photovoltaic cells and optical data storage devices [86].

One-dimensional nanostructures have also been synthesised successfully sonochemically. Nanorods of HgSe [93], CdS [98], Sn [99] and silver dendrites [89], as well as carbon [100] and $TiO_2$ [101] nanotubes have been reported but the method of each synthesis can differ greatly from ambient to extreme conditions. Whilst the exact mechanism of nanotube formation is still not fully understood, Zhu et al. [101] proposed for $TiO_2$ that during ultrasonication, small titanate nanosheets are created. Upon heating, these sheets grow in size and due to the stress caused by the extreme temperature and the reduction of the interlayer interaction at the edge of the sheet [86], they roll up to form nanotubules.

The mechanism by which nanorods are formed sonochemically is much simpler. Gendanken [86] proposed that, nanoparticles are formed initially which, under the microjets and shockwaves produced by the collapse of the bubbles formed by cavitation, are pushed towards each other and are then held by chemical forces. In the synthesis of $Sd_2S_3$ nanorods, Zhu et al. [102] suggested that the magnitude of the interparticle collisions of the initially produced nanoparticles, coupled with the extreme heat of the collapsing bubble induced effective melting at the point of collision leading to nanorod formation. Longer ultrasonication times increased the aspect ratio of the as-prepared nanorods. Xie et al. [103] reported the ultrasound assisted self-regulated preparation of Ag nanorods. In this method, 1,10-phenanthroline was employed as an anisotropic growth directing agent due to the formation of a stable square planar complex with $Ag^{2+}$ with steric hindrance on its

plane and thus a linear conformation is formed. The effect of acoustic streaming was sufficient to oxidise $Ag^{+}$ ions to $Ag^{2+}$ in the presence of oxygen. The complex was then reduced with a mild reducing agent in order to allow complete nanorod growth. The multidentate ligand EDTA has also been employed with ultrasound for the growth of CdS nanorods [98]

## 1.4 Sonoelectrochemistry

The coupling of electrochemistry with ultrasound, or sonoelectrochemistry, has became an important electroanalytical tool [104, 105]. Many homogeneous and hetrogeneous chemical reactions can be achieved electrochemically and therefore, in principle, enhanced by ultrasound. This allows the reaction occuring to be better understood and it is possible for them to be quantified [106]. The interaction of ultrasound with electrode processes is known to lead to enhanced reproducible voltammetric behaviour [107], increased mass transport of active species to the electrode surface [106], continual cleaning of the electrode [108], electrode degassing and increased reaction rates. The benefits of applying ultrasound has been observed in electroplating [107, 109], nanoparticle synthesis [25, 99, 108, 110, 111] and sonoelectroanalysis [104, 105, 112]. However, there are still inherent problems in using this technique due to the complexity of the processes induced by ultrasound.

Ultrasound has been employed in two very different ways in the synthesis of nanosized materials. As described in Section 1.3, when ultrasound is applied constantly throughout the preparation [113], the extreme environment caused by acoustic cavitation of the medium is such that small nuclei can be formed and under specific conditions, anisotropic growth can be observed. Control over size and morphology can be achieved, to a greater extent, by growing the nanoclusters electrochemically. In this approach, ultrasound is applied either constantly or in

short controlled bursts [91,114]. Reisse and co-workers [25,115,116] were the first to describe this novel method for the production of nanosized metallic powders using pulsed sonoelectrochemical reduction. Nuclei are first grown at the electrode surface by applying a current and this is immediately followed by a burst of ultrasonic energy which is used to physically dislodge the metal particles from the electrode. This not only cleans the electrode surface but also replenishes the solution layer immediately close to the electrode surface with electroactive species from the solution. An adaptation of this technique has been employed in the work carried out in this Thesis.

### 1.4.1 Electrode Geometry and Cell Design

To date several methods have been adopted for the introduction of ultrasound into an electrochemical cell. The simplest approach involves the immersion of the cell in an ultrasonic bath [15]. This can lead to a large distribution of ultrasonic power and significantly lowers the effective power delivered to the region of interest i.e, the electrode-solution interface. With current advances in technology the development of ultrasonic horns has allowed for highly focused and localised intense ultrasound to be applied to an electrode surface by placing it inside the electrochemical cell. In this configuration, the working electrode is located in close proximity to the ultrasonic horn and allows the ultrasonic intensity and the distance between the horn and the working electrode to be varied.

Three distinct working electrode geometries have been considered, Figure 1.5, in order to analyse the effects of acoustic streaming on electrode processes. In initial investigations, the 'face on' geometry with the working electrode placed 180° with respect to the ultrasonic horn was the most commonly adopted configuration, Figure 1.5 (a) and is still employed in recent investigations [109,117,118] due to its flexibility and adaptability. From this design, the 'side on' geometry was developed, Figure 1.5 (b), which allowed for quantitative analysis of voltam-

metric signals as it causes a flow of solution over the electrode in a manner crudely analogous to a flow channel electrode [119]. In the final geometry, the working electrode is actually embedded into the tip of the ultrasonic horn. This is commonly referred to as a 'sono-trode', Figure 1.5 (c). This geometry produces very high limiting currents even at low ultrasound intensities [120] compared to the other configurations previously described.

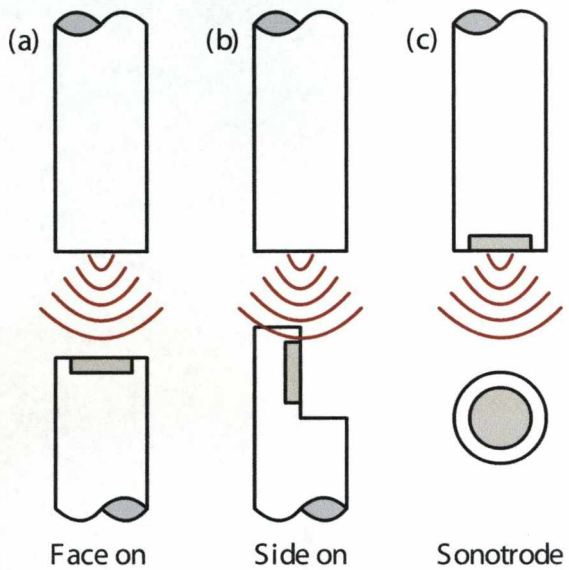


Figure 1.5: Three types of electrode geometries used in sonoelectrochemical measurements

For a reversible reaction, the relationship between the observed limiting current, $I_{lim}$, and the experimental parameters employing during a sonoelectrochemical investigation is given by [121]:

$$I_{lim} = \frac{n\mathrm{F}DAc}{\delta} \tag{1.1}$$

where $n$ is the number of electrons transfered per mole of reactant, F is the Faraday constant, $D$ is the diffusion coefficient, $A$ is the electrode area, $c$ is the concentration and $\delta$ is the diffusion layer thickness. Analysis of sonovoltammetric current data based on Equation 1.1 allows $\delta$ to be determined. For a 'face on' geometry,

the diffusion layer thickness is normally in the range of 6-7 $\mu$m althought, a layer thickness of $\ll$1 $\mu$m has been observed for a Pt sonotrode [120]. Comparing these values to the diffusion layer thickness produced by conventional methods used to enhance mass transport towards the electrode (e.g. for a rotating disc electrode, $\delta$ is typically 10-50 $\mu$m) it is evident that ultrasound induces significantly higher rates of mass transport [122].

An alternative type of sonotrode initially proposed by Reisse et al. [116], uses the titanium horn material itself as an electrode. This overcomes the sometimes complex techniques needed to embed a separate electrode within the ultrasonic horn's tip, as well as the potential problems arising from electrically isolating the working electrode from the conducting titanium body of the equipment. Furthermore, with prolonged high intensity ultrasonication, it is possible for an implanted working electrode to be dislodged even when using a strong cement [120]. Although the diffusion layer thickness achievable using this configuration is similar to that of a separate embedded electrode, the quality of the voltammogram obtained is severely compromised due to the formation of a semiconducting $TiO_2$ layer on the tips surface, which hinders electron transfer [120].

## 1.5 Thesis Outline

The main objective of the present work focused on a novel sonoelectrochemical and chemical synthesis and characterisation of spherical and non-spherical silver and gold nanoparticles along with their immobilisation and application as SERS substrates.

To achieve this, a complex experimental setup has been designed and implemented which allowed full control of the external parameters needed to nucleate and grow small metallic nuclei on a electrode surface and furthermore, to dislodge the grown nuclei into solution using a high intensity burst of ultrasound. Details of the full experimental setup and cell design are given in Chapter 2.

The preparation of silver and gold nanorods was also conducted using a seed mediated, surfactant stabilised method. The preparative technique along with characterisation of the products obtained are described in Chapter 3 and a simple investigation into the mechanism behind the anisotropic growth of silver nanorods in a surfactant medium is presented in Chapter 4. This work was carried out to complement the sonoelectrochemical synthesis of metallic nanoparticles described below.

In order to ascertain the optimum conditions of electrochemical nucleation and growth of metallic nuclei, a series of orientation experiments were conducted using cyclic voltammetry and chronoamperometry. This involved varying the silver metal salt, base electrolyte, concentration of analyte and choice of stabilising agent. Chapter 5 outlines the conditions investigated along with an analysis of the kinetics of nucleation occurring. The synthesis and characteristion of silver nanoparticles prepared with varying concentrations of the stabilising polymer polyvinylpyrrolidone (PVP) with a pulsed sonoelectrochemical method has been achieved and details of these results are given in Chapter 6.

Finally, Chapter 7 describes the immobilisation of gold nanorods onto a gold substrate carried out through electrostatic bonding at different values of pH to

serve as a substrate for Surface Enhanced Raman Spectroscopy. The SERS effect was monitored by the attachment of the Raman active molecule 4-MBA.

# Chapter 2

# Experimental

## 2.1 Introduction

The work carried out in this Thesis followed two distinct routes. Firstly, a novel sonoelectrochemical method for producing monodisperse silver nanostructures was employed and secondly, the chemical synthesis of gold and silver nanorods via a seed mediated, surfactant stabilised route for the use as substrates for Surface Enhanced Raman Spectroscopy measurements was carried out. The first involved extensive design and planning of a new electrochemical cell along with a method for controlling the various physical parameters needed to produce crystalline structures of nanoscale dimensions. The second investigated the chemical factors and kinetics of the reactions involved in the high yield synthesis of silver and gold nanorods. Although both routes were very different the need to fully identify and characterise the products obtained was common to both. This Chapter describes and explains the key techniques used along side a detailed account of the experimental setup used.

## 2.2 Characterisation Techniques

### 2.2.1 Cyclic Voltammetry

Perhaps one of the most highly versatile and commonly cited techniques, cyclic voltammetry is used for both preliminary and more complex studies into the thermodynamics and kinetics of electrodeposition reactions. Typically, a three-electrode cell design is employed. A potential is applied between the working electrode (either macro or micro in size, depending on the type of analyte being investigated) and the counter electrode relative to a high impedance reference electrode. The potential is swept linearly from an initial applied value, $E_1$, to a subsequent potential, $E_2$. Any analyte capable of being reduced within this potential range will produce a current peak. As the scanned potential is reversed back to $E_1$, any analyte capable of being re-oxidised will again produce a current peak. The applied potential waveform diagram is shown in Figure 2.1

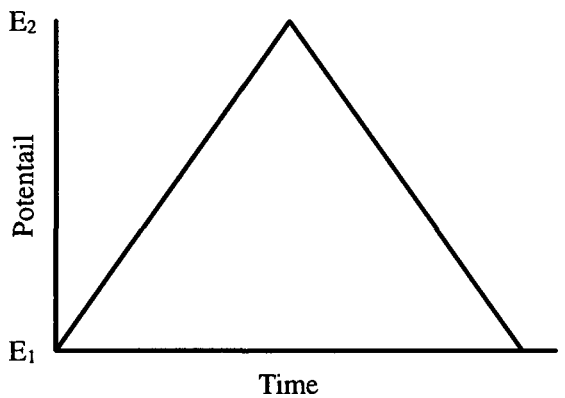


Figure 2.1: Waveform of typical cyclic voltammogram.

For a reversible reaction the voltammetric peak current density, $i_p$, is related to the sweep rate, $\nu$, and the diffusion coefficient, $D$, according to the Randles-Sevcik

equation:

$$i_p = 2.69 \times 10^5 An^{3/2} cD^{1/2} \nu^{1/2} \tag{2.1}$$

where $n$ is the number of electrons transferred per mole of reacting species, $A$ is the area of the working electrode and $c$ is the concentration of the analyte. Regardless of the reversibility of the reaction investigated, the peak currents for both forward and reverse scans depends on both the concentration of electroactive species in the solution and the sweep rate employed. This can range from a few $\mathrm{mVs^{-1}}$ to a few hundred $\mathrm{Vs^{-1}}$ depending upon the experiment. The sweep rate effectively defines the time-scale on which the reaction is examined.

For a fast reversible reaction, in order to maintain the surface concentration of the oxidised and reduced species at the values required by the Nernst Equation (Equation 2.2), electrolysis occurs at the electrode surface in response to the changes in potential.

$$E = E^o - \frac{\mathrm{RT}}{n\mathrm{F}} \ln \frac{\gamma\mathrm{Red}}{\gamma\mathrm{Ox}} \tag{2.2}$$

$E$ is the electrode potential, $\mathrm{E}^o$ is the standard reversible potential of the electrode couple, $\gamma$Red and $\gamma$Ox are the chemical activities for the reduced and oxidized species respectively, F is the Faraday constant, R is the gas constant and T is the absolute temperature.

### 2.2.2 Chronoamperometry

Chronoamperometry is a widely used technique in particular for the study of electrochemical interfacial nucleation [123–128]. In single step chronoamperometric experiments the potential of the working electrode is stepped from a rest potential, usually either the redox potential of the system or a stripping potential where no nucleation can take place, to a potential where nucleation *can* occur. The resulting current response is recorded with respect to time. For reversible reactions the $i-t$ transient produced follows a linear relationship between $i$ and $t^{-1/2}$ expressed

by the Cottrell equation [121]:

$$i(t) = \frac{n\mathrm{F}c\sqrt{D}}{\sqrt{\pi t}} \tag{2.3}$$

From Equation 2.3, at a sufficiently high overpotential, the diffusion coefficient can be calculated from the decaying part of the transient assuming that the entire surface is covered in nuclei and therefore diffusion to the surface is linear. By studying the rising section of the transient at varying overpotentials, the type of nucleation occuring and its kinetics can be investigated along with an estimation of the nuclear number density of the deposited metal. Further details about the theory of nucleation and growth of nuclei are described in Chapter 5, Section 5.2.

Double step chronoamperometry employs a more complex potential-time profile. As before, the potential of the working electrode is stepped from a rest potential, $E_0$, to a potential where nucleation occurs, $E_1$. This pulse is generally in the millisecond range, $t_1$. After the short nucleation pulse the potential is stepped to a potential where no further nucleation can take place but where growth of the nuclei formed is allowed, $E_2$, for a predetermined time, $t_2$. This technique allows the control over the shape and size of the nuclei formed by altering the potential and time of electrolysis.

Figure 2.2 shows a schematic diagram of the double pulse profile employed for this, along with the timing of the ultrasonic pulse, when used.

Due to the fast reaction kinetics of metal deposition, fast data acquisition is required for cyclic voltammetry and chronoamperometry measurements and for this reason, the experiments using these techniques were computer controlled. High speed data acquisition was obtained using an USB interface. Details of this will be given later in this Chapter.

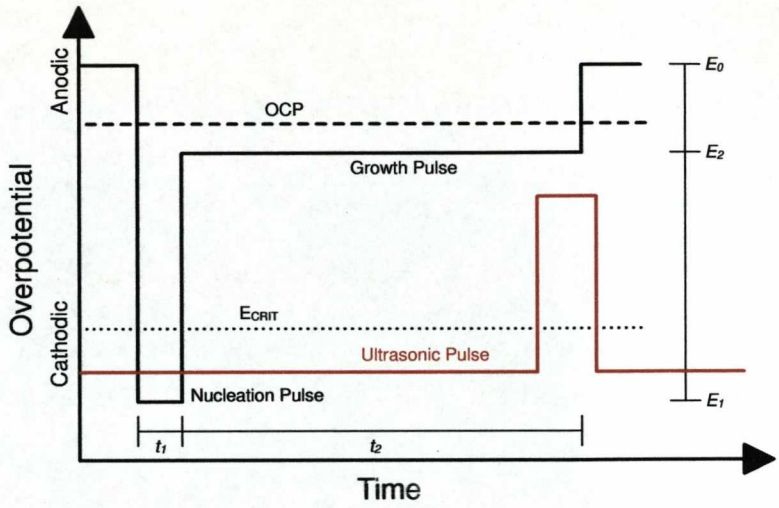


Figure 2.2: Schematic representation of the potentiostatic double-pulse method. The red line represents the ultrasonic pulse employed for dislodging the deposit.

### 2.2.3 UV-Visible Absorption Spectroscopy

Ultraviolet and visible (UV-Vis) absorption spectroscopy has been extensively used for the characterisation of colloidal solutions [27, 129–133] and multilayer formation of metallic nanoparticles through their strong plasmon absorbance [82, 134, 135]. The absorbance of a solution is given by the Beer-Lambert Law:

$$A = -\log \frac{I}{I_0} = \epsilon c l \tag{2.4}$$

where $A$ is the measured absorbance, $I_0$ is the intensity of the incident light at a given wavelength, $I$ is the transmitted intensity, $l$ the path length through the sample, $c$ the concentration of the absorbing species and $\epsilon$ is the extinction coefficient of the species being investigated.

UV-Vis absorption spectroscopy works on the principle that absorption of ultraviolet and visible light causes an electronic transition from a lower to a higher energy level. Since energy-level structures are different for different atoms/molecules then the spectrum produced can be used as an identification tool.

Modern day spectrophotometers use two different light sources, an incandescent light bulb for the visible region and a deuterium arc lamp for the ultraviolet, to produce a scan range of 200 to 1100 nm. Dual-beam spectrophotometers utilise two sample compartments, one for the sample and the other for the reference solution making it possible to collect real-time data.

### 2.2.4 Ellipsometery

The theory of ellipsometry was first developed by Paul Drude in 1887 from the Maxwell Equations of electrodymanics, although the technique only became established in the 1970's with the development of powerful computers capable of handling the complex calculations needed to process the data obtained. Mainly used in the charactisation of the optical properties of thin-film and multi-layered materials [136–138], the technique is both non-destructive and non-invasive.

There are two contributions to polarised light, light polarised parallel (p-polarised) and light polarised perpendicular (s-polarised) to the plane of incidence. Ellipsometry works on the principle that when linearly polarised light is reflected off a surface, the reflected light becomes elliptically polarised. The degree of ellipticity is determined by the complex dielectric function of the sample, Equation 2.5 [139] and its thickness:

$$\epsilon = \epsilon^{'} + i\epsilon^{''} \tag{2.5}$$

$\epsilon^{'}$ is the real part and $\epsilon^{''}$ is the imaginary part of the dielectric function respectively. These quantities are related to the refractive index according to:

$$\epsilon^{'} = n^2 + \kappa^2 \tag{2.6}$$

$$\epsilon^{''} = n\kappa \tag{2.7}$$

$n$ is the refractive index and $\kappa$ is the extinction coefficient. The ratio of the reflected p and s polarised light and also the phase difference is measured and are related by Equation 2.8:

$$\frac{R_p}{R_s} = \tan \Psi e^{i\Delta} \tag{2.8}$$

where $R_p$ and $R_s$ are the reflectance of the p and s polarised light components respectively which are defined by the Fresnel Equations; $\Delta$ and $\Psi$ are the phase shifts and the amplitude ratio, respectively. The Fresnel equations relate the reflected elliptically polarised light to the optical constants of the material.

Maxwell's equations state that when light interacts with a surface it will be both immediately reflected and also refracted. The angle of incidence, $\phi_i$, will be equal to the angle of reflectance, $\phi_r$. The refracted light will be at an angle, $\phi_t$ given by Snells law, Equation 2.9:

$$\bar{n_0} \sin(\phi_i) = \bar{n_1} \sin(\phi_t) \tag{2.9}$$

$\bar{n_0}$ and $\bar{n_1}$ are complex the refractive indices of the two different media, given by equation 2.10, $\phi_i$ is the angle of incidence and $\phi_t$ is the angle of refraction. Figure 2.3 shows a simple representation of light interacting with an air/film/bulk system.

$$\bar{n} = n + i\kappa \tag{2.10}$$

By measuring the difference between the two reflections, the thickness of the device can be determined. The reflected light also undergoes a change in polarization; this change is used to calculate the refractive index and absorption coefficient. Therefore if the angle of incidence is known then the optical constants can be calculated from the measured $\Delta$ and $\Psi$ values.

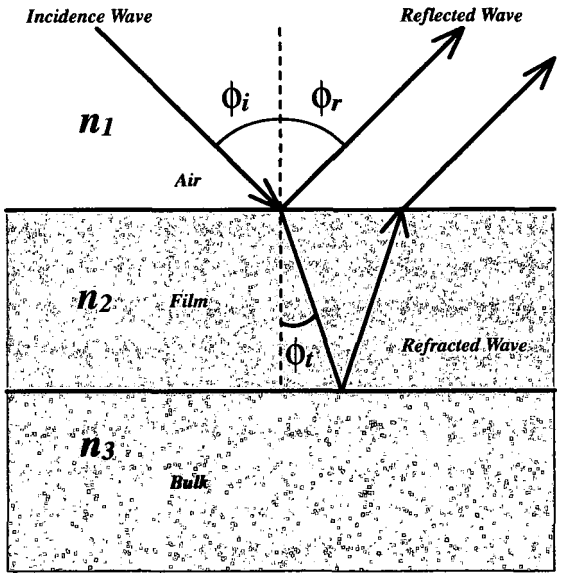


Figure 2.3: Schematic diagram showing the interaction of light with an air/film/bulk system.

### 2.2.5 Raman Spectroscopy

Spectroscopy, in its simplest form, is the study of the interaction of light with matter. It is based on the fundamental principle that when light (be it visible, infra-red or UV) interacts with matter it is either absorbed or transmitted and this causes a change in the electronic, vibrational and rotational state of molecules.

Raman spectroscopy is based upon light scattering theory. When light interacts with a molecule the photons can be elastically scattered, that is to say they have the same frequency and, hence, the same wavelength as the incidence radiation. This is known as Rayleigh scattering. However, a small proportion of the photons, usually around $1 \times 10^{-7}$, scatter inelastically. These photons have a different wavelength to the incident radiation and this is known as Raman scattering. Figure 2.4 shows a simplified view of these three types of scattering.

In classical terms, the phenomenon of Raman scattering occurs when incident photons interact with the electric dipole of a molecular bond. This causes an

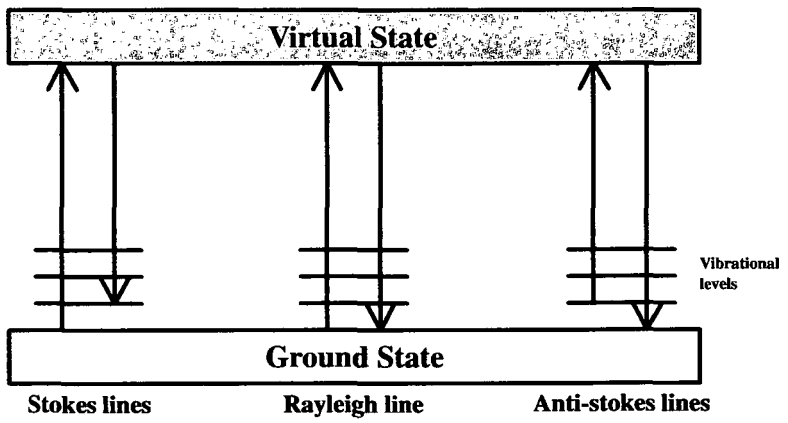


Figure 2.4: A schematic energy level diagram showing the states involved in Raman signal.

electron to be excited to a virtual state. If this excitation occurs from a ground state and relaxes to an excited vibrational state then the energy of the scattered photons produced is less than the energy of the incident photons. This generates what is known as the Stokes lines. There are, however, a small proportion of molecules already in an excited state. These molecules also excite to a virtual state but relax to the lower ground state. This causes the energy of the scattered photons to be higher in energy than that of the incident photons and produces the anti-Stokes lines. Since the number of molecules already in this excited state is far lower than the number in the ground state, the relative intensity of the Stokes and anti-Stokes lines follows a similar trend. Interestingly, the wavelength change for both the Stokes and anti-Stokes lines either side of the Rayleigh line is the same. This is a consequence of the quantisation of energy. The Stokes and anti-Stokes lines equate to the loss and gain, respectively, of the energy corresponding to the change in vibrational state on light absorption.

Similar to infra-red spectroscopy, Raman spectroscopy is governed by selection rules. For a molecule to be IR active there must be a change in its *dipole moment*, however, for a molecule to be Raman active there must be a change in its *anisotropic polarisability*. The polarisability of a molecule is a measure of its

distortion to an applied electric field. For both heteronuclear and homonuclear diatoms, this degree of distortion is relative to the direction of the field. For example, with a molecule of $H_2$, the distortion will be greater if the electric field is parallel to the molecule than if it is perpendicular.

### 2.2.6 Surface Enhanced Raman Spectroscopy

SERS is a branch of Raman Spectroscopy that was discovered, albeit accidentally, by Martin Fleischmann in 1974 [140]. It was observed that pyridine adsorbed onto a chemically roughened silver surface exhibited a Raman signal many times greater than on a smooth surface. The actual process by which this enhancement takes place is still not fully understood but it is thought to be a combination of two mechanisms. The first, electromagnetic enhancement, involves the creation of surface plasmons on the substrate surface by the incident radiation, which transfer energy through an electric field to the target molecules allowing the otherwise inaccessible vibrational structure to be determined. The second, chemical enhancement, is a charge transfer process from the roughened metal surface to a vibrational level of the same energy within the target molecule.

The combination of these two mechanisms gives an enhancement of up to $10^7$ for roughened surfaces and an estimated $10^7 - 10^{15}$ for molecules bound to silver or gold nanoparticles [141]. The exact contribution of each mechanism to the overall enhancement observed is still a matter of debate, although, it is generally accepted that the electromagnetic contribution is far greater than that of the chemical contribution, which is thought to only be 1 to 2 orders of magnitude. The SERS effect has been used in the detection of single molecules of the dye Rhodamine-6G [142–144]. This is an ideal molecule for observing the SERS effect since it has an intense absorption peak at 520 nm, which coincides with the common wavelength of most Raman spectrometers, 532 nm, hence giving excellent surface enhanced resonance. Enhancement relies heavily upon the fact that the molecule

in question is attached to or is in close proximity to a structure that greatly increases the electromagnetic field and hence its sensitivity. For single molecule detection, noble metal nanoparticles are usually the most common choice and it is this choice that can affect the overall increased enhancement of the system.

Different shaped nanostructures exhibit different field enhancement. Spherical nanoparticles have a uniform field enhancement surrounding the sphere whereas nanorods, as well as having a general field enhancement, have a more intensely localized field enhancement at the tips. This type of enhancement is observed to a much greater extent in tetrahedral and bipyrimidal nanostructures.

### 2.2.7 Transmission Electron Microscopy

A fundamental breakthrough in the characterisation of nanoscale structures came with the invention of the Transmission Electron Microscope (TEM). De Broglie observed that matter can behave as waves as well as particles, a phenomenon known as the wave-particle duality. From this he derived that the frequency of a particle is inversely proportional to its momentum, Equation 2.11.

$$\lambda = \frac{\mathrm{h}}{p} = \frac{\mathrm{h}}{m\nu} \tag{2.11}$$

where $\lambda$ is the wavelength, h is Plank constant, $p$ is the momentum of the particle, $m$ is its resting mass and $\nu$ is its velocity. Therefore, as the velocity of an electron increases its wavelength decreases, thus making TEM capable of a far greater resolution than a standard light microscope.

A TEM operates on the same basic principles as the light microscope but uses electrons instead of light. Electrons are produced at the top of the instrument, by a process known as thermionic discharge. This source, usually termed an electron gun, consists of a hairpin shaped filament. The choice of filament material is crucial since its temperature can reach in excess of 2200K. The electrons leav-

ing the filament are then accelerated toward the sample. Since electrons can be manipulated by both an electric and a magnetic field, the TEM uses electromagnetic lenses, in much the same way as a conventional light microscope uses glass lenses, to focus the electron beam. A schematic description of the lenses used is shown in Figure 2.5. The focused beam then hits the sample and depending on the specimen, various processes can occur as shown in Figure 2.6. This allows determination of the samples physical and chemical properties such as size, shape, crystallographic structure and, with the use of an energy dispersive analysis by X-rays (EDAX) detector, its chemical composition. The image is enlarged with the aid of a number of electromagnetic lenses as it passes down the microscope to the imaging screen. The contrast image produced is indicative of where the sample either allowed only a small number electrons to be transmitted (dark areas) or it allowed most electrons to pass through (light areas).

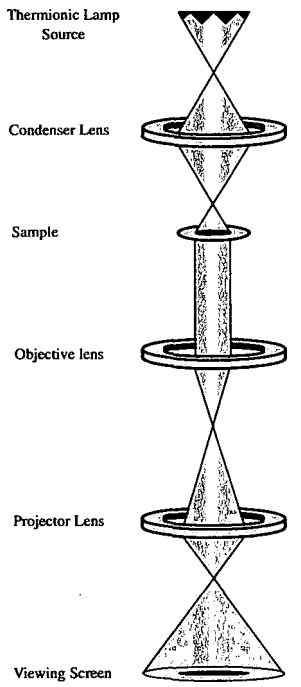


Figure 2.5: Schematic showing the lenses used in a TEM.

Although TEM is a tremendously useful and invaluable technique for imaging not only nanostructures, but also biological samples, it is not without its drawbacks. Due to the nature of the technique, the sample being imaged needs to be extremely thin so as to allow electrons to pass through it. This can lead to long sample preparation times. In addition, due to the high vacuum needed, the sample has to be thoroughly dessicated prior to use, which means living samples cannot be imaged. Furthermore, due to the use of electrons the technique can be invasive to the sample being studied.

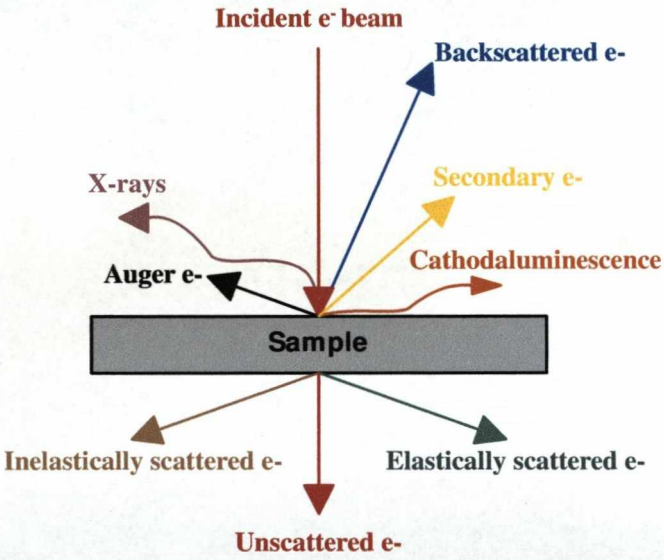


Figure 2.6: The various electron processes which can occur when striking a specimen.

## 2.3 Instrumentation

This section gives details of all the instrumentation used throughout this Thesis. This avoids repetition and also gives a solid scientific background to the work undertaken.

### 2.3.1 Autolab System

An Autolab III system (Eco-Chemie, Netherlands) was used to control all the electrochemical techniques and experiments. This system allows the attachment of specialised modules for customising the equipment to the needs of the experiment. The Autolab used was equipped with a PGSTAT20 potentiostat module and a DIO48 card. High speed data transfer to a computer was achieved via an USB adapter (Autolab USB interface, Eco-Chemie) and the General Purpose Electrochemical System (GPES) software controlled the system.

### 2.3.2 Waveform Generator

Two waveform generators were employed in the control of the sonoelectrochemical experiments. Both waveform generators were the PPR1 type(Hi-Tek Instruments, UK) capable of both internal repetition of pulse sequences and external triggering.

### 2.3.3 Oscilloscopes

In conjunction with the two waveform generators, two digital oscilloscopes were also used. To map the pulse profiles a Gould 4071 100 MHz Digital Oscilloscope, capable of sampling at 400 Ms/sec was used. For the current response, a Gould 1602 DSO, capable of sampling at 20 Ms/sec was employed.

### 2.3.4 High Frequency Ultrasonic Horn

For all the ultrasonic experiments an ultrasonic processor (VC-505, Sonics & Materials), fitted with a 13mm titanium horn was employed. The horn allowed the tips to be removed and replaced if degradation occurred during prolonged ultrasonication. This operated at a constant frequency of 20 kHz and had a maximum power output of 500W. This model of ultrasonic horn was chosen due to its specific operation frequency of 20 kHz, which is the optimum frequency for cavitation to occur. It also has the option to be externally controlled.

### 2.3.5 Centrifuge

Nanoparticle size separations were performed using a Universal 32 tabletop centrifuge (Hettich, Germany). This was equipped with a standard $35^o$ fixed angle rotor. The rotor was capable of holding six sample tubes of varying volumes (15 - 50 mL) and had a maximum spin velocity of 9000 rpm.

### 2.3.6 Transmission Electron Microscopes

Two different TEM instruments were used for the imaging of nanoparticles. The first was a FEI 120kV Tecnai G 2 Spirit BioTWIN from the School of Biological Sciences, University of Liverpool. This machine operated at 120 keV and was capable of a 0.36 nm point resolution. Digital images were captured using a SIS Megaview III camera and data analysis was performed using the AnalySIS Pro software. The second was a JEOL 2000 FX II Electron Microscope from the Materials Science Department, University of Liverpool. This machine operated at 200 keV with a standard tungsten filament. Images were captured via exposure onto a standard size film, 65 x 90 mm.

### 2.3.7 Ellipsometer

Ellipsometry measurements were conducted on a L126 Rotating Analyzer Ellipsometer (Gaertner Scientific Corporation, USA) at a fixed angle of incidence of 70° equipped with a 1mW He-Ne 632.8nm laser. Data analysis was performed with Ellgraph and Filmfit software supplied by Dr R.Greef, Southampton.

### 2.3.8 UV-Vis Spectrometer

All UV/Vis experiments were performed with a Perkin Elmer Lambda 25 spectrometer using a 10 mm x 10 mm quartz cuvette. The spectrometer has a maximum scanning range between 190 and 1100 $cm^{-1}$.

### 2.3.9 Raman Spectrometer

For all Raman and SERS experiments a R-2001 Raman Spectrometer (Ocean Optics, USA) was employed. This was fitted with a 532 nm wavelength type IIIb diode laser with a maximum output of 25 mW. It was capable of measuring over a range of 200 - 4300 $cm^{-1}$ with a resolution of 15 $cm^{-1}$. The parameters for each experiment were controlled using the software supplied by the manufacturer.

## 2.4 Spectral Deconvolution

Deconvolution of the UV/Vis data obtained was performed using Origin Software (Version 7, Microcal). A Gaussian peak fitting profile was chosen to fit the peaks:

$$y = y_o + \frac{A}{\omega\sqrt{\pi/2}} \exp \frac{-2(x - x_c)^2}{\omega^2} \tag{2.12}$$

$y_o$ is the baseline correction, $x_c$ is the deconvoluted peak position, $A$ is the area of the peak and $\omega$ is the FWHM value. All spectra were baseline corrected prior to deconvolution.

## 2.5 Sonoelectrochemical Technique

This section describes the experimental setup and procedures used for the production of silver nanoparticles using ultrasound to dislodge metallic clusters formed by electrodeposition. Two separate experimental configurations were employed. In the first, the potentials and times of the pulse profile were controlled externally using a computer. In the second the potentials and times were controlled using two waveform generators. The reason for using two different approaches is explained below.

All glassware used for the electrochemical measurements was cleaned by immersion for at least 24 hrs in a bath of concentrated acid (50:50 HNO3: H2SO4, BDH, AnalaR), followed by multiple rinsing with pure water. For the preparation of all solutions and samples, water purified using the Millipore (Milli-Q) system to a resistivity of 18MΩ cm was used.

### 2.5.1 Experimental Setup - Part I

To create the pulse profile needed for the sonoelectrochemical experiments, two separate waveform generators were required. One generator controlled the pulse sent to the potentiostat and for starting a predefined macro. The other controlled the initiation of the ultrasonic processor delivering an ultrasonic pulse to the electrode.

In conjunction with the two waveform generators, a digital oscilloscope was used with one channel connected to the reference electrode in the electrochemical cell and another channel connected to the waveform generator responsible for initialising the ultrasonic pulse. In this way a visual representation of the potentials used in the nucleation and growth pulse profile and the timing of the ultrasonic pulse employed within the deposition cycle was obtained. This was useful since it allowed the fine tuning of the timing, length and intensity of the ultrasonic pulse

with respect to the nucleation and growth potentials in the profile. All cables used in the setup were fitted with BNC connectors. Figure 2.7 shows a schematic diagram of the equipment used.

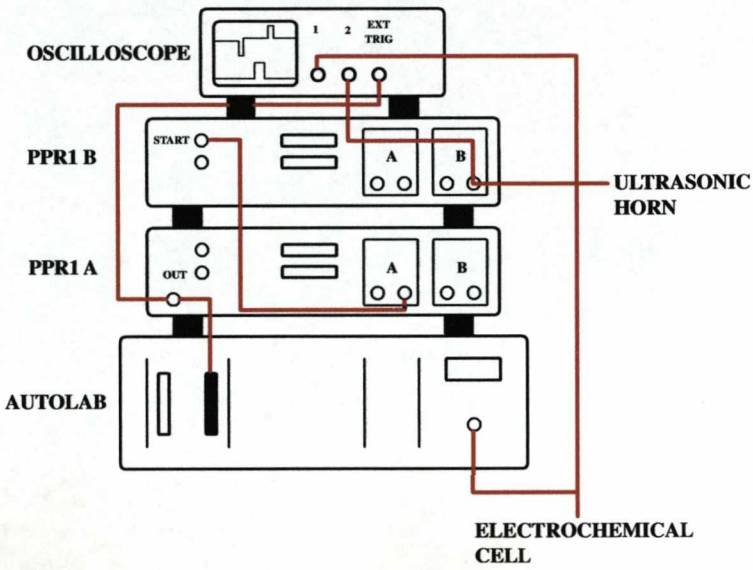


Figure 2.7: The ultrasonic experiment hardware setup used in Part I.

#### 2.5.1.1 Macro

A macro was written to control the numerous processes involved in adapting the requirements of the sonoelectrochemical technique to be computer controlled. This allowed external control and resetting of the Autolab system and for a single nucleation and growth experiment to be repeated for a specified number of cycles. Figure 2.8 shows the macro used. The macro was written within the Autolab software using the macro program provided.

The "OPEN=("C:\...filename") term refers to a pre-saved procedure within Autolab where the parameters for the electrochemical measurements were defined. "P2" refers to the 25-pin plug mounted on the DIO48 module of the Autolab system. The connectors to this plug were attached to pin 1 and 25, as stated in

```
PROCEDURE! METHOD=CM
PROCEDURE! OPEN=("C:\...filename")
DATASET! AUTONUM=1
DATASET! AUTOREPLACE("001")
REPEAT(n)
DIO! WAITBIT("P2","A","0","ON")
PROCEDURE! START
DATASET! SAVEAS("C:\...filename1")
ENDREPEAT
```

Figure 2.8: The macro used to control the sonoelectrochemical experiments.

the manufacturers user manual, in order for the Autolab system to be externally controlled.

The type of experiment required was selected from within the Autolab software and the potentials, times and number of data points for each pulse entered. The selection of the number of data points recorded proved critical since the transient produced during the nucleation phase of the experiment is quite complex and requires a large number of data points in order to collect all the necessary information.

#### 2.5.1.2 Experimental Procedure

The equipment was setup as described in Section 2.5.1. All electrodes were attached to the Autolab system via the supplied cable. The cable connected to channel 1 of oscilloscope A was split with one wire connected to ground and the other connected to the reference electrode. This allowed the nucleation and growth potentials to be viewed on the oscilloscope. Once the experimental parameters had been entered into the procedure file in the Autolab software, the macro was started. Before the Autolab recorded any measurements it waited for an external trigger from PPR1 A. The experiment was started manually from the PPR1 A trigger. This did three things. Firstly, it sent a signal to the Autolab triggering it to start the measurement. Secondly, it sent a signal to the PPR1 B triggering

it to send a pulse to the ultrasonic processor, this then sent a pulse of a specified length to the ultrasonic horn in the cell, with a controllable time delay, and thirdly, it triggered the oscilloscope to start recording the pulse profiles of both the nucleation and growth potentials and the ultrasonic burst.

Due to the repeat command in the macro, the software waits for another trigger from the PPR1 A once this cycle was finished. This was achieved by setting the re-trigger delay on the PPR1 A to a value greater than the time taken to complete one measurement cycle. This allowed the experiment to be left running without the need for continual manual triggering once it had been started. Once the macro had reached the end of a predefined number of cycles the PPR1 A was reset. For each cycle of the macro, a transient was recorded and saved.

### 2.5.2 Experimental Setup - Part II

In this experimental setup, a PPR1 waveform generator was used to control the potentials and times of the pulse profile. This allowed a more rapid repetition cycle for each electrochemical and ultrasonic pulse. This setup utilised the same equipment as described in Section 2.5.1 but a second digital oscilloscope was connected directly to the Autolab System. This allowed the current response of the electrode, which had previously been measured by the GPES software, to be observed. Figure 2.9 shows a schematic description of this setup.

#### 2.5.2.1 Experimental Procedure

The main difference in this setup as compared with that in Section 2.5.1, was that the procedure was started and retriggered from the PPR1's and not by the computer software. This was achieved by using the PPR1's internal retrigger function. This has a range from 1ms to 10s or the option to be externally triggered. In this case a constant retrigger time of 1s was chosen. This was longer than the total nucleation and growth potential pulse which allowed each pulse to go to completion

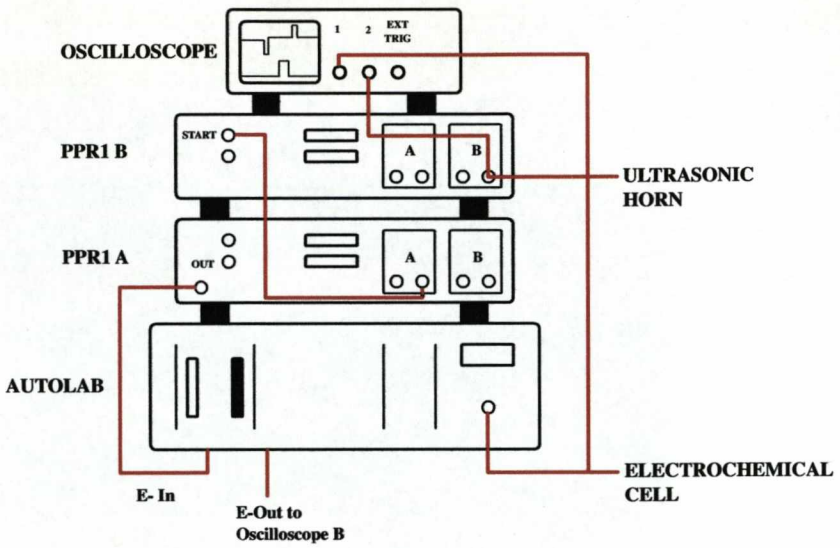


Figure 2.9: The ultrasonic experiment hardware setup used in Part II.

before the system was retriggered. The potentials chosen in the PPR1 were relayed to the Autolab system by connecting the output signal (OUT) of the PPR1 to the E-In input of the Autolab equipment. The electrochemical cell was then connected to the Autolab as normal. Therefore, in this configuration, the Autolab was only used as a potentiostat and the potential sequence was established by the external waveform generators. The whole experiment was started by initialising the PPR1 A and could be left running until completion. The PPR1 B was again used to control the ultrasonic pulse timing.

### 2.5.3 Electrochemical Cell

For all electrochemical experiments a standard three electrode cell was employed similar to that originally designed by Compton et al. [104, 117, 119]. This cell design was modified, however, to an hourglass shape. This maximised the space within the cell to allow the three electrodes and the ultrasonic horn to be placed inside it but also allowed easy positioning of the working electrode. The horn was held in place by a retort stand and boss clamp attached to the transducer section

of the horn.

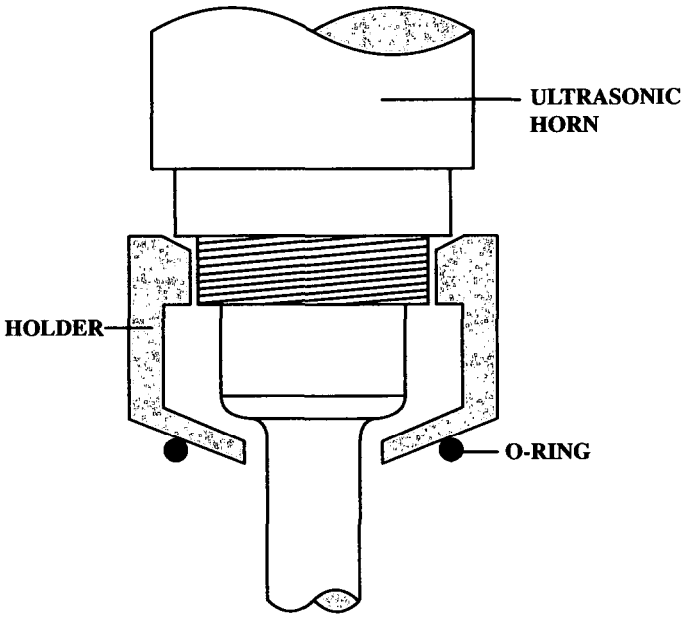


Figure 2.10: Schematic diagram showing the stainless steel holder used to isolate the electrochemical cell from the ultrasonic horn.

Due to the oscillation of the titanium horn it was necessary to isolate it from the glass cell to prevent damage. This was achieved by a stainless steel holder milled to the exact specifications of the horn. The ultrasonic horn was positioned at the top of the cell and an airtight seal was achieved by resting the holder on a rubber "O"-ring. Figure 2.10 shows a schematic drawing of the holder used.

The working electrode was housed in a PTFE holder. This was held in place by a screw cap and a PTFE "O"-ring and was milled to a diameter slightly smaller than that of the PTFE "O"-ring used to fix the holder in place. This PTFE-PTFE joint was both air and water tight. The electrode was positioned at an angle of $180^{o}$ with respect to the horn so that both surfaces were facing each other. The distance between each face was kept constant at 2mm, Figure 2.11.

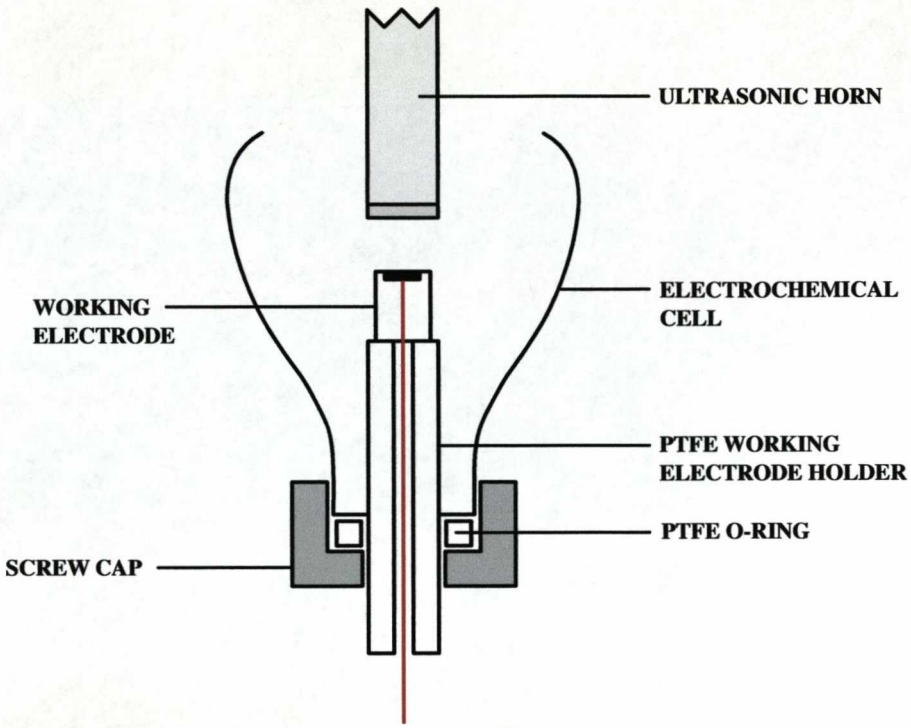


Figure 2.11: Schematic diagram showing the working electrode holder.

### 2.5.4 Electrodes

Two working electrodes were used for this investigation, platinum and glassy carbon. Both were sealed in PTFE and had a surface area of 0.188 $cm^2$. Prior to each experiment the working electrodes were polished using successively finer grades of alumina slurries (Buehler Micropolish, USA) until a mirror finish was produced. A saturated mercury sulphate ($Hg/Hg_2SO_4$, $Na_2SO_4$ (sat)) reference electrode was employed. This was set adjacent to the working electrode via a Luggin capillary to decrease ohmic drop. A platinum gauze acted as the counter electrode. All potentials stated are with respect to the Saturated Mercury Sulphate Electrode (MSE). Prior to all experiments the solution was deoxygenated for 30 minutes with purified argon . Figure 2.12 shows a picture of the electrochemical cell prior to a measurement being carried out.

Figure 2.12: Photograph of the electrochemical cell used in the sonoelectrochemical experiments.

# Chapter 3

# Preparation and Characterisation of Silver and Gold Nanorods

## 3.1 Introduction

The electrochemical synthesis of metal nanostructures is only relatively new. The first, and indeed the majority of nanoparticle syntheses, are chemically based. Well-defined nanostructures are very desirable due to their unique optical and electronic properties. These are strongly dependent on the size and shape of the particles employed in their construction and therefore, there is an increasing need to control these parameters for fine tuning their properties. This Chapter describes the application of a seed mediated method used in the preparation of gold and silver nanorods for use as substrates for Surface Enhanced Raman Spectroscopy measurements due to the large electromagnetic field enhancement these can induce [145].

The synthesis of metallic nanorods by the seed mediated route essentially involves two steps. Firstly, the preparation of small size spherical nanoparticles and secondly, the growth of these seeds in a rod-like micellar environment. The addition of preformed seeds has two advantages: (1) It increases the overall reaction

rate and hence the nanorods growth rate and (2) Nanorod aspect ratio can be controlled by varying the ratio of metal salt to seed. Ascorbic acid was employed as the reducing agent for gold and silver salts in the growth stage. Ascorbic acid is a mild reducing agent that cannot reduce silver or gold salts in micellar solutions without the presence of a seed. This approach separates the nucleation from the growth steps, greatly reducing any additional nucleation occurring during the growth phase with the corresponding improvement in monodispersity. As described later on, the same strategy was used for the electrochemical growth of nanoparticles.

## 3.2 CTAB Stabilised Gold Nanorods

### 3.2.1 Chemicals and Materials

Cetyltrimethylammonium bromide (CTAB, 99%), L-ascorbic Acid (99%), Hydrogen tetrachloroaurate ($HAuCl_4.3H_2O$, 99.99%), silver nitrate ($AgNO_3$, 99.999%), sodium borohydride ($NaBH_4$, 99.9%) were purchased from Aldrich. All glassware was cleaned prior to use using freshly prepared aqua regia (1:3 $HNO_3$:HCl) followed by repeated rinsing with ultra pure Milli-Q water.

### 3.2.2 CTAB Stabilised Gold Nanoparticles Seed Synthesis

The synthesis used follows the method described by Murphy et al. [27] with slight modifications. Gold seeds were synthesised using CTAB as a stabilising agent. El-Sayed et al. [146] observed that the use of CTAB as opposed to tri-sodium citrate as the capping agent, for the seed produced a far higher yield of nanorods. When citrate was used, distorted nanorods and star shaped fractals were produced [146].

Briefly, 0.25 mL of 0.01 M $HAuCl_4$ was added to 7.5 mL of 0.1 M CTAB and mixed by inversion. To this, 0.6 mL of freshly prepared ice-cold 0.01 M $NaBH_4$

was injected, followed by rapid inversion for two minutes. The solution produced was pale brown/yellow. The gold seeds were used after one hour to allow the $NaBH_4$ to react completely.

Figure 3.1 shows the UV-Vis adsorption spectrum of the as-prepared CTAB stabilised gold seed nanoparticles 1 hour after preparation. Murphy et al. [27] states that the gold nanoparticles produced should be ~4 nm in diameter. The absence of a surface plasmon band , however, indicates the presence of smaller gold particles than expected. A similar UV-Vis absorption spectra to the one presented here was obtained by Nikoobakht using a similar method [146]. TEM

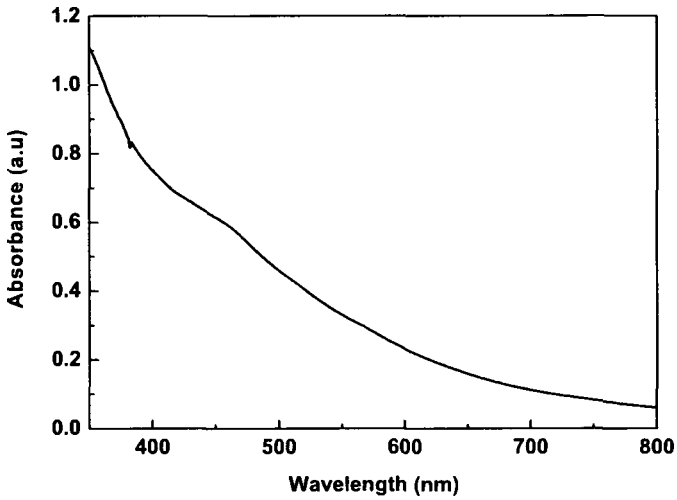


Figure 3.1: UV-Visible absorption spectrum of CTAB stabilised gold seed nanoparticles

images of the particles, Figure 3.2, show they their mean diameter was (4.6±0.9) nm which is in good agreement with the results reported by Murphy et al. [27], indicating that slight aggregation must occur between preparation and imaging.

The gold seed nanoparticles could only be used up to one day after preparation. After this time aggregation occurred. This was visible by a change in the colour

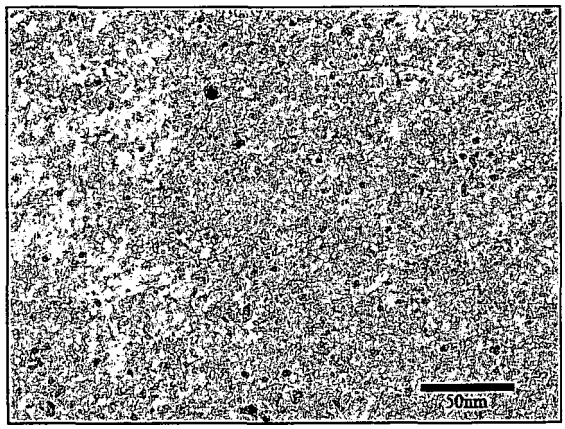


Figure 3.2: TEM image of the as-prepared CTAB stabilised gold seed

of the solution from a pale brown to a pinkish red. This was confirmed by the UV-Vis spectrum, Figure 3.3, of 18 day old seed nanoparticles. A surface plasmon band at 502nm is clearly visible. This is lower than that expected for the plasmon band for Au, probably due to the presence of a CTAB environment.

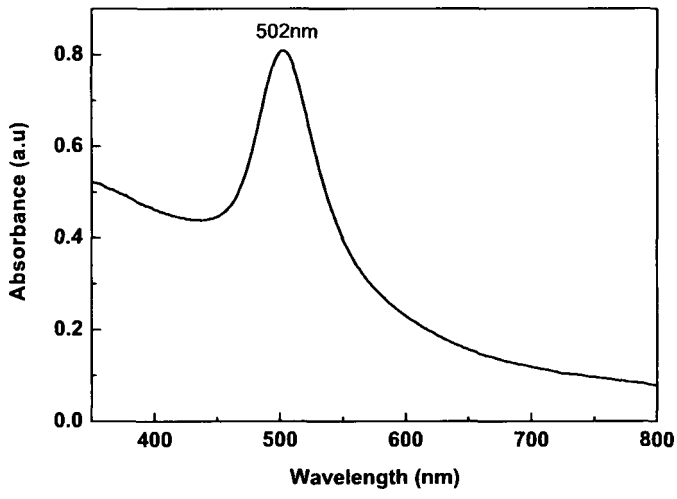


Figure 3.3: UV-Visible absorption spectrum of CTAB stabilised gold seed nanoparticles after 18 days

Pileni et al. [147] investigated the effects of these larger aged seeds when used in the formation of gold nanorods. It was found that an increase in size from 3nm (2 hours old) to an average of 7nm (30 days old) drastically affected both the yield and morphology of the nanorods produced. This increase in seed size virtually eliminated the longitudinal plasmon band and only produced large agglomerates.

### 3.2.3 Gold Nanorod Synthesis

Gold nanorods were prepared as follows. 9.5 mL of 0.1 M aqueous CTAB was added to varying amounts (80, 160 and 300 $\mu$L) of 0.01 M silver nitrate aqueous solution and 0.5 mL of 0.01 M $HAuCl_4$. The solution turned dark orange/brown upon the addition of the $HAuCl_4$. 80 $\mu$L of 0.1 M aqueous ascorbic acid was then added with stirring. After ~30 seconds the solution became clear indicating a change in the gold oxidation state from $Au^{3+}$ to $Au^{+}$. Varying amounts (12, 24 and 36 $\mu$L) of the as-prepared CTAB stabilised gold seeds were rapidly injected into this growth solution to initiate the growth of the gold nanorods. After vigorous shaking for one minute the solution was left to age for two hours. During this period the solution changed colour from clear to deep purple within thirty minutes, indicating the formation of gold nanorods.

The gold nanorods thus prepated were contained in a highly concentrated CTAB solution, which at room temperature is poorly soluble in water. Therefore, for their characterisation and subsequent used, the gold nanorods had to be isolated and re-dispersed in ultra pure water. This was achieved by centrifugation. The solutions were placed into plastic centrifuge tubes (Falcon, Sigma) and centrifuged at 6000 rpm for twenty minutes. The supernatant was carefully extracted leaving a pellet of nanorods at the bottom of the centrifuge tube. This was re-dispersed in 4 mL of ultra pure Milli-Q water and the centrifugation repeated. After a final re-dispersion in 1.5 mL of water the samples were considered ready for analysis. Any further attempt to centrifuge the sample led to aggregation due

to the lack of a sufficiently high concentration of stabilising CTAB in the solution.

#### 3.2.3.1 Results with Varying Silver Nitrate Concentration

The silver nitrate concentration in the growth solution was varied by adding different amounts of silver nitrate solution. Although it is not directly involved in the control of aspect ratio, silver nitrate is needed to produce gold nanorods in a high yield [19,41]. The direct mechanism for this is still unknown but it is thought that silver forms an AgBr complex which inhibits its reduction by ascorbic acid. It has been proposed that this AgBr complex adsorbs onto the surface of the Au particle and restricts its growth in a linear fashion [19, 43, 148]. This is discussed in more detail in Chapter 4. The production of the gold nanorods was followed by UV-Vis spectroscopy at various intervals in their formation and their size and morphology was established by TEM. Figures 3.4 and 3.5 show the UV-Vis spectra and the corresponding TEM images of the gold nanorods produced with the addition of varying amounts of the silver nitrate solution and gold seed amounts, respectively. Samples for TEM characterisation were prepared by placing 3 $\mu$L of the centrifuged suspension onto a copper grid (400 mesh, Agar Scientific, UK) and allowing the solvent to dry overnight in air.

The UV-Vis spectra of all solutions show the presence of two clear plasmon bands, with the addition of a smaller third band in some cases. The first, at $\sim$520 nm, is the conventional transversal plasmon band for spherical or nearly spherical shaped particles. The second is due to the longitudinal plasmon band of the nanorods. The position and intensity of this band is highly sensitive to the aspect ratio and concentration of the gold nanorods produced, with higher aspect ratio nanorods causing a shift to higher wavelength in the absorption spectrum and vice-versa. From Figures 3.4 and 3.5 it can be seen that changing both the silver nitrate concentration and the seed concentration has large effects upon the position of the longitudinal plasmon band and the effects of this are clearly seen

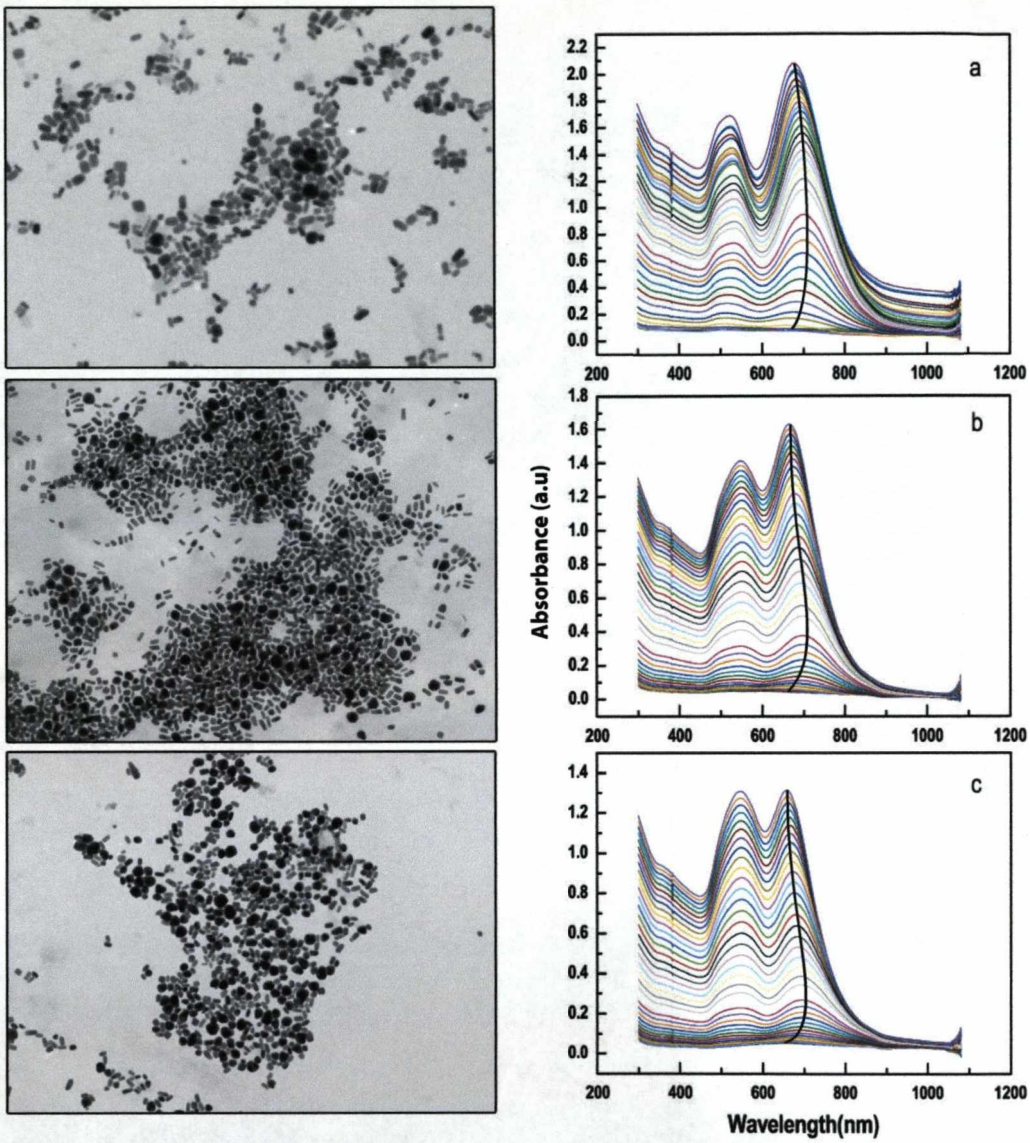


Figure 3.4: UV-Visible absorption spectrum and corresponding TEM images of the prepared gold nanorods with the addition of a) 80 $\mu$L, b) 160 $\mu$L and c) 300 $\mu$L silver nitrate. Seed conc: $1.25\times10^{-6}$ M (12 $\mu$L of gold seed). The spectra were taken at two minute time intervals.

in the corresponding TEM images, with the latter seeming to cause the greatest change.

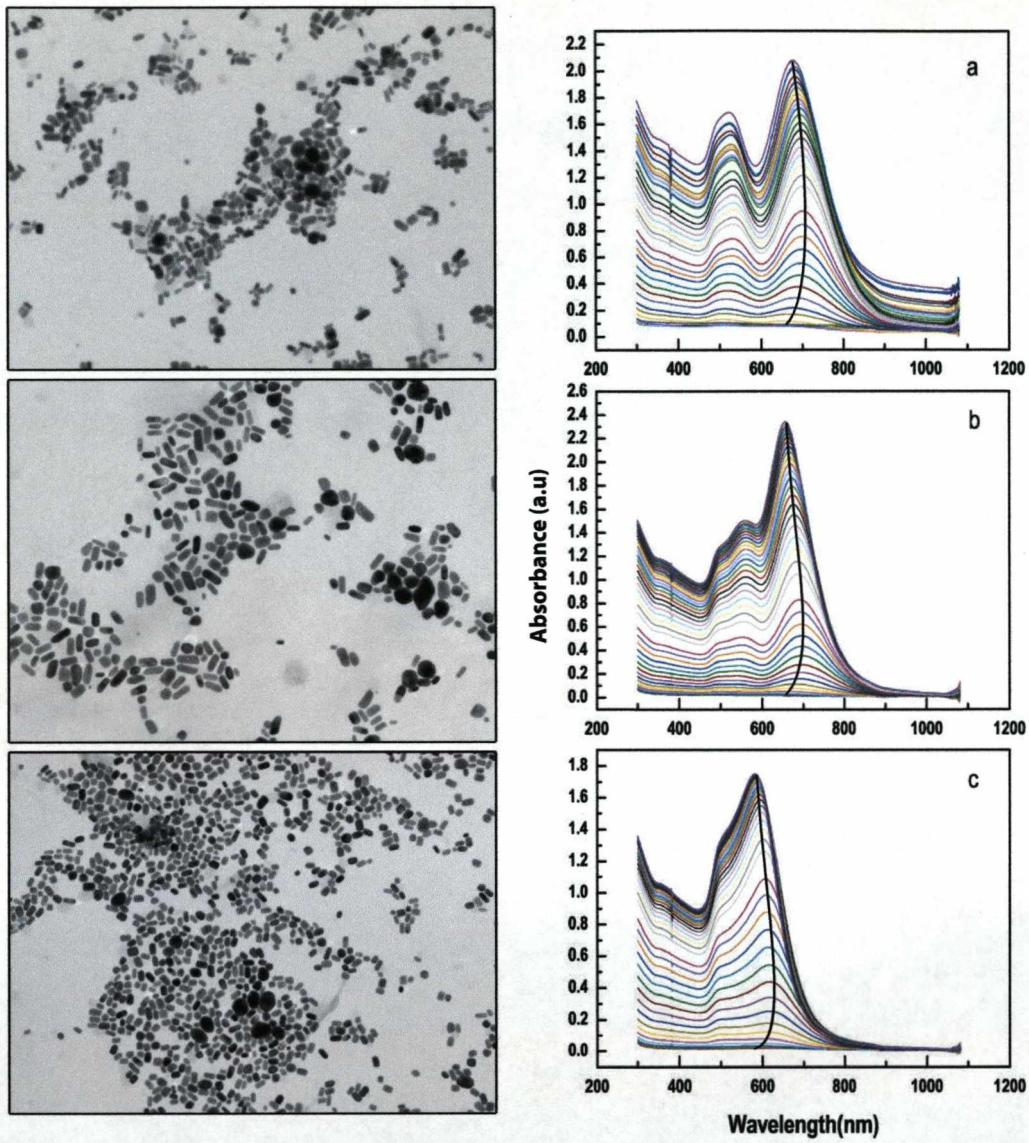


Figure 3.5: UV-Visible absorption spectrum and corresponding TEM images of the prepared gold nanorods with the addition of a) 12 $\mu$L, b) 24 $\mu$L and c) 36 $\mu$L of CTAB stabilised gold seeds. Silver conc: $6\times10^{-5}$ M (80 $\mu$L of silver nitrate). The spectra were taken at two minute time intervals.

Increasing the amount of gold seed present in the growth solution by adding from 12 $\mu$L to 36 $\mu$L of seed solution caused a shift in the longitudinal plasmon

band from 676 to 580 nm with the shape of the nanorods formed being close to spherical, Figure 3.5 (c). Murphy et al. reported that increasing the amount of silver nitrate added to the growth solution increases the aspect ratio of the nanorods produced [27]. This was not observed in the present work, with only a slight decrease in the longitudinal band from 676 to 656 nm. The third, smaller band is assigned to the di-polar resonance of well faceted gold nanocubes which are sometimes present in the solution [39]. However, a noticeable change in the ratio of the two plasmon bands to a vlaue of almost 1:1, was observed indicating an increased presence of spherical nanoparticles. This was confirmed by TEM, Figure 3.4 (c).

From the UV-Vis spectra taken at different stages of nanorod growth it is clear that in all cases nanorod formation started almost immediately upon the addition of the gold seed to the growth solution. One feature to note is the wavelength of the absorbance of the longitudinal plasmon band as the growth of the nanorods progresses. When the seed concentration is varied, Figures 3.4 and 3.5, the initial position of the band increases within the first 10 minutes of growth. This decreases at longer times and the final position is usually at lower wavelengths than the initial value, indicated by the black line. A similar result was observed by Murphy et al. [149]. Since the wavelength maximum of this longitudinal plasmon band is a direct indication of the aspect ratio of the nanorods being produced [150], this indicates that during growth, the nanorods elongate longitudinally first, increasing the aspect ratio and then a widening occurs, reducing the overall aspect ratio and thus shifting the band to lower wavelengths. This effect is also observed when varying the silver nitrate concentration, Figure 3.5, although to a lesser extent.

It is worth to note that although all conditions investigated did produce gold nanorods, the morphology and size deviation was far from constant. This could be attributed to the ambient conditions under which the nanorods were allowed to grow. The solubility of CTAB in water is low at room temperature and for

this reason the CTAB solution used in the growth solution was heated to 40°C to allow the CTAB to fully dissolve. However, CTAB crystalises out of the solution very quickly once room temperature is reached and it is possible that this hinders the growth of the nanorods. It has been reported by Lee et al. [42] for the synthesis of silver nanorods that a constant reaction temperature above that of the point where CTAB dissolves produces nanorods which are more uniform in size and shape although the aspect ratio is reduced. Park et al. [151] observed that a lower temperature is critical for the formation of nanorods with an increase in the aspect ratio of CTAB stabilised gold nanorods from 1 to 40 e.g., when the reaction temperature was decreased from 315 to 376 K. Therefore, a compromise has to be made. From the results obtained in the previous experiments, optimal reaction conditions were chosen, as indicated in Figure 3.6, and the growth solution was transferred to a water bath kept at a constant temperature of 40°C for the entire growth period. The results of this preparation are shown in Figure 3.6. The nanorods formed are dog bone shaped and are in accordance with

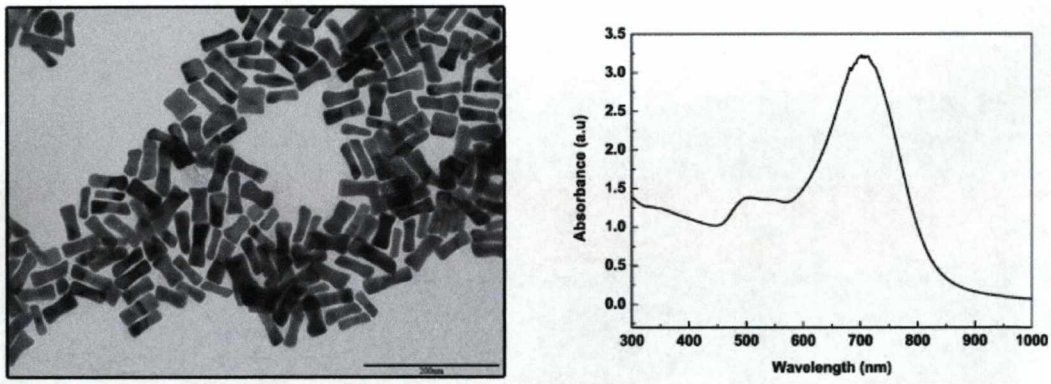


Figure 3.6: UV-Visible absorption spectrum and corresponding TEM images of the prepared gold nanorods with the addition of 100 $\mu$L silver nitrate and 12 $\mu$L of CTAB stabilised gold seeds.

the results from Guo et al [27]. The average length and width of these particles were (54±11) nm and (21±11) nm, respectively, giving an average aspect ratio of

2.8±0.8. The nanorods were stable at room temperature for periods in excess of a month with slight precipitation although a slight red shift in the position of $\lambda_{max}$ of the longitudinal plasmon band was observed [39].

## 3.3 CTAB Stabilised Silver Nanorods

### 3.3.1 Chemicals and Materials

Silver nitrate ($AgNO_3$, 99.999%), tri sodium citrate dehydrate (99+% A.C.S), sodium borohydride ($NaBH_4$, 99.9%), cetyltrimethylammonium bromide (CTAB, 99%), L-ascorbic acid (99%) and sodium hydroxide (NaOH, 96%) were purchased from Sigma.

All glassware was cleaned prior to use using freshly prepared aqua regia (1:3 $HNO_3$:HCl) followed by repeated rinsing with ultra pure Milli-Q water.

### 3.3.2 Citrate Stabilised Silver Nanoparticles Seed Synthesis

This was based on a method described by Jana et al. [21]. A 20 mL solution with a final concentration of 0.25 mM $AgNO_3$ and 0.25 mM trisodium citrate in water was prepared. While stirring vigorously, 0.6 mL of 10 mM $NaBH_4$ was added all at once. Stirring was stopped after 30 s. This seed solution was used two hours after preparation but could not be used after five hours. This method produced uniform seeds with an average size of (5±1) nm. This is in good agreement with Lee et al [42] who, using very similar conditions, produced silver seeds with an average size of (6±2) nm. Figure 3.7 shows the corresponding UV-Visible absorption spectra of the citrate stabilised silver seeds along with their TEM image and size distribution histogram.

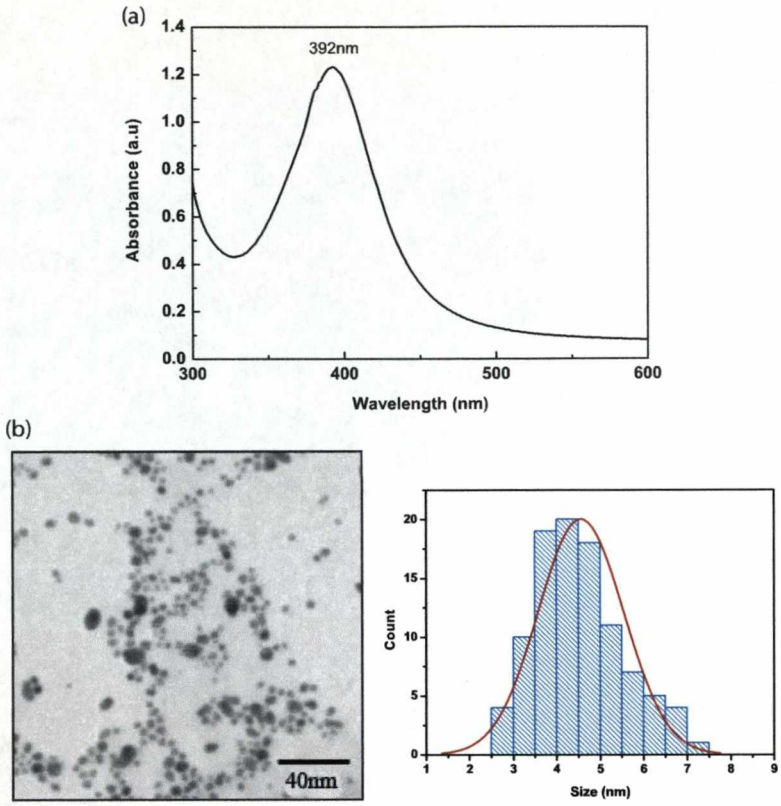


Figure 3.7: (a) UV-Visible absorption spectrum and (b) TEM image and corresponding size distribution of the 5nm citrate stabilised silver seed

### 3.3.3 Silver Nanorod Synthesis

Six solutions sets were prepared containing 0.25 mL of 10 mM $AgNO_3$, 0.50 mL of 100 mM ascorbic acid, and 10 mL of 80 mM CTAB. Next, different volumes of the seed solution (2, 1, 0.5, 0.25, 0.125 or 0.06 mL) were added. Finally, 0.10 mL of 1 M NaOH was added to each set. NaOH must be added last to obtain the desired nanorods in a decent yield. After adding the NaOH, the solution was gently shaken. Within 1-10 min a colour change occurred varying from red, to brown, to green depending on seed concentration as shown in Figure 3.8. Each solution contained a mixture of rods and spheres.

Rods were separated from the spheres and surfactant by centrifugation. For solutions prepared with the addition of 250 $\mu$L or more of seed solution, the

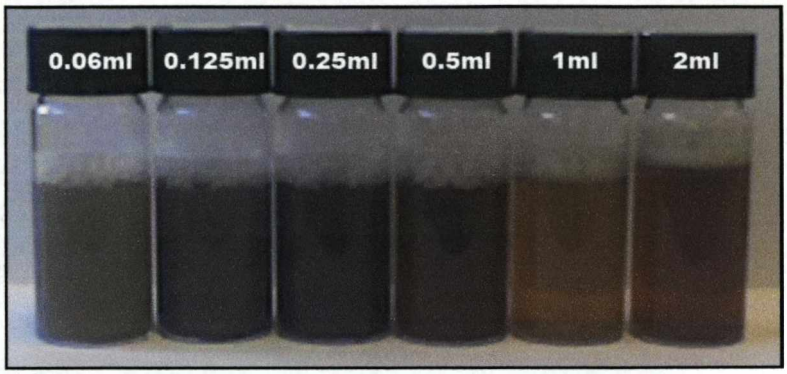


Figure 3.8: A photograph of the as-prepared silver nanorods with varying concentrations of silver seeds.

solution was centrifuged at 6000 rpm for 30 minutes; for solutions containing 125 $\mu$L and 60 $\mu$L of seed, the solution was centrifuged at 2000 rpm for 10 minutes. For each solution the supernatant was carefully removed and the solid was re-dispersed into 4mL of ultra pure water. Centrifugation was then repeated and finally the solid was re-dispersed in 1mL of ultra pure water. Any further attempt at purification by centrifugation caused the particles to precipitate.

Figure 3.9 shows the UV-Vis absorption spectra for each seed concentration. The conventional plasmon band at ~420 nm is observed for spherical silver nanoparticles. At longer wavelengths a secondary plasmon band is also observed assigned to the longitudinal plasmon resonance of rod shaped particles. Decreasing the concentration of the citrate stabilised seed caused a red shift in the position of the plasmon band to higher wavelengths, indicating an increase in the aspect ratio of the silver nanorods synthesised.

Deconvolution of each UV-Vis spectra was performed following the procedure detailed in Chapter 2, Section 2.4. This was necessary to obtain the correct wavelength and intensity of each plasmon absorption. Each spectra was baseline corrected prior to deconvolution. The results are shown in Figure 3.10 and the values obtained are presented in Table 3.1.

The relative intensities of the transversal and longitudinal plasmon bands

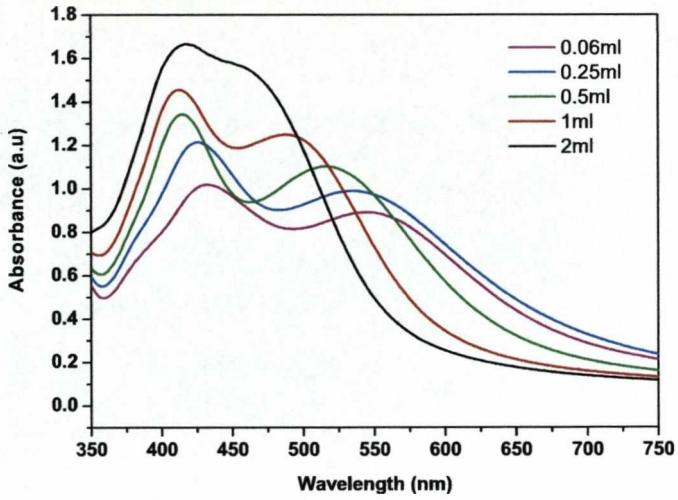


Figure 3.9: UV-vis spectra of silver nanorods showing the effect of changing the amount of 5nm seed employed (2, 1, 0.5, 0.25 and 0.06mL of seed solution.

in Figure 3.10 indicates that there is a high ratio of spherical nanoparticles to nanorods in the as-prepared solutions.

Table 3.1: Plasmon resonance positions of the UV-Vis spectra in Figure 3.10.

| | Plasmon Band | |
|---|---|---|
| Seed Amount | Tranversal(nm) | Longitudinal(nm) |
| 2000$\mu$L | 410 | 477 |
| 1000$\mu$L | 409 | 493 |
| 500$\mu$L | 414 | 520 |
| 250$\mu$L | 423 | 524 |
| 60$\mu$L | 429 | 549 |

The spectral changes observed, however, are not related to the relative intensities of the two plasmon bands but to their position. This shows that the amount of seed added influences the aspect ratio of the nanorods produced. For instance, when comparing the longitudinal plasmon band, a shift in the maximum from 549 to 477 nm is observed when increasing the seed concentration. The reason for this

must be related to a shifting of the length of the nanorods probably resulting from the different time dependence of the overall $Ag^+$ concentration during growth.

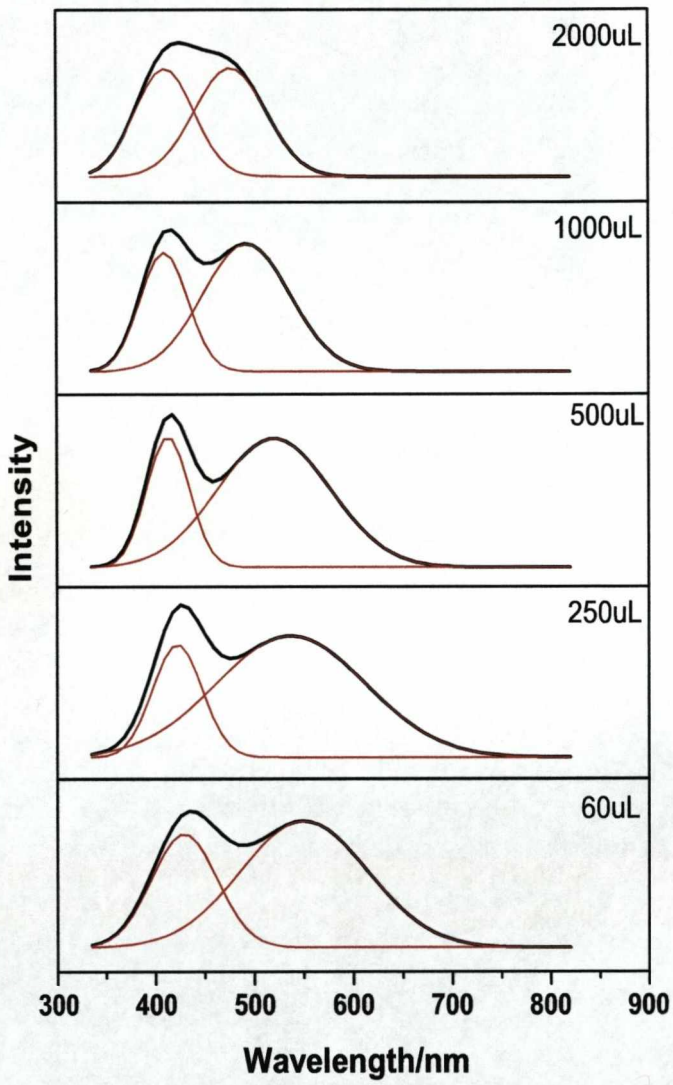


Figure 3.10: Deconvolution of the UV-Vis spectra from Figure 3.9.

### 3.3.4 TEM Characterisation

TEM images of silver nanorods produced after the addition of 125 $\mu$L and 500 $\mu$L citrate stabilised silver seed to a 10 ml growth solution of 0.25 mL of 10mM $AgNO_3$, 0.50 mL of 100mM ascorbic acid, and 10 mL of 80mM CTAB are shown in Figures 3.11 (a-d) and (e-g), respectively. Using the same method and growth solution, Murphy et al. [21] observed a high yield of uniform nanorods. The results presented here are typical of many attempts at Murphy's synthesis and it was not possible to reproduce their results. Although nanorods *were* formed the yield was poor with the majority of particles formed being spherical, Figure 3.11 (d). The size and shape of the nanorods varied significantly across the TEM grid, Figures 3.11 (a-c). Similar results were obtained by Lee et al. [42] but with a slightly higher degree of success than reported here.

The UV-Vis absorption spectra in Figure 3.9 clearly shows the appearance of a longitudinal plasmon resonance at high wavelengths for each seed concentration employed indicating the formation of nanorods in solution. However, it is also apparent from the relative intensities of the transversal and longitudinal plasmon bands in Figure 3.10, that there is also a significant proportion of spherical nanoparticles in solution. To separate the larger nanorods from the smaller spheres, each solution was centrifuged. It was expected that centrifugation would allow the separation of the nanorods from the spherical nanoparticles. This, however, was not the case and the method described by Murphy et al. [21] did not appear to be reproducible.

A large number of truncated triangular shaped nanoparticles were also present in solution for each seed concentration investigated. Similarly sized triangular shapes as those found here have a main plasmon absorption resonance at ~550 nm and a secondary band at ~430 nm attributed to the in-plane and out of plane dipole resonances, respectively [152]. The wavelength at which the former occurs is dependent on the size and shape of the particle [153]. Therefore, it is possible

that the plasmon resonance observed at higher wavelengths in Figure 3.9 is due to these triangular nanoparticles.

The stability of short aspect ratio gold nanorods is far greater than for similar sized silver nanorods [19–21, 28, 40, 149, 154]. This is reflected in the far greater number of research papers published for gold than for silver when investigating the contributing key factors to the anisotropic growth of nanorods. Murphy et al. [43] observed that gold nanoparticles of many different shapes are far more stable than those of silver, especially after purification from the reaction mixture.

Interestingly, it has been reported in a recent paper by Korgel et al. [155] that CTAB bought from different manufacturers with differing purities when employed in the seed mediated synthesis of gold nanorods significantly affected the shape and yield of the products formed with, in some cases, no nanorod formation being observed. The choice of CTAB was also seen to have an effect on the formation of the CTAB stabilised gold seeds formed indicating that the level of impurities in the CTAB significantly affects the products formed. There are open questions that need additional research. A discussion on the role of the anions in these preparations is presented in the next Chapter. It can be concluded that the method reported Murphy et al. requires a better control of the purity of the surfactant employed.

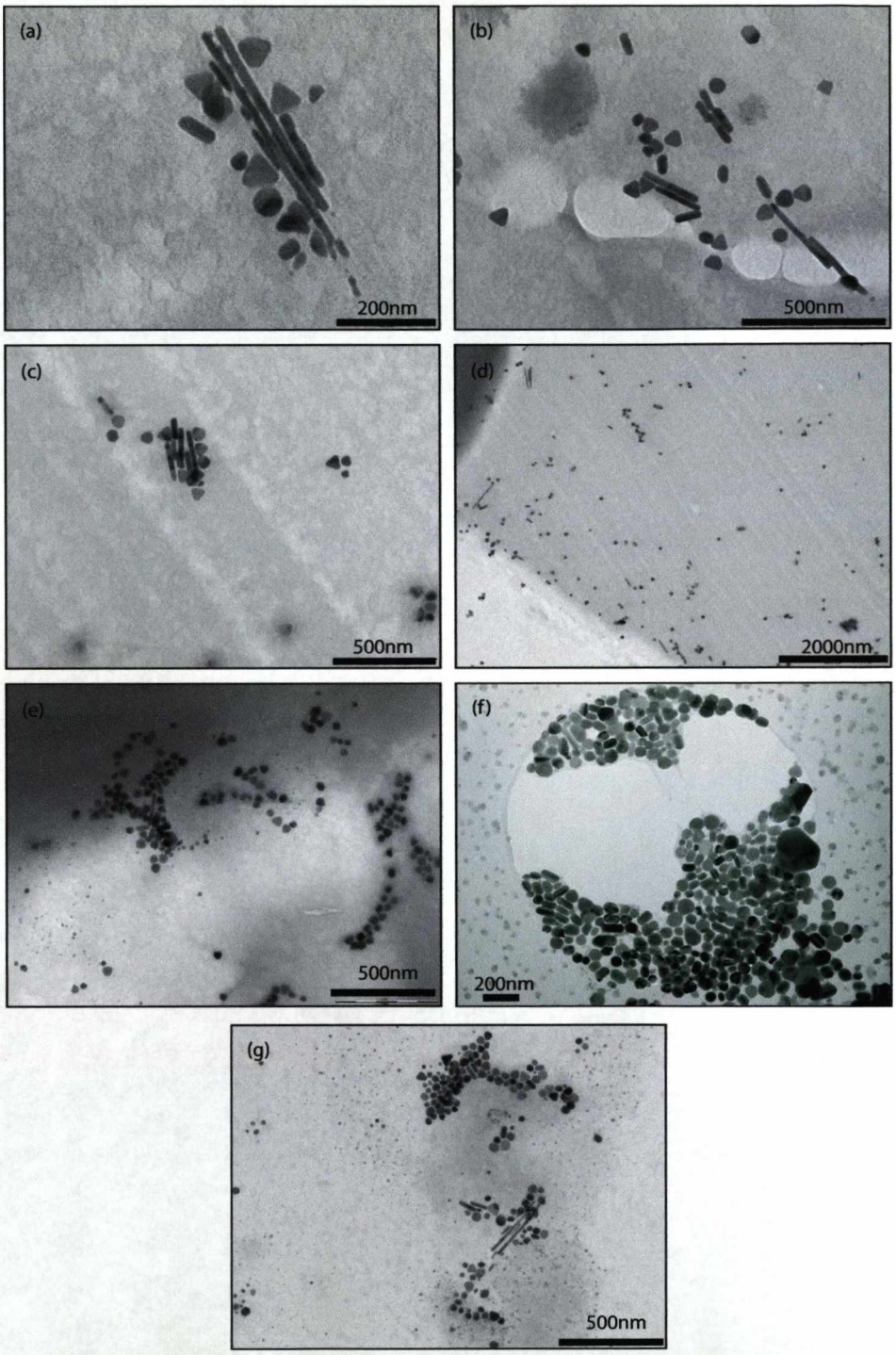


Figure 3.11: TEM images of silver nanorods grown by the addition of (a-d) 125 $\mu$L and (e-g) 500 $\mu$L of the citrate stabilised silver seed.

## 3.4 Summary

In this Chapter two synthetic methods for the preparation of gold and silver nanorods are described. The products obtained were characterised by UV-Vis spectroscopy and TEM.

CTAB stabilised gold nanorods with an average width and length of (54±11) nm and (21±11) nm, respectively, giving an average aspect ratio of 2.8±0.8 were synthesised employing a seed mediated surfactant stabilised method. From TEM images it was observed that the size, shape and aspect ratio of the nanorods changed significantly with varying concentrations of seed and silver nitrate within the growth solution. Time resolved UV-Vis spectroscopy showed that the gold nanorods elongate longitudinally first, increasing the aspect ratio and this is then followed by a widening, reducing the overall aspect ratio. The nanorods were stable in excess of two months.

A previously reported seed mediated method was employed for the synthesis of silver nanorods. UV-Vis spectroscopy showed the presence of a longitudinal plasmon resonance at higher wavelengths. TEM images failed, however, to show silver nanorods in the high yield expected. This was attributed to possible flaws in the separating of the rods from spheres in the centrifugation stage and to their low stability compared with gold. The chemical synthesis, although unsuccessful, served as a useful background for the electrochemical technique described later on.

# Chapter 4

# Ion Exchange Experiments

## 4.1 Introduction

This Chapter presents a study of the chemical synthesis of nanorods. These were the prefered materials of the Surface Enhanced Raman Spectroscopy experiments, presented in Chapter 7, since they provide a great enhancement of the electromagnetic field close to them.

Although the exact mechanism for the formation of metallic nanorods is still not fully understood, several hypotheses have been proposed. Most of the work in this field has concentrated on the formation of gold nanorods due to their greater stability compared with silver. As observed in the work carried out in this Thesis, the ability to successfully synthesise stable gold nanorods in a high yield was far greater than for silver.

During the formation of short gold nanorods, the presence of silver nitrate within the solution is crucial to produce a high yield, yet its concentration is not directly associated with the aspect ratio obtained [41]. In the absence of silver nitrate an aspect ratio of up to 25 has been observed but in very low yield [146]. The role of $AgNO_3$ however, is still not fully understood. The concentration of CTAB is also critical for nanorod growth with concentrations in excess of 80mM

being required, even though its critical micelle concentration (cmc) is far less than this value [43]. At such CTAB concentrations, the $Br^-$ concentration is so high that the addition of $AgNO_3$ should result in the observable formation of a AgBr precipitate. However, this was not observed. This has lead to the proposal that AgBr forms a monolayer in an epitaxial fashion on certain faces of the growing gold nanorod, thus inhibiting growth at these faces [31, 43]. Quantitative elemental analysis by Chen and co-workers on the surface of CTAB stabilised silver nanoplates showed an atomic ratio of 3:1 for Br and N, respectively. Since the ratio for a full CTAB monolayer should be 1:1, this unexpected difference was thought to be due to the formation of AgBr [31].

The steric effect by which CTAB acts as a growth directing agent has also been a matter of much debate. A study of mature gold nanorods using electron diffraction and HTREM showed the presence of two specific pairs of crystallographic zones, either (112) and (100) or (110) and (111), which are consistent with a cyclic penta-twinned crystal with five (111) twin boundaries arranged radially to the (110) direction of elongation [156]. On the basis of these results, Murphy et al. proposed that there is a small degree of preferential binding of the $CTA^+$ headgroup to the elongated (110) side faces [43]. This was considered to be due to the greater spacing of the Au atoms on the side faces which is comparable to the size of the $CTA^+$ head group, rather than that on the (111) end faces. From thermogravimetric and FTIR analysis, El-Sayed and co-workers [44, 65, 146] established that the surfactant used in the stabilisation and formation of silver and gold nanorods adopts a chemically adsorbed bilayer structure. The formation and stability of this bilayer is highly dependent on the length of the tail unit of the surfactant employed and this has a direct influence on the size and morphology of the shapes produced [40]. It has been proposed that this bilayer forms a close packed structure that not only increases the stability of the side faces but was also thought to sterically hinder the addition of any further metal ions. The

(111) end faces, however, have a significantly lower number of $CTA^+$ headgroups which allows further deposition of gold, thus increasing the length of the nanorods formed until the growth reagents in solution are depleted.

This proposal is further supported by the observed end to end assembly of gold nanorods through the use of the protein streptavidin. When gold nanorods are incubated in biotin disulphide, preferential binding is observed at the nanorod tips, which binds to the streptavidin linker creating a long chain assembly of nanorods [154].

The counter ion of the cationic surfactant employed has been shown to play a fundamental role in the formation of metallic nanorods [22, 31, 40–44, 157, 158]. In the synthesis of both silver and gold nanorods, the substitution of $Br^-$ by $Cl^-$ resulted in the production of only spherical gold nanoparticles. The cause of this is still not fully understood. Other workers have also found that anions play a very important role in nanocrystal growth [157].

As discussed above, the presence of bromide ions in CTAB could produce a AgBr precursor that assists nanorods formation. If this growth occurred from colloidal AgBr particles then the anisotropy in metal deposition to growing seeds should be lost since the reduction would not involve a surface orientation sensitive reaction. For this reason, two studies were performed in the present work. In the first, the $Br^-$ ion of CTAB was replaced by $NO_3^-$ through an ion-exchange reaction, to produce cetyltrimethylammonium nitrate (CTAN), which would not lead to the formation to an insoluble silver salt in the growth solution. Secondly, the overall $Br^-$ ion concentration was increased in preparations employing CTAB through the addition of KBr in order to alter the concentration of free $Ag^+$ ions in solution.

## 4.2 Chemicals and Materials

Amberlite© resin (IRA-400(Cl), BHD), sodium hydroxide ((NaOH, 96%), nitric acid ($HNO_3$), cetyltrimethylammonium bromide (CTAB, 99%) and potassium bromide (KBr, 99%) were purchased from Sigma and were used as received.

## 4.3 Experimental

### 4.3.1 Preparation of CTAN

Cetyltrimethylammonium nitrate (CTAN) was synthesised by an ion exchange reaction using CTAB as a starting compound using the following method. An ion exchange column was half filled with Amberlite© basic resin and through this 2 M NaOH was flushed under pressure to fully exchange the resin with $OH^-$. This process was repeated twice to ensure complete exchange with $OH^-$. The column was then rinsed through with ultra pure water (Milli-Q, Millipore) until a neutral pH was reached. Next, with the water level just above the start of the resin, an 80 mM CTAB solution heated to above 40°C to fully dissolve the surfactant, was pumped through the column under pressure. The presence of CTAOH in the eluent was detected by a large increase in pH. Once this had been observed the eluent was collected. This process was repeated until the required volume of CTAOH was obtained. If significant volumes were required the saturation of the column with $OH^-$ ions was repeated. The column was once again rinsed through with ultra pure water until a neutral pH was reached. The CTAOH solution formed by this process was neutralised by the careful addition of 0.5 M nitric acid. The as-prepared CTAN solution was then considered ready for use.

## 4.4 Formation of Silver Nanorods in CTAN Solution

The method of silver nanorods preparation was the same as described in Chapter 3, Section 3.3 but in this preparation CTAB was replaced by the as-prepared CTAN solution. All other experimental conditions remained the same. Two seed concentrations resulting from the addition of 60 and 125 $\mu$L of Ag seed (Section 3) were employed. The concentration of the CTAN solution was 65mM. The difference in the concentration compared with the original CTAB solution was probably due to the inaccuracy in determining the end point in the formation of CTAOH in the column and some dilution in the preparation.

### 4.4.1 Results and Discussion

Figure 4.1 shows the absorption spectra of the silver reduction products obtained when CTAB was replaced by CTAN with the addition of (a) 60 and (b) 125 $\mu$L of silver seed, respectively. In the presence of CTAB, two peaks are visible indicating the formation of silver nanorods but with the use of CTAN only one peak at ~400 nm was observed. This value is very close to that observed in the absorption spectra of the citrate stabilised silver seeds (Figure 3.7) (a).

When employing CTAB, during the growth phase of the silver nanorods, after the addition of the silver seed and NaOH, a gradual change in the colour of the growth solution was observed over a period of 10 - 30 minutes with the final colour depending on the silver seed concentration employed, indicating a change in the size and aspect ratio of the silver nanorods produced (Figure 3.8). When CTAN was used, however, a rapid colour change from dark green to brown to finally yellow was observed within 2 seconds of the addition of the silver seeds and NaOH. Furthermore, the turbidity of the growth solutions changed with the change in surfactant. For CTAB, at the end of growth the solution was cloudy

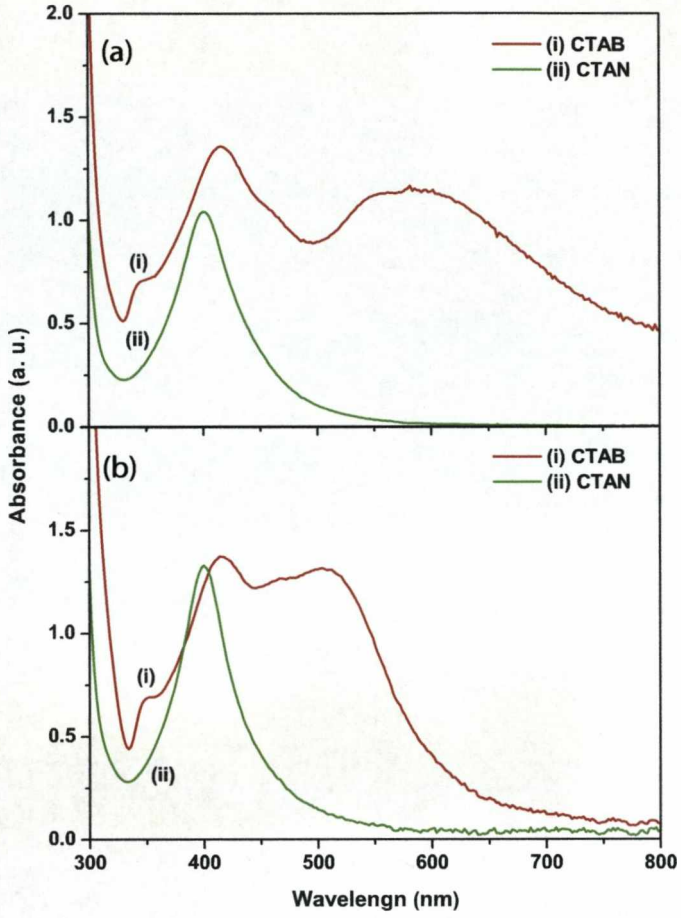


Figure 4.1: UV-Vis spectra of silver products for obtained for CTAB and CTAN with the addition of (a) 60 and (b) 125 $\mu$L citrate stabilised silver seed solution.

whereas for CTAN, the growth solution remained completely transparent.

The distinct lack of any secondary longitudinal plasmon band in Figure 4.1 indicates that no silver nanorods were produced when the $Br^-$ counter ion of CTAB was replaced by $NO_3^-$. Similar results were obtained when the $Br^-$ ion was replaced with $Cl^-$ [31, 42]. In the formation of silver nanoplates, Chen et at. [31] observed using UV-Vis spectroscopy, the presence of Ag-CTAB complexes in the absence of any reducing agent. These are most probably AgBr colloids stabilised by $CTA^+$. Similar spectroscopic results were obtained for Au-CTAC [159]. The use of $Cl^-$ should still result, however, in the formation of an insoluble colloidal

AgCl precursor. The silver-halide precursor appears to play a crucial role in the initial directional growth of the metallic seed employed and therefore, a change in the counterion which also leads to a insoluble silver complex should still result in nanorod formation; evidently this is not the case. The reason for using a soluble silver salt in this present study was to determine if the concentration of the free $Ag^+$ in solution controlled directional growth. The present results give a clear indication that nanorod formation is not influenced only by the presence of $CTA^+$. Further evidence of this is that the critical micelle concentration, degree of micelle ionisation and thermodynamic parameters for both CTAB and CTAN differ very little as shown in Table 4.1. If the anisotropic growth was simply due to $CTA^+$ then due to the similarities between both surfactants both should produce nanorods. Therefore, as proposed in the literature [22, 31, 40–44], it can be concluded that the presence of $Br^-$ is essential for nanorod growth.

Table 4.1: Critical micelle concentration (cmc), degree of micelle ionization ($\alpha$) and thermodynamic parameters for the CTAB and CTAN surfactants at 298.15 K. Data taken from Reference [160]

| | cmc (mM) | $\alpha$ | $\Delta H_{mic}$ (kJ mol$^{-1}$) | $\Delta G_{mic}$ |
|---|---|---|---|---|
| CTAB | 0.95±0.03 | 0.33±0.02 | -6.9±0.3 | -28.9 |
| CTAN | 0.89±0.03 | 0.31±0.02 | -7.8±0.5 | -29.4 |

The effect of increasing the concentration of the CTAN solution on the formation of silver nanorods was also investigated. Figure 4.2 shows the absorption spectrum of the silver reduction products formed when the concentration of the as-prepared CTAN solution was increased to 160mM by rotary evaporation. Although the intense band at ~400 nm is still present a weaker secondary absorbance was also observed at ~500 nm. The solution also appeared cloudy which was an

indication of nanorod formation. A similar absorption spectra was obtained by Kawasaki et al [161] for the synthesis of gold nanoparticles by the reduction of $AuCl_4^-$ by 2,2´ iminodiethanol in the presence of CTAN.

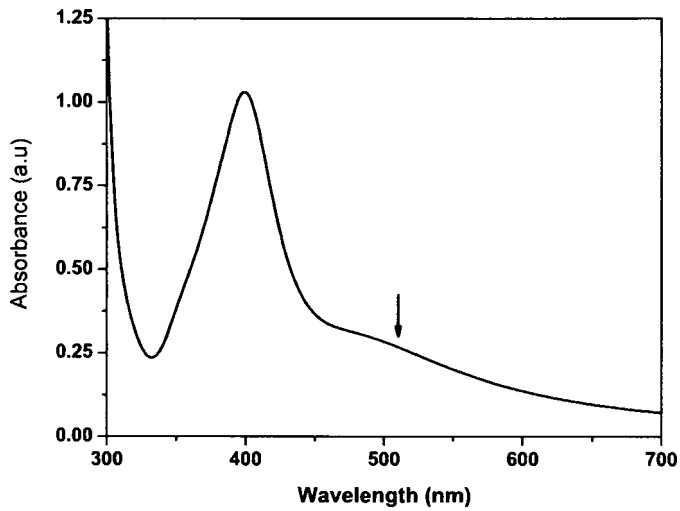


Figure 4.2: UV-Vis spectra of silver products formed using 160mM concentrated solution of CTAN.

The presence of a plasmon resonance at a higher wavelength is indicative of the formation of non-spherical nanoparticles. This second band is observed without the presence of any $Br^-$ ions in solution but its intensity is much less than the plasmon band at ~400 nm. The formation of any non-spherical silver nanoparticles in this solution is probably due to a soft template effect resulting from the large increase in CTAN concentration [20].

## 4.5 Nanorods Formation with Increased Bromide Concentration

In an attempt to demonstrate that the presence of a colloidal AgBr precursor in solution is essential for the anisotropic growth of silver nanocrystals and not just the total concentration of soluble silver, the concentration of $Br^-$ in the growth solution (consisting of CTAB, silver nitrate and ascorbic acid (Section 3)) was increased by the addition of KBr. A normal nanorod synthesis was then performed using 125 $\mu$L of the silver seed solution.

### 4.5.1 Results and Discussion

Figure 4.3 shows the absorption spectra of the silver reduction products formed when the overall $Br^-$ concentration in solution was increased. Initially, in the absence of any excess $Br^-$, two plasmon resonance bands were observed indicating the formation of nanorods, Figure 4.3 (a). When the concentration of excess $Br^-$ in solution was increased to 50mM a red shift in the position of the longitudinal plasmon band was observed, Figure 4.3 (b), and when the concentration was increased to 100mM the longitudinal plasmon band disappeared completely, Figure 4.3 (c). Clearly, an increase in the concentration of $Br^-$ favours spherical nanoparticle formation although the long absorbance tail observed indicates a variety of shapes and sizes.

If we consider the AgBr colloids as sources of $Ag^+$ in solution, then increasing the concentration of $Br^-$ should increase the availability of $Ag^+$ as complexes of composition $[AgBr_{n+1}]^{n-}$. Equations (4.1) to (4.4) show the complexes which can form along with their corresponding equilibrium constants [162].

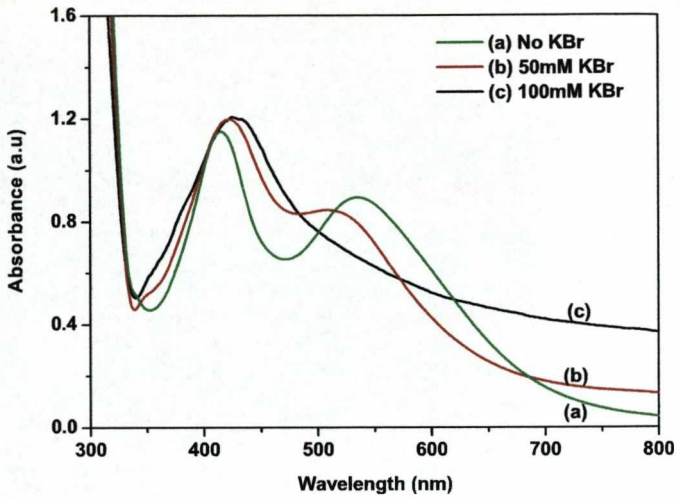


Figure 4.3: UV-Vis spectra of silver products obtained when the overall bromide concentration was increased (a) 0 mM, (b) 50 mM and (c) 100 mM by the addition of KBr.

$$Ag^+ + Br^- \rightleftharpoons AgBr \qquad K_1 = 5.35 \times 10^{-13} \tag{4.1}$$

$$AgBr + Br^- \rightleftharpoons [AgBr_2]^- \qquad K_2 = 1 \times 10^{-5} \tag{4.2}$$

$$[AgBr_2]^- + Br^- \rightleftharpoons [AgBr_3]^{2-} \qquad K_3 = 1 \times 10^{-4.13} \tag{4.3}$$

$$[AgBr_3]^{2-} + Br^- \rightleftharpoons [AgBr_4]^{3-} \qquad K_4 = 1 \times 10^{-3.22} \tag{4.4}$$

From Equations (4.1) to (4.4), the total concentration of silver in solution, including both free silver and complexes, $[Ag]_t$, is given by:

$$[Ag]_t = \frac{5.35 \times 10^{-13}}{[Br^-]} + 10^{-5}[Br^-] + 7.41 \times 10^{-5}[Br^-]^2 + 6.03 \times 10^{-4}[Br^-]^3 \tag{4.5}$$

From these values, the total concentration of free silver in solution under normal growth conditions was $7.31\times10^{-7}$ mol $dm^{-3}$, given by Equation 4.5. When the total bromide concentration was increased by 50 mM by the addition of KBr this increases the concentration of free silver slightly to $7.52\times10^{-7}$ mol $dm^{-3}$. This small change caused a slight red shift in the longitudinal plasmon band of the silver nanorods formed, Figure 4.3 (b) indicating a reduction in their aspect ratio. A decrease in the intensity of this band was also observed. When the total bromide concentration was increased to 100 mM, a large increase in the total concentration of free silver in solution to $2.31\times10^{-6}$ mol $dm^{-3}$ was calculated. This coincided with the disappearance of the longitudinal plasmon band in the absorption spectra, Figure 4.3 (c), indicating the formation of only spherical nanoparticles. Therefore, as the total concentration of free silver increases, the formation of spherical nanoparticles is favoured. However, it must also be considered that the addition of KBr also causes a decrease in the cmc, aggregation number and solubility of aqueous CTAB [163] which would greatly affect the anisotropic formation of nanorods.

These experiments show that, by themselves, neither the increase of $Br^-$ concentration nor that of silver in solution are determining factors in the formation of silver nanorods.

The exact mechanism for nanorod formation is still not fully understood and the work carried out here does not endeavour to propose such a mechanism. However, from the results presented here, we can further substantiate the proposed formation of colloidal AgBr precursors by Murphy, Chen and co-workers as an initial deposit which chemisorbs on specific faces of the silver seed.

Furthermore, if the anisotropic growth of silver nanorods was solely due to a soft template effect of the CTAB micelles in solution then increasing the amount of free silver should lead to an increase in the yield of nanorods formed. Since the opposite is observed then it is clear that other factors must contribute. It is

also clear that free $CTA^+$, or its specific adsorption, does not solely direct the formation of silver nanorods and it can be speculated that a combination of the selective absorption of CTAB on the (111) plane of silver seeds and the formation of AgBr leads to the anisotropic growth observed.

## 4.6 Summary

The effect of increasing total bromide concentration and the use of the surfactant cetyltrimethylammonium nitrate (CTAN) on the formation of silver nanorods is described. The products formed were characterised by UV-Vis spectroscopy. In the presence of CTAB two plasmon resonance bands were observed indicating the formation of silver nanorods. When CTAN was employed, however, the longitudinal plasmon resonance disappeared indicating the formation of only spherical nanoparticles. Since the use of CTAN leads to the formation of soluble silver nitrate in solution and no nanorod formation was observed, the formation of colloidal AgBr appears to be essential for the formation of nanorods; probably as an adsorbed layer on the growing structure.

# Chapter 5

# Electrochemical Nucleation and Orientation Experiments

## 5.1 Introduction

The electrochemical nucleation, deposition and growth of metal nanoparticles on electrode surfaces, although well documented [123,124,164–167], still continues to be a subject of great interest. As a method for the production of metal nanoparticles, electrochemical nucleation has many advantages over conventional chemical synthesis, namely the ability to control the rate of reaction by defining the applied interfacial potential and the ability to control the size of the nucleation center by altering the time of the applied potential [114, 168, 169]. A combination of these factors gives a unique opportunity to control both the density and size of the nucleating centers.

Various techniques have been developed to study experimentally the nucleation process. Cyclic voltammetry indicates the presence of nucleation by an enhanced peak separation and the appearance of a nucleation loop in the cathodic region. Once nucleation has been observed, potential step chronoamperometry allows the type of nucleation and reaction kinetics to be determined.

Before the methods for analysing nucleation and growth through current-time transients were developed, the number density of nuclei could only be determined by direct microscopic examination of the electrode surface. This was overcome by the introduction of various mathematical models which have been developed in order to establish a quantitative mechanism by which 3D nucleation and growth occurs [165, 167, 170, 171]. These mathematical models, however, still fail to provide an accurate determination of number density and growth parameters.

The initial aim of this part of the work was to investigate the optimum conditions for the electrochemical growth of nanoparticles at an electrode surface. Since the properties of nanoparticles vary as a function of size and shape, there is a need for a reliable method of synthesis capable of producing mono-disperse nanoparticles. An understanding of the mechanism of growth and the kinetics involved would undoubtedly facilitate the design of a reliable synthesis. This work formed the basis of a novel approach for the synthesis of cylindrical nanoparticles involving ultrasound.

The rate of nucleation can be described in two ways, instantaneous and progressive. If nucleation is instantaneous, the number of nuclei present on the surface at any time following the onset of deposition is constant. For progressive nucleation, however, new centers are formed continuously during the growth process and therefore, the number of nuclei increases continuously with time. For the growth of mono-disperse nuclei at the electrode surface, instantaneous nucleation is required.

## 5.2 Theory of Nucleation

In the early stages of metal deposition, the reaction rate and hence the number of nuclei formed is strongly dependent on the overpotential, where the applied

overpotential ($\eta$) is defined as:

$$\eta = E_f - E_0 \tag{5.1}$$

$E_0$ corresponds to the equilibrium potential of the system being studied and $E_f$ is the applied potential which is more negative than $E_0$.

Metal electrodeposition onto an electrode surface occurs in two stages. The initial step involves the formation of nuclei which grow independently of each other. It was first proposed that this growth of nuclei under diffusional control was a one-dimensional process. However, it was later realised that due to the small size of the nuclei being formed, the growth was best described by localised spherical diffusion [125]. The second stage is the subsequent overlap of the growth centers. If the number density of growing nuclei is large enough, a compact electrodeposited film is formed and this latter step is controlled by linear diffusion following the Cottrell equation.

Quantitative electrochemical techniques such as chronoamperometry and cyclic voltammetry, allow the kinetics of nucleation to be investigated by observing the corresponding current response to a particular waveform. Potential step experiments, in particular, allow the determination of diffusion coefficients, nucleation rate constants and nucleus number density. A typical $j - t$ transient is shown in Figure 5.1.

The initial decrease in current is a result of reorganisation of the electrical double layer, where a new charge distribution equilibrium is reached and a charging current flows at the interface [171] and the growth of a distribution of sub-critical sized clusters on the electrode surface. Immediately after double layer charging is complete, a minimum current is observed followed by a rising current associated with the growth of the nuclei on the electrode surface. The minimum in the current observed results from the combination of the decaying transient described above and the growth of nuclei of size larger than the critical radius. The rise

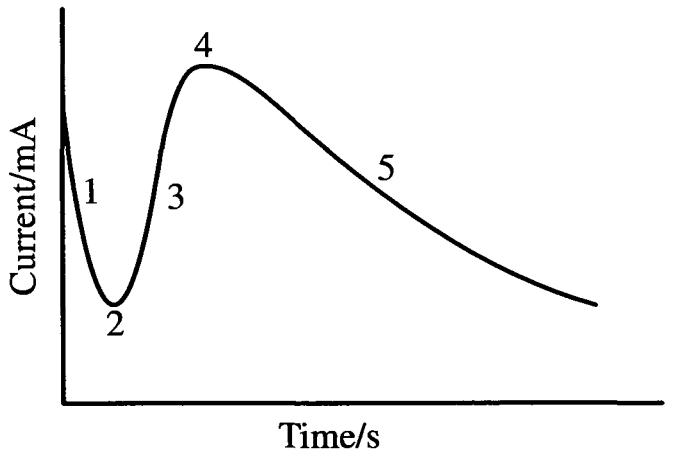


Figure 5.1: A typical current-time transient, 1; double layer charging region; 2; minimum current; 3; nucleus-growth current; 4; maximum peak current determined by the overlap of the diffusional fields of the growing nuclei; 5; linear diffusion-limiting current [171].

in current reaches a maximum value, $I_m$, at time $t_m$, due to the change in diffusional geometry from spherical to linear. The time of this maximum depends on the overpotential employed. Finally, a decreasing diffusion-limiting current is observed due to the onset of linear diffusion.

In the early stages of deposition, the relationship between current, $I$, and time, $t$, is given by:

$$I = \alpha t^x \tag{5.2}$$

where $x$ depends on factors such as the type of nucleation (instantaneous or progressive) and the geometry of the crystallite being formed. Allongue et al. [127] modeled expressions for a variety of cases along with the corresponding values of $x$.

For mass transport controlled growth of nuclei, the current, $I$, at time $t$, for a fixed number of crystallites, $N$, growing by hemispherical diffusive flux is given by [165]:

$$I(t) = \frac{\mathrm{zF}\pi(2Dc)^{3/2}\mathrm{M}^{1/2}Nt^{1/2}}{\rho^{1/2}} \tag{5.3}$$

where zF is the molar charge of the depositing species, $D$ is the diffusion coefficient, $c$ is the concentration in mol $cm^{-3}$, M is the molecular weight of nucleating species and $\rho$ is its density. This is referred to as instantaneous nucleation, where effectively all the nuclei are the same age and grow at the same rate.

In the case of progressive nucleation the current at a given time is given by:

$$I(t) = \frac{2zFAN_{\infty}\pi(2Dc)^{3/2}M^{1/2}t^{3/2}}{3\rho^{1/2}} \tag{5.4}$$

where $N_{\infty}$ is the maximum nuclear number density and $A$ is the steady state nucleation rate.

In both cases of instantaneous and progressive nucleation, as the depletion zones surrounding each growing nucleus start to overlap, the transient current is expected to decay following planar diffusional control given by the Cottrell equation [172]:

$$I(t) = \frac{nFcD^{1/2}}{\pi^{1/2}t^{1/2}} \tag{5.5}$$

Scharifker and Hills [164, 165] developed a non-dimensional model to describe hemispherical nucleation and diffusion controlled growth using an extension of the Avrami Theorem [173]. If we consider a random set of hemispherical nuclei growing under diffusion control, then the radius, r, of each growth center as a function of time is given by:

$$r(t) = (kDt)^{1/2} \tag{5.6}$$

where $k$ is a numerical constant determined by the experimental conditions. At short times the current can be expressed by Equation 5.3. However, as the nuclei overlap the diffusional fields become linear. The corresponding current can then

be expressed as linear diffusion of a single diffusive zone given by:

$$S(t) = \pi k D t \tag{5.7}$$

If at t=0, $N$ centers are instantaneously nucleated then at a later time, $t$, the fraction of area covered by the diffusion zones is given by:

$$\theta_{frac} = N\pi k D t \tag{5.8}$$

Using the Avrami Theorem [173], the actual area of the the electrode, $\theta$ can be related to, $\theta_{frac}$, where $\theta_{frac}$ is the fraction of area that would be covered by diffusional zones in the absence of any overlap. The law of conservation of mass requires that the amount of material entering the diffusion zones is equal to the amount being incorporated into the growing nuclei. Therefore, the current for the whole electrode is given by:

$$I = \frac{\mathrm{zF}D^{1/2}c}{\pi^{1/2}t^{1/2}}[1 - exp(-N\pi k D t)] \tag{5.9}$$

Assuming that at very short times the fraction of the electrode area covered by diffusion zones is $\ll 1$ i.e., considering that no overlap is occurring, Equation 5.9 becomes:

$$I = \mathrm{zF}D^{3/2}c\pi^{1/2}Nkt^{1/2} \tag{5.10}$$

Since this current density must equal that for $N$ isolated hemispherical nuclei, Equation 5.3, then for instantaneous nucleation, parameter $k$ equates to:

$$k = \left(\frac{8\pi c\mathrm{M}}{\rho}\right)^{1/2} \tag{5.11}$$

For progressive nucleation,

$$N(t) = AN_{\infty}t \tag{5.12}$$

and

$$\theta_{frac} = \int_0^t AN_{\infty}\pi k^{'} Dtdt = AN_{\infty}\pi k^{'} Dt^2/2 \tag{5.13}$$

It follows that

$$I = \frac{2\mathrm{zF}D^{1/2}c}{\pi^{1/2}t^{1/2}}[1 - exp(-AN_{\infty}\pi k' Dt^2/2)] \tag{5.14}$$

and $k^{'}$ can again be evaluated in the limit $AN_{\infty} \rightarrow 0$ and by comparison with Equation 5.4. For progressive nucleation:

$$k^{'} = \left(\frac{4}{3}\right)\left(\frac{8\pi c\mathrm{M}}{\rho}\right)^{1/2} \tag{5.15}$$

A plot of Equations 5.9 and 5.14, produces, in both cases, a maximum value of the current, $I_m$ at a time, $t_m$. Equating the first derivative of both these equations to zero produces solutions for the maximum for each type of nucleation. This enables the density of nuclei and the rate of nucleation to be calculated.

For instantaneous nucleation:

$$t_m = \frac{1.2564}{N\pi kD} \tag{5.16}$$

$$I_m = 0.6382\mathrm{zF}Dc(kN)^{1/2} \tag{5.17}$$

$$I_m^2 t_m = 0.1629(\mathrm{zF}c)^2 D \tag{5.18}$$

For progressive nucleation:

$$t_m = \left(\frac{4.6733}{AN_\infty \pi k' D}\right)^{1/2} \tag{5.19}$$

$$I_m = 0.4615\mathrm{zF}D^{3/4}c(k'AN_\infty)^{1/4} \tag{5.20}$$

$$I_m^2 t_m = 0.2598(\mathrm{zF}c)^2 D \tag{5.21}$$

The product term $I_m^2 t_m$ is an excellent diagnostic tool to determine the type of nucleation occurring since its value is independent of the nucleation and growth rates. Alternatively, the transient can be plotted in their dimensionless form of $I_m/I_m^2$ vs $t/t_m$ and by direct comparison to their theoretical expression given by Equations 5.22 and 5.23 for instantaneous and progressive nucleation, respectively. Inserting values, the nucleation transients are described by:

$$\frac{I^2}{I_m^2} = \frac{1.9542}{t/t_m}[1 - exp(-1.2564(t/t_m))]^2 \tag{5.22}$$

$$\frac{I^2}{I_m^2} = \frac{1.2254}{t/t_m}[1 - exp(-2.3367(t/t_m))]^2 \tag{5.23}$$

Figure 5.2 shows the limiting cases of instantaneous and progressive nucleation resulting from equations 5.22 and 5.23.

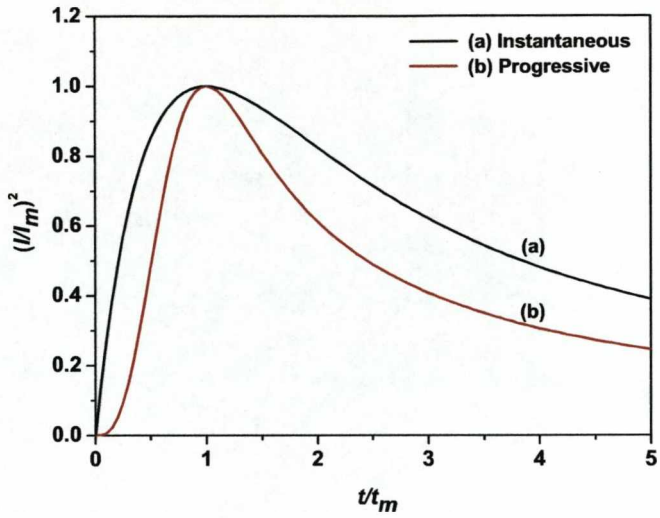


Figure 5.2: Non-dimensional $(I/I_m)^2$ vs $t/t_m$ plots for (a) instantaneous and (b) progressive nucleation.

## 5.3 Chemicals and Materials

Silver nitrate ($AgNO_3$, 99.999%), silver perchlorate monohyrdate ($AgClO_4 \cdot H_2O$, 99.999%), tri sodium citrate dehydrate ($Na_3C_6H_5O_7$, 99+% A.C.S), sodium perchlorate ($NaClO_4$, 99.0%), perchloric acid ($HClO_4$, 70% A.C.S) and polyvinylpyrrolidone (PVP, average $M_w$=55,000) were purchased from Aldrich. All glassware was cleaned prior to use using freshly prepared aqua regia (1:3 $HNO_3$:HCl) followed by repeated rinsing with ultra pure Milli-Q water.

## 5.4 Experimental

Details of the experimental setup and cell are given in Sections 2.5 and 2.5.3, respectively. In all experiments the working electrode was a platinum disk with an area of 0.188 $cm^{-2}$ and the counter electrode was a platinum gauze placed close to the working electrode. A saturated mercury sulphate electrode (MSE)

was employed as a reference electrode and all potentials are quoted with respect to this. The same cell was used for both cyclic voltammetry and chronoamperometry experiments. Prior to measurement, the working electrode was polished using progressively finer alumina slurries until a mirror finish was achieved and then cleaned in an ultrasonic bath. No electrochemical pre-treatment was employed.

## 5.5 Orientation Experiments

As an initial basis to the experimental sonoelectrochemical work discussed later on, an extensive series of preliminary experiments were conducted. The aim of these was to determine the conditions needed for nucleation and, more critically, stabilisation of the nanoparticles prepared. A number of different solution at differing concentrations with various stabilising agents were investigated. The investigation of systems without the addition of a base electrolyte were conducted to aid the formation of dendritic growth at the electrode surface, which the presence of a base electrolyte eliminates. Each system studied was characterised by cyclic voltammetry and potential step experiments.

### 5.5.1 1 mM $AgNO_3$ + 5 mM tri-sodium citrate

Cyclic voltammetry was used to determine the potential region in which silver electrodeposition occurs, Figure 5.3. From a starting potential of 0.3 V two peaks are clearly present. The first, $P_c$, corresponds to the reduction of the silver ions, with the deposition of silver starting at a critical potential, $E_{CRIT}$, of ~120 mV. On reversing the scan a second peak, $P_a$ appears corresponding to the oxidation of the previously deposited silver ions. This stripping peak occurs at ~0 mV.

The oxidation peak exhibits a sharp decrease in current after the peak maximum, which is typical of anodic stripping and is due to the depletion of the metal deposit [126], however, initially the onset of ohmic control is observed. The cur-

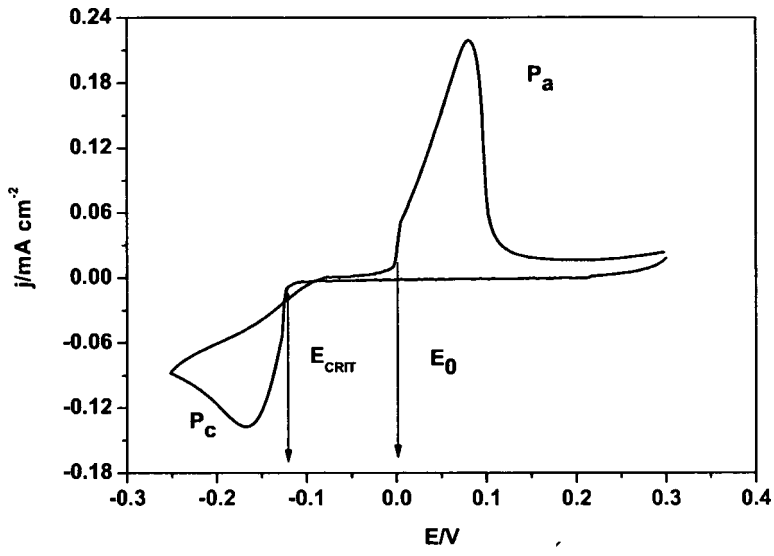


Figure 5.3: Typical CV curve obtained in a Pt/1 mM $AgNO_3$ + 5 mM Tri-sodium Citrate system. The potential scan started at +0.3 V toward the negative direction and then reversed at -0.25 V. $\nu$ = 10 mV/s.

rent due to the oxidation of Ag $\rightarrow$ $Ag^+$ should should grow exponentially but, at some value, this is limited by the formation of an insoluble Ag-citrate film. A characteristic nucleation loop is also present. The equilibrium redox potential for $Ag/Ag^+$ in the solution was -0.023 V vs MSE.

From the CV, the diffusion coefficient can be calculated from [174]:

$$j_p = 0.61(n\mathrm{F})^{3/2}(\mathrm{RT})^{-1/2}D^{1/2}c\nu^{1/2} \tag{5.24}$$

where $j_p$ is the current density of the cathodic peak, F is the faraday constant, $n$ is the number of electrons transfered, R is the gas constant, $T$ is the temperature in Kelvin, $D$ is the diffusion co-efficient, $c$ is the bulk concentration in mol cm$^{-3}$ and $\nu$ is the sweep rate in Vs$^{-1}$. A value of $D_{Ag^+}$ = 1.40×10$^{-5}$ cm$^2$s$^{-1}$ was calculated. This is in reasonably good agreement with the literature value of

$1.70 \times 10^{-5}$ $cm^2 s^{-1}$ [175]. The slight difference is most probably due to coordination by citrate.

The parameters obtained from the cyclic voltammogram were employed for the chronoamperometric study. Taking $E_{CRIT}$ as the nucleation potential, a potential cathodic of this value and close to the equilibrium potential was chosen as the starting potential so that no nucleation and growth would take place. From this value, the potential was then stepped to a value more negative than $E_{CRIT}$ so that nucleation would occur and this was repeated with increasingly more negative values. Figure 5.4 shows the $j - t$ transients measured.

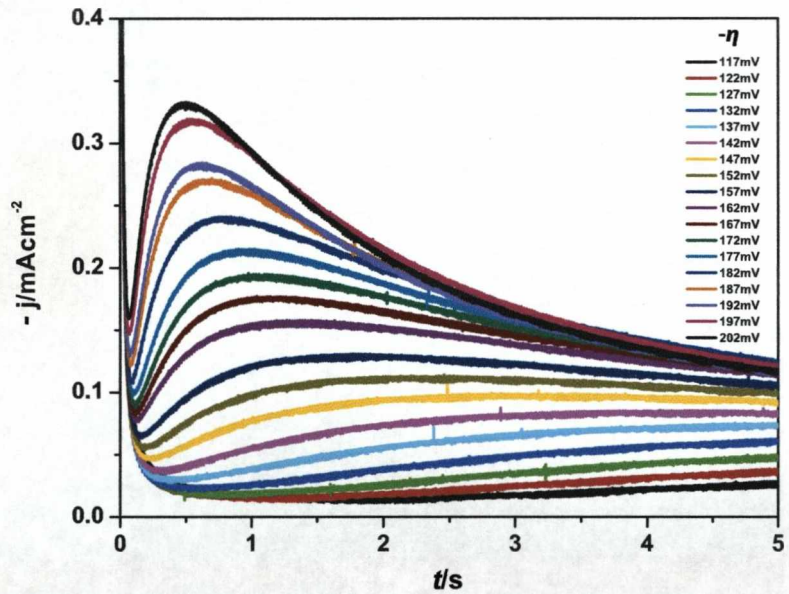


Figure 5.4: A set of experimental current time transients recorded in a Pt/1 mM $AgNO_3$ + 5 mM tri-sodium citrate system at the different overpotentials indicated in the Figure.

The transients observed are typical of 3-D nucleation controlled by hemispherical diffusion and therefore, can be investigated using the theory set out in Section 5.2. Equation 5.3 predicts that for instantaneous nucleation the rising part of the transient should be a linear function of $t^{1/2}$. Figure 5.5 shows that this is indeed the case but the currents extrapolate to a positive intercept on the time

axis and this intercept is potential dependent [164]. This is due to the difference in the nucleation times at different potentials which appears as a shift in the time scale

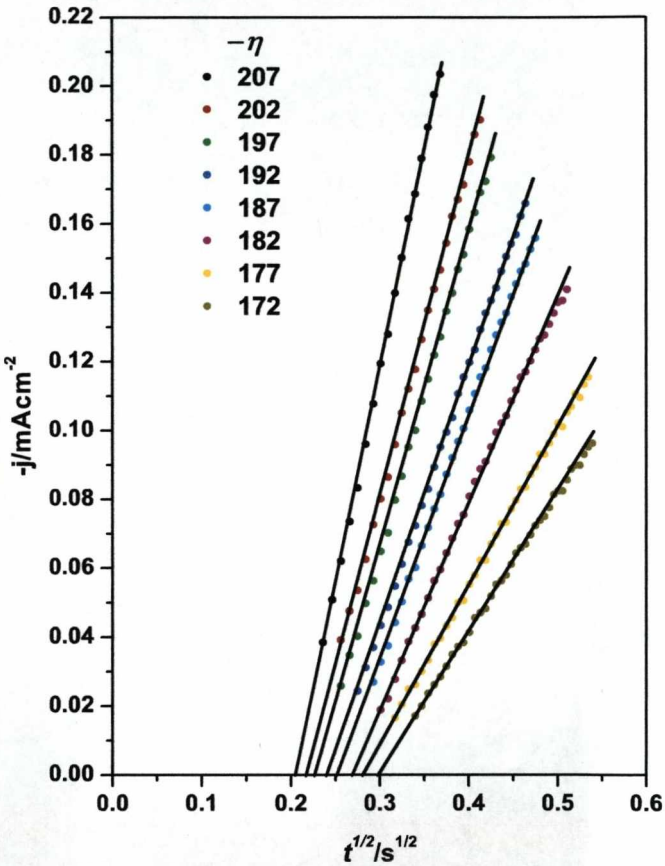


Figure 5.5: Plots of $j$ vs $t^{1/2}$ taken from the middle, rising current sections of the transients in Figure 5.4.

The reduced variable plot in Figure 5.6 shows that the nucleation of silver on platinum from this system follows that predicted for instantaneous nucleation for both low (157 mV) and high (207 mV) overpotentials. At low overpotentials the experimental values fit the theory extremely well but at higher overpotentials, there are slight deviations at both short and at long times where the current does

not decay according to the Cottrell equation. This is due to the limitations in the theory which cannot model accurately the processes occurring during growth.

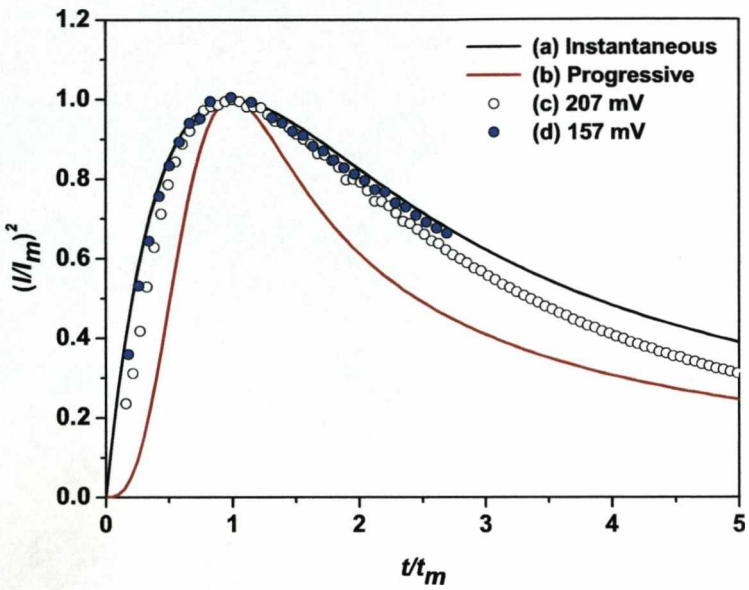


Figure 5.6: Non-dimensional $(I/I_m)^2$ vs $t/t_m$ plots for (a) instantaneous nucleation and (b) progressive nucleation and for an overpotential of (c) 207 mV and (d) 157 mV.

As discussed earlier, the product term $I_m^2 t_m$ should be independent of the nucleation and growth rates and therefore, this quantity should be independent of the overpotential. However, Table 5.1, shows that this is not the case and an increase in its value with increasing overpotential is observed.

From Equations 5.18 and 5.21 the term $I_m^2 t_m$ should be $7.09 \times 10^{-8}$ A$^2$ cm$^{-4}$s and $1.13 \times 10^{-7}$ A$^2$ cm$^{-4}$s for instantaneous and progressive nucleation, respectively. The mean value obtained $(5 \pm 1) \times 10^{-8}$ A$^2$ cm$^{-4}$s is close to that for instantaneous nucleation. The diffusion coefficient can be obtained from Equation 5.18 and a value of $(3.1 \pm 0.7) \times 10^{-5}$ cm$^{-2}$ s$^{-1}$ was obtained. This differs from that calculated from the Cottrell equation by pulsing to a high overpotential,

Table 5.1: Analysis of the current maxima. Data taken from Figure 5.4.

| $-\eta$ (mV) | $-10^4 I_m$ ($Acm^{-2}$) | $t_m$ (s) | $10^7 I_m^2 t_m$ ($A^2cm^{-4}s$) | $10^5 N$ ($cm^{-2}$) |
|---|---|---|---|---|
| 157 | 1.30 | 1.85 | 31.4 | 1.27 |
| 162 | 1.56 | 1.38 | 33.8 | 1.83 |
| 167 | 1.76 | 1.27 | 39.3 | 2.32 |
| 172 | 1.94 | 1.12 | 41.9 | 2.82 |
| 177 | 2.13 | 0.94 | 42.2 | 3.39 |
| 182 | 2.40 | 0.80 | 45.9 | 4.33 |
| 187 | 2.70 | 0.71 | 51.5 | 5.48 |
| 192 | 2.83 | 0.62 | 49.7 | 6.01 |
| 197 | 3.18 | 0.54 | 54.7 | 7.59 |
| 202 | 3.32 | 0.52 | 56.8 | 8.26 |
| 207 | 3.86 | 0.45 | 66.3 | 11.2 |

$D_{Ag^+} = (4.7 \pm 0.5) \times 10^{-5}$ cm$^{-2}$ s$^{-1}$. Both of these calculated values are higher than that obtained from Equation 5.24. This indicates limitations to the theory laid out early in the Chapter.

From the current maxima and equation 5.17, the corresponding nuclear densities for each overpotential can be calculated and these values are also shown in Table 5.1. As expected, the number of nuclei increases significantly with increasing overpotential.

### 5.5.2 5 mM $AgNO_3$ + 10 mM tri-sodium citrate

Due to the small current densities observed for the 1 mM $AgNO_3$ in the 5 mM tri-sodium citrate system, a higher concentration of silver nitrate was investigated. The concentration ratio of silver to citrate could not be kept constant due to the solubility limit of silver citrate at high citrate concentrations.

The redox potential of the $Ag/Ag^+$ electrode was -33.8 mV. Both the cyclic voltammograms and the $j - t$ transients are similar to those obtained for 1 mM $AgNO_3$ but, as expected, there is a noticeable increase in the current density. From equation 5.24, $D_{Ag^+} = 7.89 \times 10^{-6}$ cm$^2$s$^{-1}$, a value lower than that previously

calculated. This can be attributed to the higher concentration of citrate in the solution. The citrate ion is large compared to that of $Ag^+$ and therefore, the diffusing species will have a size determined by the coordination of Ag by citrate. Citrate is a tri-dentate ionic ligand binding through the three carboxylate groups. The low value of $D_{Ag^+}$ could be due to strong solvation of the carboxylate groups and also the possible formation of aggregates in solution through the multidentate ligand. This system had a molar ratio of 1:2 silver:citrate; when a similar system was investigated, consisting of 8mM $AgNO_3$ + 20mM tri-sodium citrate, a molar ratio of 1:2.5, a diffusion coefficient of $8.39\times10^{-6}$ $cm^2s^{-1}$ was calculated. Since the solution had an increased concentration of citrate to silver, as mentioned before, a decrease in the diffusion coefficient should have been expected but a small increase was observed. The origin of this small difference is unclear at present.

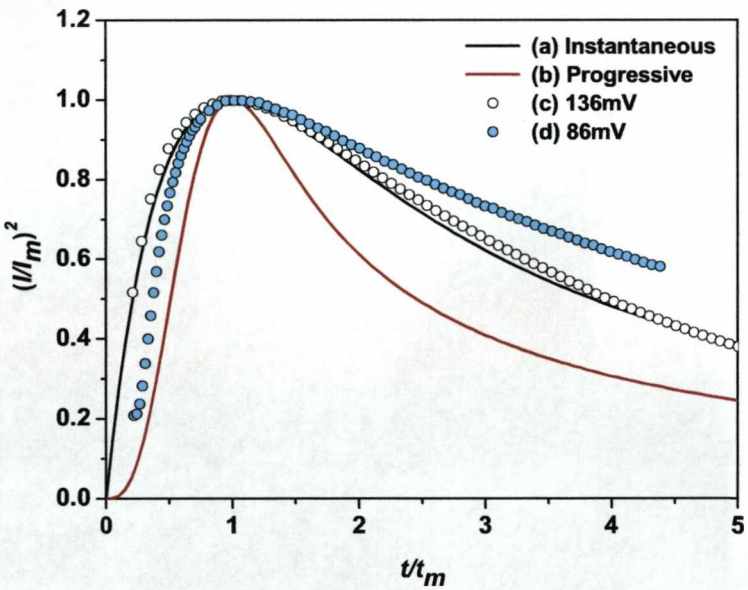


Figure 5.7: Non-dimensional $(I/I_m)^2$ vs $t/t_m$ plots for (a) instantaneous nucleation and (b) progressive nucleation and for an overpotential of (c) 136 mV and (d) 86 mV .

The dimensionless plots for overpotentials of 136 mV and 86 mV along with the corresponding predicted plots for instantaneous and progressive nucleation are shown in Figure 5.7. From the results for an overpotential of 86 mV it is unclear which type of nucleation is occurring. At short growth times the response is close to that of progressive nucleation, but at longer times the transient follows that predicted for instantaneous nucleation. As time progresses, the decaying section does not follow that predicted by the Cottrell equation. As the overpotential is increased to 136 mV, the agreement with the behaviour corresponding to instantaneous nucleation is excellent, both initially and at longer times. Since at lower overpotentials the rate of nucleation and growth is slower than that at higher overpotentials this uncertainty in the type of nucleation could be related to the kinetics of electrodeposition limited by coordination to citrate.

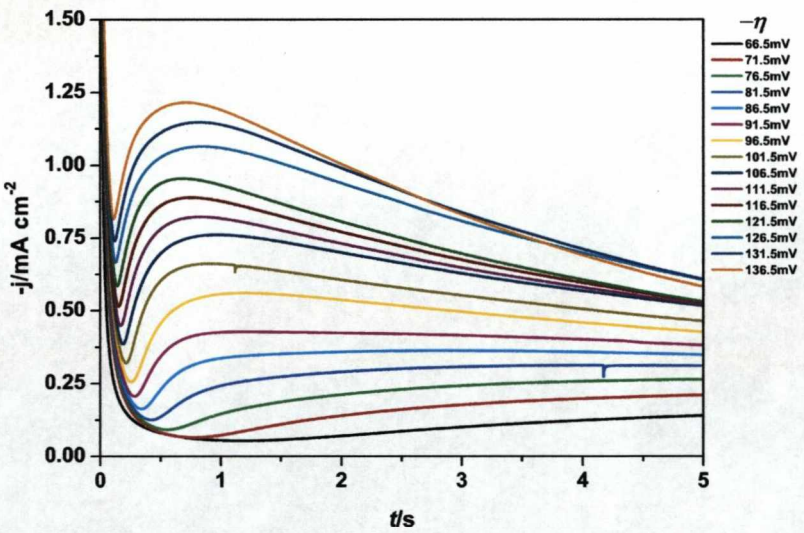


Figure 5.8: A set of experimental current time transients recorded in a Pt/5 mM $AgNO_3$ + 10 mM tri-sodium citrate system at the different overpotentials indicated in the Figure.

From the analysis of the current and time maxima from the transients in Fig-

ure 5.8, $D_{Ag^+} = 1.27\times10^{-5}$ $cm^2s^{-1}$ and $7.95\times10^{-6}$ $cm^2s^{-1}$ for instantaneous and progressive nucleation respectively. The value calculated for progressive nucleation is in excellent agreement with that calculated from the CV. However, this contradicts the results from the dimensionless plots where a good correlation with instantaneous nucleation was observed. It is worth noting that the calculation of the diffusion coefficient from Equation 5.24 does not incorporate any nucleation processes and is on a much smaller time-scale compared with the potential step experiments. The value obtained from the $j-t$ transients for instantaneous nucleation, of $1.27\times10^{-5}$ $cm^2s^{-1}$, is close to that value obtained in Section 5.5.1 for 1 mM $AgNO_3$ + 5 mM tri-sodium citrate solutions.

Further investigation was performed by means of double potential step experiments (Section 2.2.2). Briefly, the electrode was held at a potential anodic to the redox potential so that no nucleation occurs. The potential was then stepped for a set time usually in the millisecond range, to a value determined from the CV where spontaneous nucleation will occur. The potential is then stepped again to a value where no further nucleation can occur, but cathodic of the $Ag/Ag^+$ redox potential so that growth of the nuclei can be observed. Ueda et al. [168] indicated that this value should be between 15-20mV more negative than the redox potential of the system being investigated.

The number density and size of the nuclei produced can be controlled by altering the nucleation and growth conditions employed. Ueda and Sandmann [168, 169] have shown this with great success in the nucleation of silver clusters on ITO surfaces, where highly monodiperse nuclei were formed.

The $j-t$ transients observed in the double potential step experiments give a good indication of the type of growth occurring. Once nucleation has taken place during the initial short nucleation pulse, an anodic peak should be observed when the potential is switched from $E_1$ to $E_2$, associated with the dissolution of the nuclei which are not large enough to grow at $E_2$. The remaining nuclei which *are*

large enough, continue to grow.

The relationship between overpotential and this critical radius is given by [176]:

$$r_c = -\frac{2\sigma V_m}{z\eta \mathrm{F}} \tag{5.25}$$

$\sigma$ is the surface tension, $V_m$ is the molar volume, z is the charge number and $\eta$ is the applied overpotential. As the overpotential is increased, the critical size of the nuclei decreases.

For hemispherical growth, this should coincide with an increase in the measured current with time until a maximum is reached when overlap of the hemispherical diffusional fields occurs. For the growth of cylindrical, rod shaped structures, after a short increase, a constant current response should be observed. This corresponds to an initial stage where 3-D nucleation of hemispherical centers occurs, followed shortly by 1-D linear diffusional growth. Figure 5.9 shows the current transients measured for different values of $E_1$, $E_2$ and $t_1$ (Section 2.2.2).

Figure 5.9 (a) shows the effect of increasing the nucleation potential from -200 mV to -300 mV. The inset in the Figure shows the corresponding increase in current density in the nucleation region. Figure 5.9 (e) shows the growth region in greater detail. As the potential is increased a constant current is observed at a much shorter time indicating a change in the growth geometry from 3-D to 1-D.

Figure 5.9 (b) shows the effect of increasing the growth potential whilst keeping the nucleation potential constant and details of this transient are shown in Figure 5.9 (f). With only a slight increase of 10 mV, from -110 mV to -120 mV, a noticeable increase in the growth current is observed. This clearly shows how sensitive the current response is to only a slight change in potential. However, an anodic peak following the nucleation pulse is also visible at both potentials indicating that the nucleation potential was insufficient to compensate for the dissolution effect when the growth potential is applied. The presence or absence of an anodic peak and, more quantitatively, its intensity and area under the peak

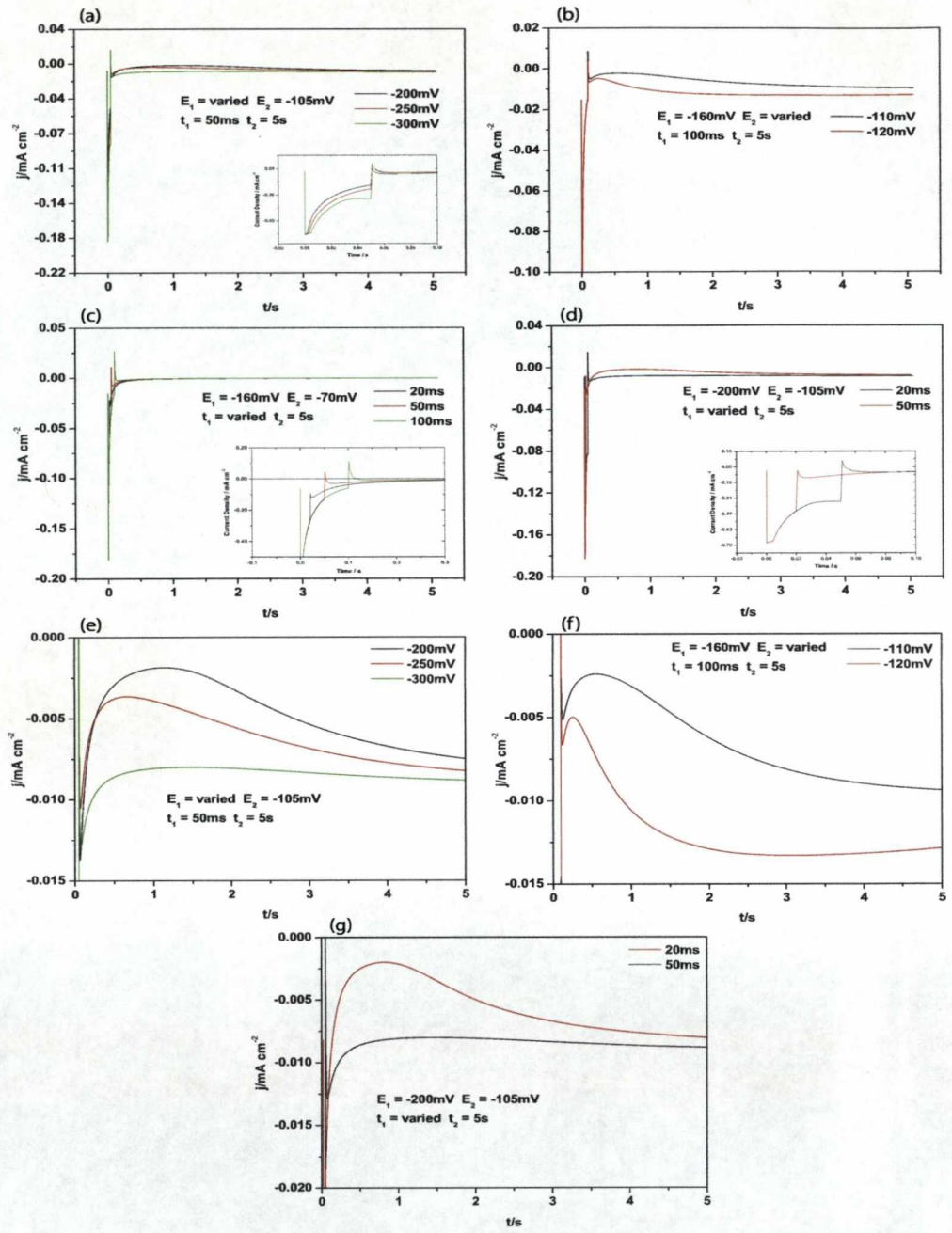


Figure 5.9: Current responce to the change in the parameters (a) $E_1$, (b) $E_2$ and (c)-(d) $t_1$ for the system Pt/5 mM $AgNO_3$ + 10 mM tri-sodium citrate. The insets on each $j - \bar{t}$ transient show the current response at shorter times. Figures (e), (f) and (g) show the current responses of (a), (b) and (d), respectively, in more detail.

are a complex method for measuring the number of sub-critical particles with respect to the number of stable particles [168].

Figures 5.9 (c) and (d) show the effects of varying the nucleation pulse time on the current response. The results in (c) show that no growth current is observed even by increasing the growth time from 20 ms to 100 ms. This is due to the growth potential, $E_2$, being too close to the redox potential of the system and simple dissolution of the nuclei is occurring upon switching to this potential. By contrast, in Figures 5.9 (d), the growth potential is sufficiently cathodic to allow growth. Figure 5.9 (g) shows that by increasing the nucleation time from 20 ms to 50 ms a constant current response is observed which is a possible indication of 1-D linear diffusional rod formation.

The results above clearly demonstrate that even very subtle changes in the parameters employed in double pulse chronoamperometry causes significant effects to the nucleation and growth of nuclei. Critically, the use of the correct nucleation potential is essential. This requires the potential to be sufficiently cathodic to nucleate a high number of stable particles but not too cathodic so that the individual identity of the growing nuclei is preserved. Similarly, the nucleation time needs to be sufficiently long to nucleate centers which are large enough to remain on the electrode surface after switching to the growth potential.

### 5.5.3 1 mM $AgNO_3$ + 5 mM tri-sodium citrate + 0.1 M $NaClO_4$

The initial set of solutions employing tri-sodium citrate as a stabiliser were investigated again with the addition of sodium perchlorate as a base electrolyte in order to determine the influence of uncompensated resistance on the growth parameters. Figure 5.10 (a) shows the corresponding cyclic voltammogram for this system. This is similar to that presented in Section 5.5.1. The stripping peak is observed at a potential of 0.03 V more negative. This is due to the absence of

Table 5.2: Analysis of the current maxima. Data taken from Figure 5.10 (b).

| $-\eta$ (mV) | $-10^4 I_m$ (A cm$^{-2}$) | $t_m$ (s) | $10^7 I_m^2 t_m$ (A$^2$ cm$^{-4}$s) |
|---|---|---|---|
| 105 | 1.05 | 2.81 | 3.08 |
| 110 | 1.38 | 1.71 | 3.26 |
| 115 | 1.82 | 0.95 | 3.13 |
| 120 | 2.35 | 0.60 | 3.32 |
| 125 | 2.97 | 0.39 | 3.45 |
| 130 | 3.66 | 0.28 | 3.75 |
| 135 | 4.56 | 0.20 | 4.05 |
| 140 | 5.43 | 0.16 | 4.56 |
| 145 | 6.49 | 0.11 | 4.63 |

ohmic drop that dominates the stripping peak in the absence of a base electrolyte. The potential of the $Ag/Ag^+$ couple was -36 mV and $D_{Ag^+} = 1.64 \times 10^{-5}$ cm$^2$s$^{-1}$. The results of the potential step experiments are shown in Figure 5.10 (b). The transients observed are typical for 3-D nucleation and growth controlled by hemispherical diffusion and can therefore be analysed using the theory discussed in Section 5.2. The calculated values are given in Table 5.2. Figure 5.11 shows a dimensionless plot of $(I/I_m)^2$ vs $t/t_m$ for an overpotential of 145 mV. As can be seen, this follows very closely the dimensionless plot corresponding to progressive nucleation.

The diffusion coefficient calculated from the Cottrell equation at a high enough overpotential (255 mV) was $D_{Ag^+} = 1.65 \times 10^{-5}$ cm$^2$s$^{-1}$, this is in good agreement with that obtained from cyclic voltammetry. The average value of $I_m^2 t_m$ for all the overpotentials was $(3.7 \pm 0.6) \times 10^{-8}$ A$^2$ cm$^{-4}$s. The expected values for instantaneous and progressive nucleation are $2.51 \times 10^{-8}$ A$^2$ cm$^{-4}$s and $4.00 \times 10^{-8}$ A$^2$ cm$^{-4}$s, respectively, and the results were within experimental error for the value corresponding to progressive nucleation.

Interestingly, simple addition of a base electrolyte $NaClO_4$ to the initial 1 mM $AgNO_3$ + 5 mM tri-sodium citrate system, changed the type of nucleation from

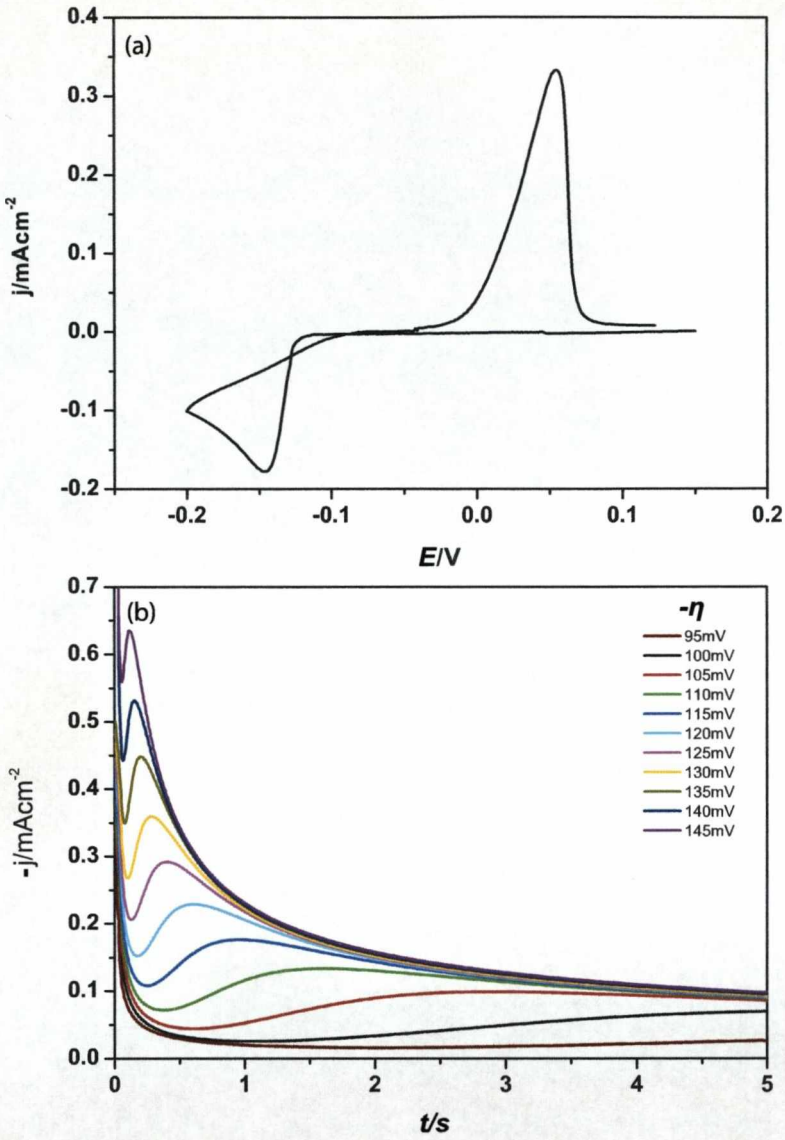


Figure 5.10: (a) CV curve obtained in a Pt/1 mM $AgNO_3$ + 5 mM Tri-sodium Citrate + 0.1 M $NaClO_4$ system. The potential scan started at 0.15 V toward the negative direction and then reversed at -0.2 V at a scan rate of 10 mV/s and (b) A set of experimental current time transients recorded in same system at the different overpotentials indicated in the figure.

instantaneous to progressive. The reason for this behavior is unclear.

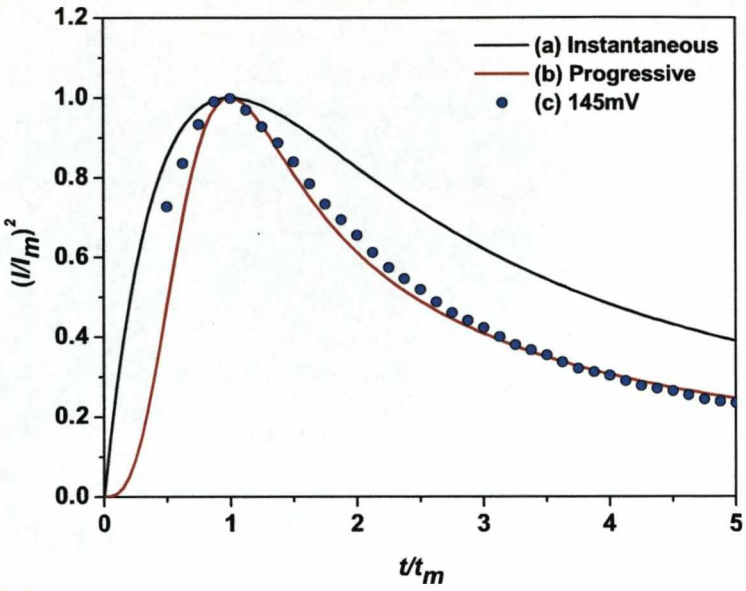


Figure 5.11: Non-dimensional $(I/I_m)^2$ vs $t/t_m$ plots for (a) instantaneous nucleation and (b) progressive nucleation and (c) the data from Figure 5.10 (b) for 145 mV.

### 5.5.4 0.1 M $AgClO_4$

Since dendritic growth was considered interesting for the synthesis of nanorods, $Ag^+$ solutions in the absence of a base electrolyte were studied. Figure 5.12 shows the cyclic voltammogram and the corresponding set of $j - t$ transients for 0.1 M $AgClO_4$. A high concentration was employed to facilitate 1D diffusional growth and also lead to a higher yield of products in solution when ultrasound was used to dislodge the electrodeposited metal centers from the electrode surface.

The cyclic voltammogram observed is typical for a system dominated by ohmic drop. However, the characteristic cross-over loop of a nucleation and growth process can still be observed. The current densities observed in the $j-t$ transients are much smaller than expected for such a highly concentrated solution. Since no

base electrolyte is present, the low current densities observed could be a result of large dentritic growth.

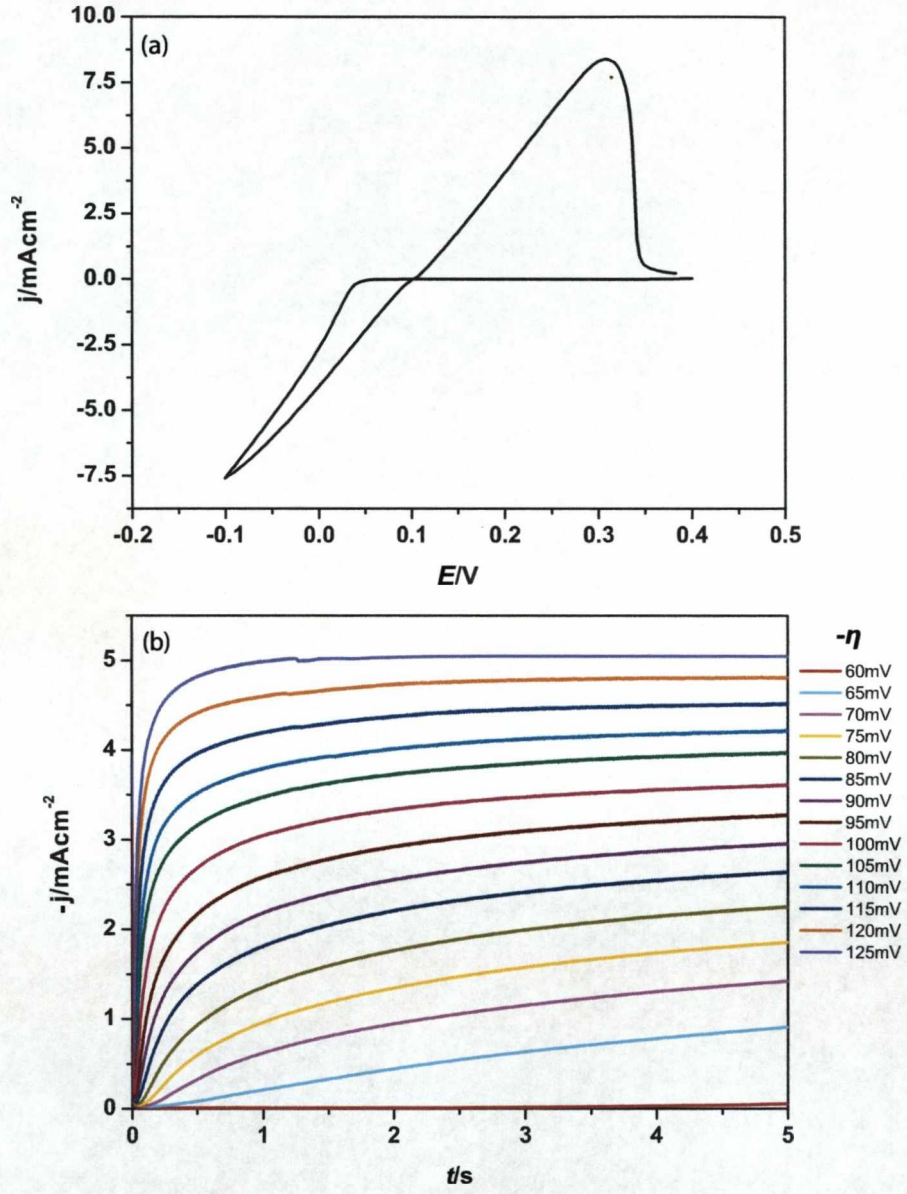


Figure 5.12: (a) CV curve obtained in a Pt/0.1 M $AgClO_4$ system. The potential scan started at 0.4 V toward the negative direction and then reversed at -0.1 V at a scan rate of 50 mV/s and (b) A set of experimental current time transients recorded in a Pt/0.1 M $AgClO_4$ system at the overpotentials indicated in the figure by pulsing from a stripping potential of 0.11 V

If 1-D dendritic growth occurs then the observed current would be expected to be localised at the growing tips of the dendrites and minimal diffusional growth would be taking place at the electrode surface. Furthermore, the current response of the $j - t$ transients should become constant after very short times even at relatively low overpotentials. A schematic diagram showing the difference between 3-D and 1-D diffusional growth is shown in Figure 5.13. For hemispherical diffusional growth, overlap of the depletion zones surrounding each nuclei causes the current to decay as predicted by the Cottrell equation. However, for diffusional growth at the tip of dendrites no overlap of the diffusional fields of the growing deposit would occur and the current response would becomes constant. Thus, spherical diffusion at the tips of dendrites gives a self-preserving diffusional geometry, in contrast with the 3-D growth of nuclei.

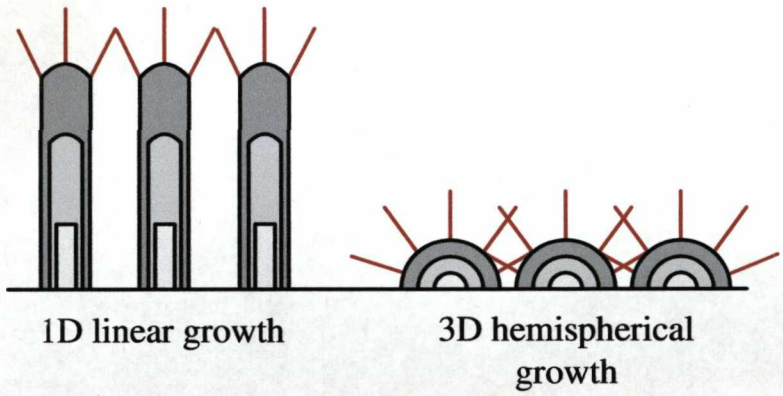


Figure 5.13: A schematic diagram showing the difference between 1-D and 3-D diffusional growth.

Due to the unusual characteristics of the $j - t$ transients, the diagnostic criterion employed in earlier sections could not be used. However, Milchev et al. [177] studied a similar system and found that the data was in good agreement for progressive nucleation. On this basis, the current response from the rising section of the transients displayed in Figure 5.12 (b) should be linear with respect to $t^{3/2}$ and Figure 5.14 shows that this is the case, confirming the presence of progressive

nucleation. The potential of the $Ag/Ag^+$ couple was 79.2 mV which is also in good agreement with the value given by Milchev et al. [177].

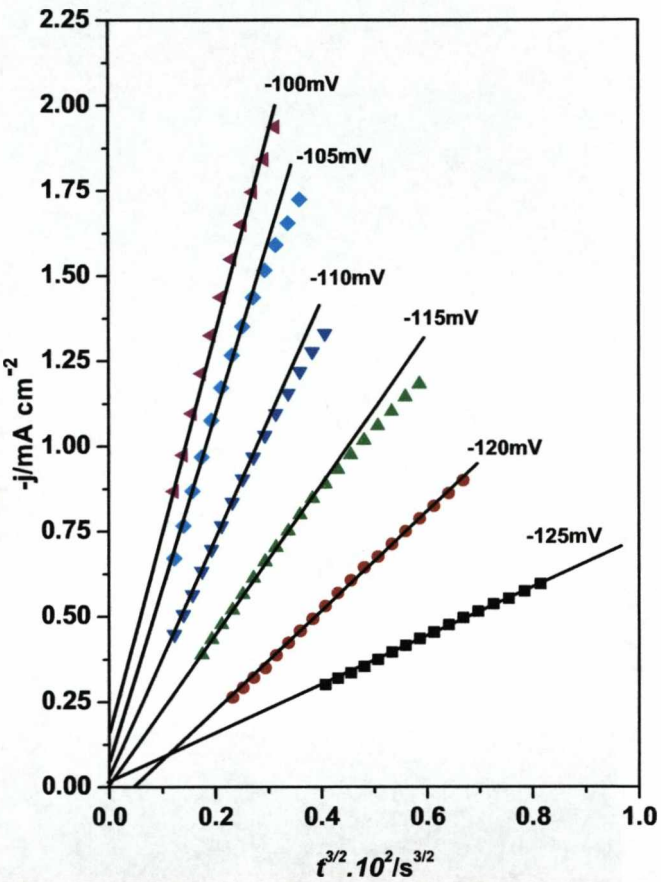


Figure 5.14: Plots of $j$ vs $t^{3/2}$ taken from the middle, rising current sections of the transients in Figure 5.12 (a).

### 5.5.5 5 mM $AgNO_3$ + 0.8 g/l PVP

The use of polyvinylpyrrolidone (PVP) as a stabilising agent for metal nanoparticles is well documented [38, 178–181]. Many shape selective syntheses have been developed to prepare anisotropic metal nanoparticles with a variety of shapes [132, 182] and PVP has been frequently used as the crucial reagent for controlling the shapes by selective absorption on specific metal crystallographic facets [182].

The structure of PVP is shown in Figure 5.15. It consists of a polyvinyl skeleton with polar groups that strongly adsorb on the surface of silver nanoparticles through coordination between silver and the oxygen atoms of the carbonyl groups [114].

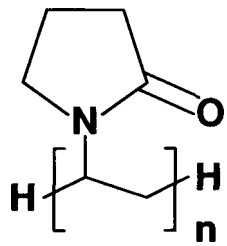


Figure 5.15: The molecular structure of polyvinylpyrrolidone (n denotes the number of repeating units).

Due to its long chain structure, silver dendrites and chain-like structures have been synthesised in which PVP acts as both an adsorption agent and an architectural soft template [183]. An electrochemical investigation of PVP/$AgNO_3$ by Yin et al. [113] showed that PVP greatly promotes silver particle formation rate and significantly reduces silver deposition rate thereby making monodisperse silver nanoparticle formation viable through electroreduction. Jiang et al. [114] took this a stage further and presented a novel route for the preparation of monodisperse silver nanoparticles in the presence of PVP by a pulse sonoelectrochemical technique. In this study, a concentration of 0.8 g/l of PVP ($M_W$=55,000) was employed.

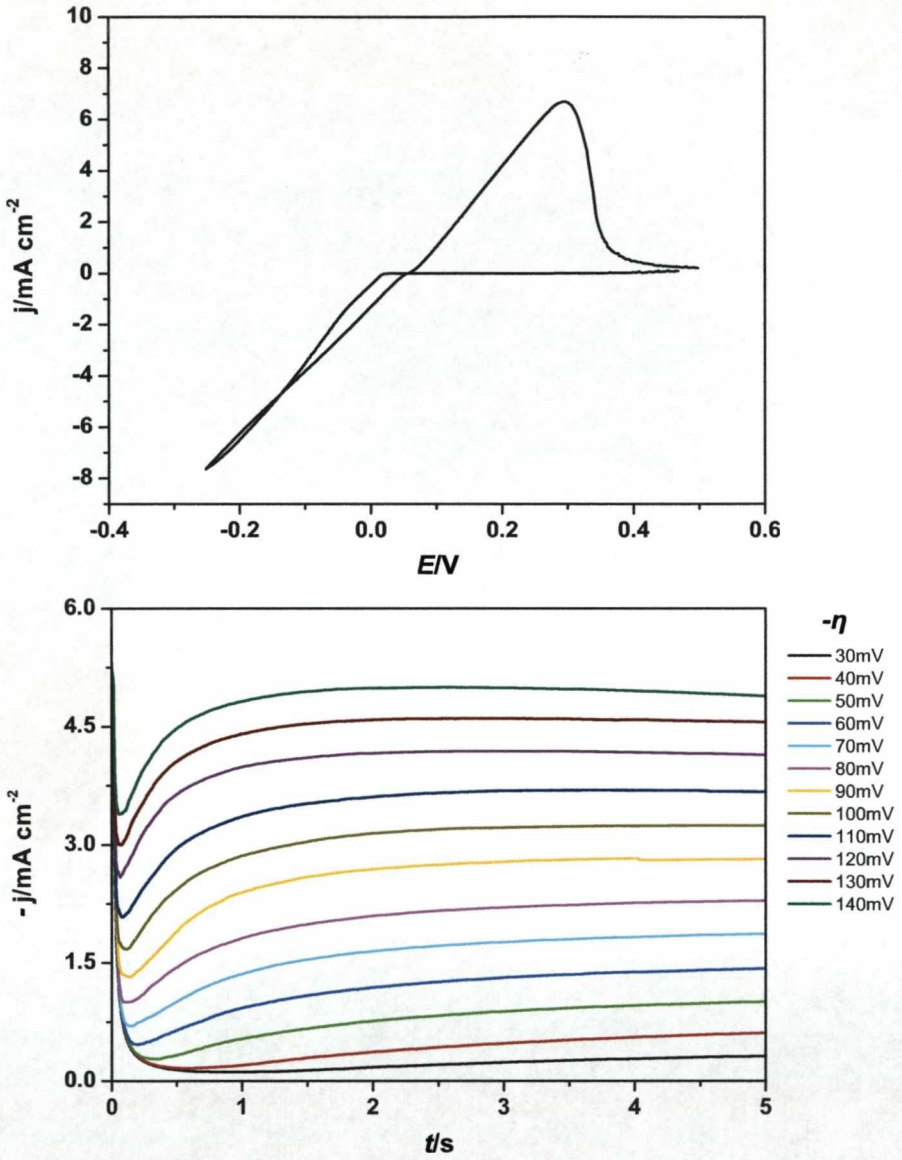


Figure 5.16: (a) CV curve obtained in a Pt/5 mM $AgNO_3$ + 0.8 g/l PVP. The potential scan started at 0.5 V toward the negative direction and then reversed at -0.25 V at a scan rate of 20 mV/s and (b) A set of experimental current time transients recorded in a Pt/5 mM $AgNO_3$ + 0.8 g/l PVP system at the overpotentials indicated in the Figure.

The corresponding cyclic voltammogram and $j-t$ transients for 5 mM $AgNO_3$ + 0.8 g/l PVP are shown in Figure 5.16. Compared with the results in Figure 5.8 for a similar concentration, a larger current density is observed in the presence of

PVP. For similar overpotentials (140 mV), a current density of 1.25 mA $cm^{-2}$ was observed for the citrate solution, but this increased to 4.75 mA $cm^{-2}$ when PVP was employed as the stabilising agent. Furthermore, the cyclic voltammogram shows the characteristics of a system dominated by ohmic drop. The experimental cell arrangement employed was the same as in all previous experiments. The $j-t$ transients also resemble those of a more concentrated solution as the currents observed in the decaying section of each transient do not follow the predictions from the Cottrell equation and instead, an almost constant current is observed. At higher overpotentials, the onset of a slight decay is observed but even at much longer times (360 seconds) this decay did not follow the Cottrell equation. Due to the shape directing properties of PVP, this constant limiting current could be due to 1-D linear diffusional growth of silver at the electrode surface as discussed in Section 5.5.4.

Double potential step experiments were employed to investigate further the nucleation and growth processes observed by altering the parameters $E_2$ and $t_1$. The results of this are shown in Figure 5.17 along with the potentials and times employed.

Figures 5.17 (a)-(b) shows the effect of increasing the growth overpotential, $E_2$, but keeping all other parameters constant. As the overpotential is increased to more negative values it is clear that not all the available sites are covered by nuclei and hence, nucleation is continuing at the growth potential. Figures 5.17 (c)-(d) show the effect of increasing the nucleation time of the growth of nuclei. It is clear that increasing the nucleation time significantly effects the current observed associated with the growing nuclei and it is apparent that 1-D growth is observed as longer nucleation times are employed. Therefore, it can be concluded that for the proposed synthetic strategy to be followed, longer nucleation times are preferred.

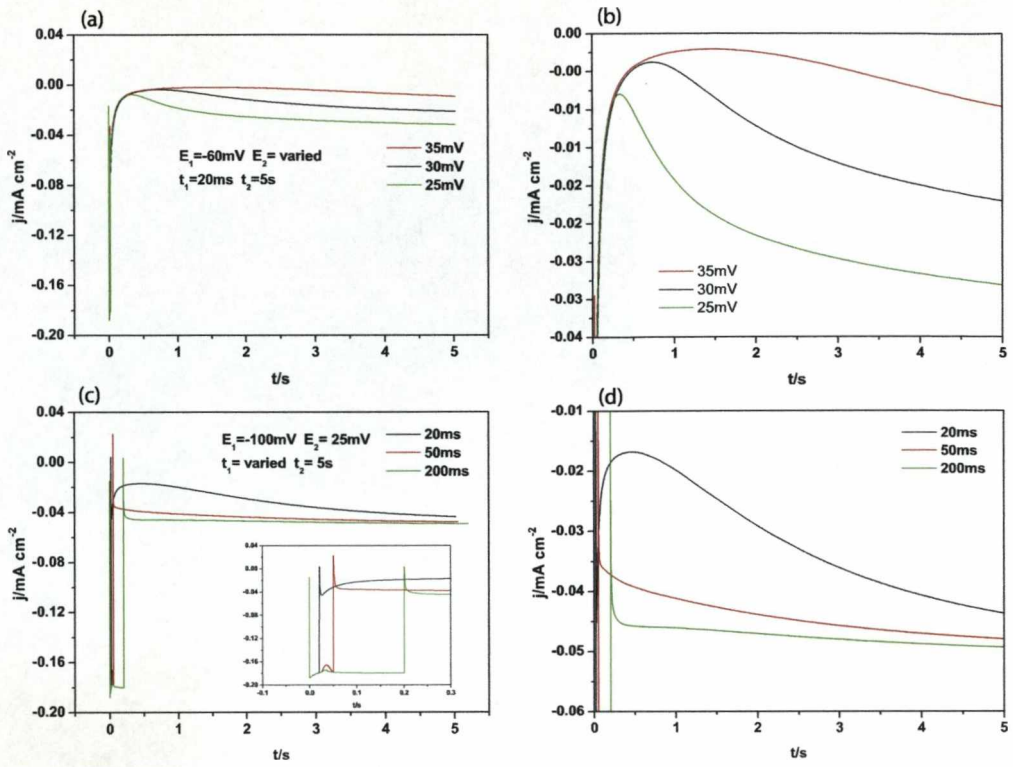


Figure 5.17: Current response to the change in the parameters (a) $E_2$, (c) and (e) $t_1$ for the system Pt/5 mM $AgNO_3$ + 0.8 g/l PVP. The insets on a $j$(t) transient show the current response at shorter times. Figures (b), (d) and (f) show the current responses of (a), (c) and (e), respectively, in more detail.

### 5.5.6 5 mM $AgClO_4$ + 20 mM $HClO_4$

As a comparison with previous experiments carried out in the absence of supporting electrolyte, perchloric acid was employed as a base electrolyte to investigate its effect on the kinetics of nucleation. The corresponding cyclic voltammogram and $j - t$ transients are shown in Figure 5.18. The CV shows the expected characteristics of a nucleation and growth metal deposition reaction. The potential of the $Ag/Ag^+$ couple was 52.5 mV. Similarly to the results shown in Figure 5.16 the $j - t$ transients in Figure 5.18 (b) show an increase in current density as the overpotential is increased; the rate at which the maximum current is reached is far greater than in previous experiments, with all current maxima occurring within 1

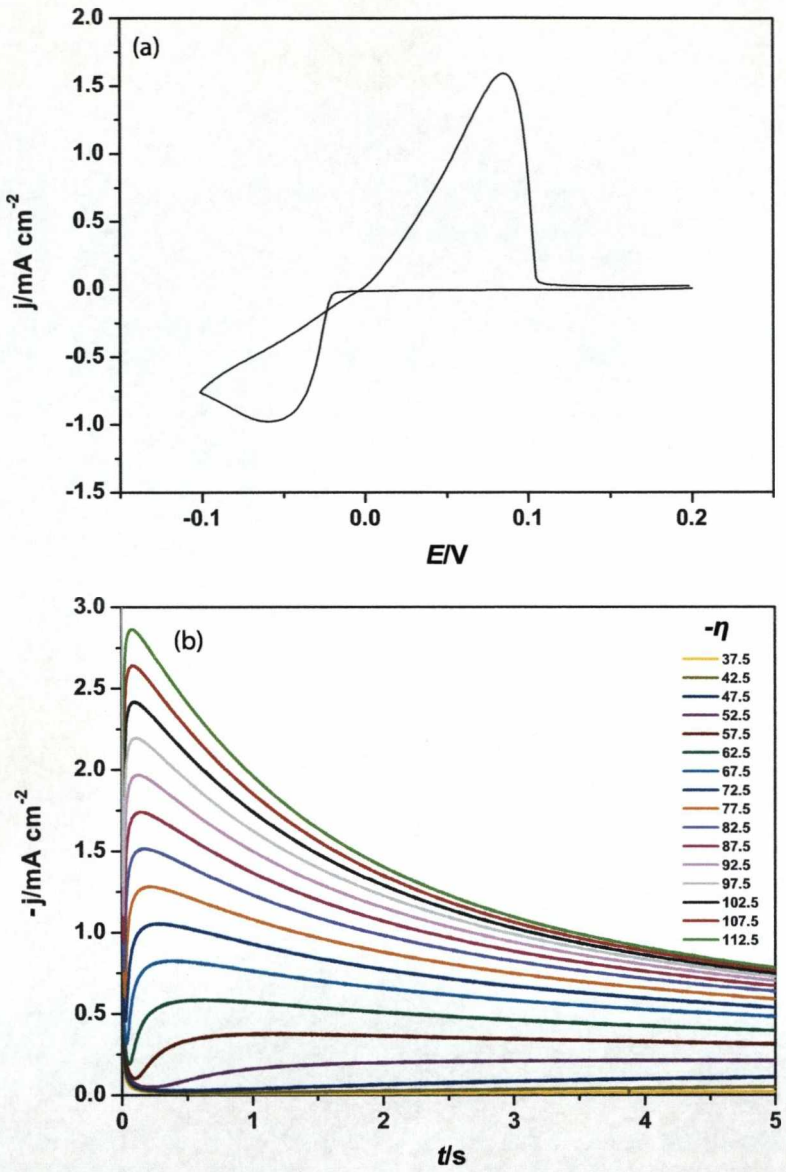


Figure 5.18: (a) CV curve obtained in a Pt/5 mM $AgClO_4$ + 20 mM $HClO_4$. The potential scan started at 0.2 V toward the negative direction and then reversed at -0.1 V at a scan rate of 20 mV/s and (b) A set of experimental current time transients recorded in a Pt/5 mM $AgClO_4$ + 20 mM $HClO_4$ at the overpotentials indicated in the Figure.

second. This indicates that the rate of nucleation is much faster with the addition of an acid as a base electrolyte.

By employing classical theory, the kinetics of nucleation was investigated and the corresponding nuclear number densities, as a function of overpotential, were calculated as shown in Table 5.3. From the results, $D_{Ag^+} = 1.42\times10^{-5}$ $cm^2s^{-1}$ (Equation 5.24). From this value the corresponding values of $5.39\times10^{-7}$ $A^2$ $cm^{-4}s$ and $8.59\times10^{-7}$ $A^2$ $cm^{-4}s$ were calculated for $I_m^2 t_m$, for instantaneous and progressive nucleation, respectively. The mean value of $I_m^2 t_m$, obtained experimentally $4.33\times10^{-7}$ $A^2$ $cm^{-4}s$ which indicates that instantaneous nucleation is occurring.

This is further confirmed in dimensionless plots shown in Figure 5.19. These show that initially, nucleation is instantaneous and is independent of the applied overpotential. At longer times, however, there is a large deviation from the values predicted from Equations 5.22 and 5.23.

Table 5.3: Analysis of the current maxima. Data taken from Figure 5.18 (b).

| $-\eta$ (mV) | $-10^3 I_m$ ($Acm^{-2}$) | $t_m$ (s) | $10^7 I_m^2 t_m$ ($A^2cm^{-4}s$) | $10^6 N$ ($cm^{-2}$) |
|---|---|---|---|---|
| 62.5 | 0.58 | 0.49 | 1.66 | 1.97 |
| 67.5 | 0.83 | 0.37 | 2.56 | 2.62 |
| 72.5 | 1.05 | 0.28 | 3.12 | 3.44 |
| 77.5 | 1.28 | 0.22 | 3.62 | 4.41 |
| 82.5 | 1.51 | 0.18 | 4.08 | 5.44 |
| 87.5 | 1.75 | 0.15 | 4.62 | 6.45 |
| 92.5 | 1.96 | 0.12 | 4.61 | 8.11 |
| 97.5 | 2.20 | 0.11 | 5.32 | 8.85 |
| 102.5 | 2.41 | 0.09 | 5.51 | 10.3 |
| 107.5 | 2.67 | 0.08 | 6.03 | 11.5 |
| 112.5 | 2.85 | 0.07 | 6.52 | 12.1 |

These classical nucleation and growth relationships refer to well defined conditions of spherical diffusion but cannot reproduce more complex behaviour as is obviously the case with these experiments. It is interesting to notice, however, that the system follows an instantaneous nucleation model for $t/t_m \leq 1.8$ s. This indicates that the diffusion geometry is initially hemispherical but changes to a more complex pattern, including a 1-D component, at longer times. This result most likely reflects the changes in geometry of the growing crystallites with

electrolysis time.

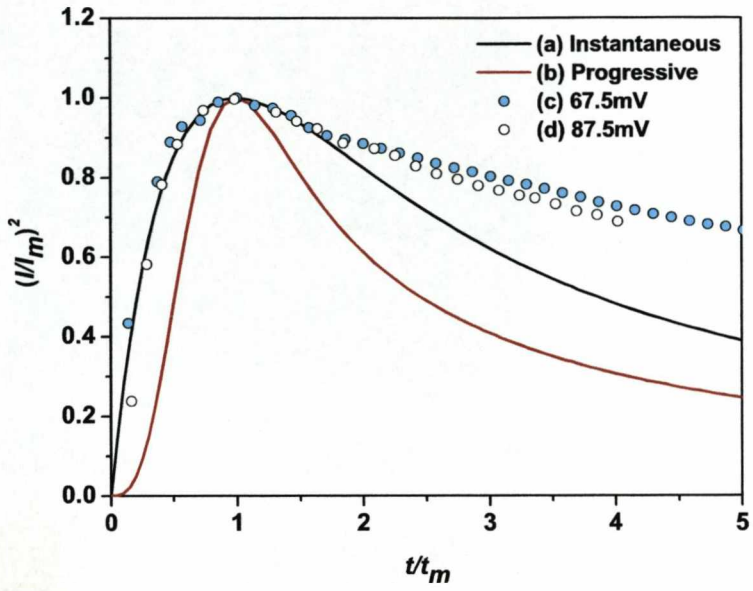


Figure 5.19: Non-dimensional $(I/I_m)^2$ vs $t/t_m$ plots for (a) instantaneous nucleation and (b) progressive nucleation and (c) the data from Figure 5.18 (b) for overpotentials of 67.5 mV and 87.5 mV

### 5.5.7 0.1 M $AgClO_4$ + 20 mM $HClO_4$

In order to increase the current density and hence, the yield of nanoparticles achievable, the use of a higher concentration of silver perchlorate was investigated. Figure 5.20 shows the corresponding cyclic voltammogram and current-time transients. The potential of the $Ag/Ag^+$ couple was measured at 75.2 mV.

The results are similar to those measured for 0.1 M $AgClO_4$. In both cases a constant current is observed with and without the addition of base electrolyte, indicative of 1-D diffusion limited growth, but the time at which this is reached is considerably faster with the addition of the base electrolyte.

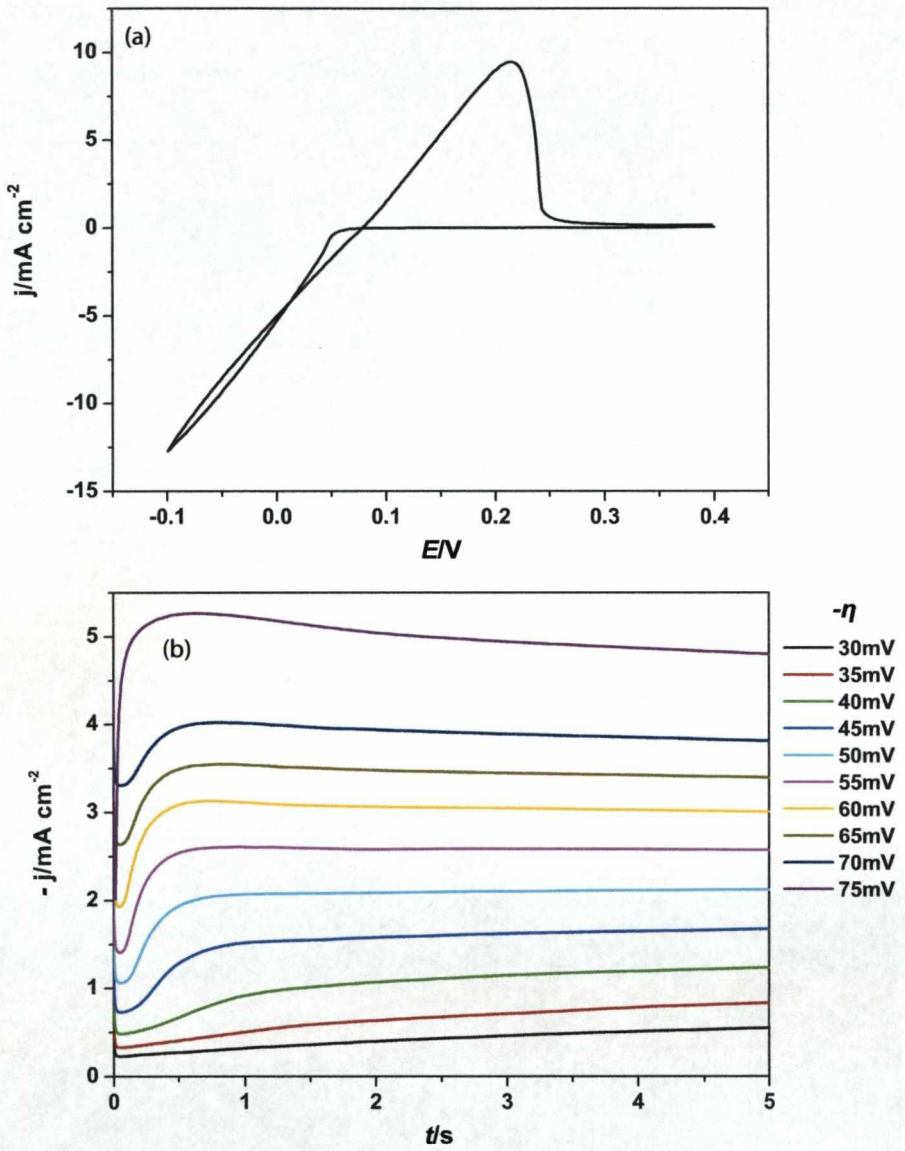


Figure 5.20: (a) Typical CV curve obtained in a Pt/0.1 M $AgClO_4$ + 20 mM $HClO_4$. The potential scan started at 0.4 V toward the negative direction and then reversed at -0.1 V at a scan rate of 20 mV/s and (b) A set of experimental current time transients recorded in a Pt/0.1 M $AgClO_4$ + 20 mM $HClO_4$ system at the overpotentials indicated in the Figure.

## 5.6 Summary

Several $Ag^+$ systems have been investigated using cyclic voltammetry and a single/double potential step to assertain the optimum conditions for the electrochemical growth of nanoparticles at an electrode surface. The effects of the addition of two stabilising agents, tri-sodium citrate and PVP, the use of different base electrolytes and the effects of supporting ions were investigated as well as the influence of solution concentration. The kinetics of nucleation and growth were also investigated, where allowed, by the use of current-time transients to determine the type of nucleation occurring.

It was observed that altering the experimental conditions had a dramatic effect on the kinetics and the type of nucleation occurring. For both dilute solutions of 1 mM and 5 mM $AgNO_3$ + 5 mM tri-sodium citrate, instantaneous nucleation was observed. However, by the simple addition of a base electrolyte, $NaClO_4$, the type of nucleation occurring changed to progressive. The only noticeable effect of the citrate ions in solution was to decrease the diffusion coefficient of $Ag^+$; possibly due to its coordination by citrate.

With the addition of PVP, a noticeable increase in the current density was observed for both the CV and the $j - t$ transients. This was coupled with a proposed one dimensional growth by the appearance of a constant current in the growth region of the transient.

For 0.1 M $AgClO_4$, investigation of the rising sections of the transients showed that progressive nucleation was occurring since the current was linearly dependent on $t^{3/2}$.

In order to use ultrasound to dislodge the nuclei forming and produce monodisperse nanoparticles, instantaneous nucleation is required since at any given time, the nuclear number density will be constant. Therefore, on the basis of these results it was concluded that initially no stabilising agent would be employed until it had been proved experimentally that it was possible to transfer the deposited

nanoparticles into solution. However, once transfer had been achieved then PVP would be employed as the stabilising agent due to the proposed one dimensional growth observed in Section 5.5.5. Also it was initially proposed that in order for dendritic 1-D growth to occur a highly concentrated solution without a base electrolyte would be favourable. However, the rate at which nucleation occurred was slow. This was overcome by the addition of a base electrolyte that increased the rate of nucleation observed. On these factors both 0.1 M and 5 mM $AgClO_4$ and 20 mM $HClO_4$ were chosen as the medium for the ultrasonic electrochemical synthesis. This work is detailed in the next Chapter.

# Chapter 6

# Sonoelectrochemical Synthesis of Silver Nanoparticles

## 6.1 Introduction

The combination of electrochemistry and ultrasound has been shown to have a large influence on the electrodeposition of metals [107]. On the basis of the results from Chapter 5 it was investigated whether metallic centres nucleated and grown at an electrode surface could be dislodged using ultrasound in order to synthesise metal nanoparticles. The main advantages of this method is that not only does the burst of ultrasonic energy remove the metal particles from the cathode, but this also leads to the cleaning of the electrode surface and provides a very high rate of mass transport by the localised turbulence in the solution. Similar systems have been investigated previously with the aim of producing pure binary and ternary alloyed metal nanopowders [25], semiconductors [108], silver nanowires [111] and amorphous silver nanoparticles [184].

The main difference between this previous work and that carried out here is that the products are formed by employing a constant potential controlled regime. This limits the control over the size and shape of the products formed.

By coupling a double potential step profile with pulsed ultrasonic excitation it was hoped that greater control could be achieved on the growth and size distribution of the nanoparticles synthesised.

## 6.2 Chemicals and Materials

Silver perchlorate monohyrdate ($AgClO_4 \cdot H_2O$, 99.999%), perchloric acid ($HClO_4$, 70% A.C.S), polyvinylpyrrolidone (PVP10; average $M_w$=10,000 and PVP55; average $M_w$=55,000), hydrogen tetrachloroaurate ($HAuCl_4.3H_2O$, 99.99%), potassium hydroxide (KOH, 85%) and sulphuric acid ($H_2SO_4$, 98.0% A.C.S) were purchased from Aldrich. All glassware was cleaned prior to use using freshly prepared aqua regia (1:3 $HNO_3$:HCl) followed by repeated rinsing with ultra pure Milli-Q water.

## 6.3 Experimental

The potential pulse profile employed was the same as for the double potential step experiments, where the nucleation and growth potentials, along with their time can all be independently altered and controlled. Experimental details of this are given in Section 2.2.2.

During the period when no nucleation or growth occurs, the electrode was held at a constant stripping potential of +0.3V to clean the surface from material electrodeposited during previous growth cycles. The pulse profile was repeated every second for a total of 1 hour. The ultrasonic horn was placed at a constant distance of 2 mm from the working electrode and the intensity of the ultrasonic pulse was set to 95% of full power. The timing of the ultrasonic pulse used to dislodge the nanoparticles was controlled using a Hi-Tek PPR1 signal generator and an oscilloscope was employed as a visual aid to fine-tune accurately the pulse time sequence. The current response produced during the nucleation, growth

and the eventual removal of the metal nanoparticles was recorded on a separate oscilloscope. The ultrasonic pulse was positioned so that it overlapped with the switching to the stripping potential to ensure that no further growth could occur after the ultrasonic pulse had ended. The ultrasonic pulse was set to last 50ms.

All conditions and hardware were the same as employed in the orientation experiments. The pulse parameters and nomenclature is the same as described in the previous Chapter. All measurements were performed in the three-electrode cell described in Section 2.5.3. Each solution investigated was purged with oxygen free argon for 30 minutes prior to any measurements being taken. Two different working electrodes were employed as described below.

## 6.4 Platinum Electrode

### 6.4.1 0.1 M $AgClO_4$ + 20 mM $HClO_4$

In the first experiments, a high concentration of analyte was employed to increase both the likelihood of dendritic/rod-like growth and the overall yield of the nanoparticles produced. From the results obtained from the CV and $j - t$ transients shown in Chapter 5, Section 5.5.2, the following nucleation and growth parameters were chosen: $E_1$ = -0.1 V, $t_1$ = 5 ms, $E_2$ = +0.05 V and $t_2$ = 400 ms. After 10 minutes of ultrasonic coupled electrodeposition the colour of the solution inside the cell changed from clear to light yellow. This colour is characteristic of a solution containing silver nanoparticles.

Figure 6.1 shows the UV-Vis spectrum of the as-produced solution taken after 30 minutes of electrolysis. The absorption peak centered at 408nm is characteristic of the surface plasmon resonance of silver nanoparticles [185]. The broad peak observed indicates a wide dispersion of shapes and sizes in solution. Due to the high electrolyte concentration and the absence of any stabilising agent, the silver nanoparticles were unstable and precipitated from solution after a short time.

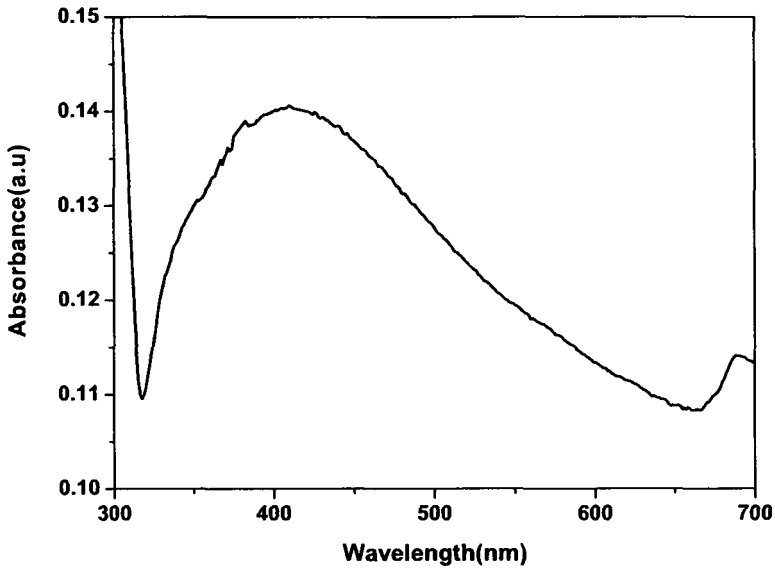


Figure 6.1: UV-Vis spectra of the as-prepared silver nanoparticles formed by repeated nucleation, growth and ultrasonic dislodgement from a 0.1 M $AgClO_4$ + 20 mM $HClO_4$ solution under the following conditions: $E_1$ = -0.1 V, $t_1$ = 5 ms, $E_2$ = +0.05 V and $t_2$ = 400 ms.

Because of this it was not possible to take representative TEM images.

### 6.4.2 5 mM $AgClO_4$ + 20 mM $HClO_4$

From the results obtained in Section 6.4.1 and the relative success of this sonoelectrochemical technique to produce nanoparticles, a lower electrolyte concentration was employed in an attempt to increase the stability of the silver nanoparticles produced.

The same potentials and times as for the 0.1 M $AgClO_4$ + 20 mM $HClO_4$ solution were employed but even after 1 hour of electrolysis the UV-Vis spectra showed that no silver nanoparticles were formed. The lack of results shows that the solution concentration greatly affects the results obtained. From the work reported in the previous Chapter, nucleation and growth should occur at the

potentials employed but various attempts using different nucleation and pulse potentials failed to produce any nanoparticles in solution. It is possible that the size of the nuclei produced at these potentials was too small to allow transfer into solution and redissolved due to the absence of any stabilising agent . Another possibility is that the growth period was insufficient to allow the nuclei to grow to a large enough size. Due to limitations beyond control in the experimental setup, the entire pulse cycle had to be limited to less than one second in order for a sufficiently large number of repetition cycles to be achieved.

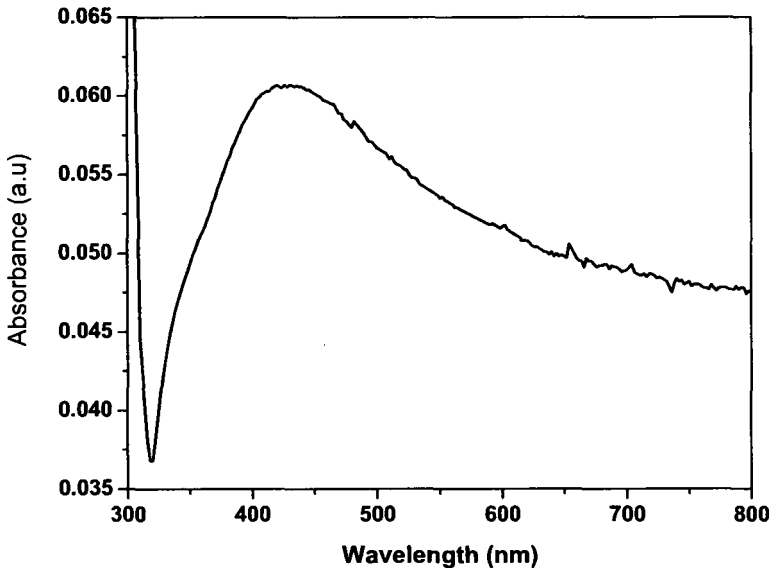


Figure 6.2: UV-Vis spectra of silver nanoparticles formed by repeated nucleation, growth and ultrasonic dislodgement from a 5 mM $AgClO_4$ + 20 mM $HClO_4$ solution from a single growth potential of -0.5 V for 400 ms.

It is known that the potentials and times employed in the double pulse experiments have a great influence on the size of the nucleated centres produced [168, 169]. During the transition in potential from the high nucleation overpotential to the moderate growth overpotential, all nuclei that had not yet reached the critical

size needed to continue to grow simply redissolve. If this is the case, then by eliminating this transition and applying a constant potential should result in no dissolution and therefore, increase the number of nuclei on the electrode surface. For this reason, a constant potential of -0.5 V was employed for 400 ms.

Figure 6.2 shows the UV-Vis spectra of the solution obtained after electrolysis for 30 minutes at a single potential of -0.5 V held for 400 ms followed by dislodgement by ultrasound. A stripping potential of +0.3 V was applied after the pulse profile to ensure the absence of metal nuclei when starting the next deposition cycle. A surface plasmon resonance peak at ~428 nm was present indicating the formation of silver nanoparticles in solution. This was confirmed by a change in the colour of the solution from clear to a light yellow after 30 minutes.

From the results of Zhang and co-workers, the scattering of light by nuclei with a diameter less than 10 nm is responsible for the light yellow colour [186]. The broad plasmon band absorbance is comparable to that of the nanoparticles formed in the 0.1 M $AgClO_4$ + 20 mM $HClO_4$ solution. A shift in the peak maxima from 408 nm to 428 nm was observed. The position of the plasmon resonance band is known to be highly dependent on size and shape [16, 23, 187]. It can be concluded that, by employing a single nucleation/growth pulse, larger nanoparticles are produced.

Figure 6.3 shows the UV-Vis spectra taken at different electrolysis times during the silver nanoparticles synthesis. A linear relationship between the absorbance and the electrolysis time is observed as shown in Figure 6.4, which indicates that formation of the silver nanoparticles is not hindered by longer reaction times. Furthermore, each UV-Vis spectra is similar for different times of electrolysis indicating that the morphology of the nanoparticles produced is constant. No separate longitudinal plasmon band is observed. There is, however, a shift in the maximum peak of the plasmon resonance band. As time progresses from 30 minutes to 60 minutes, a shift from 428 nm to 447 nm is observed. This indicates

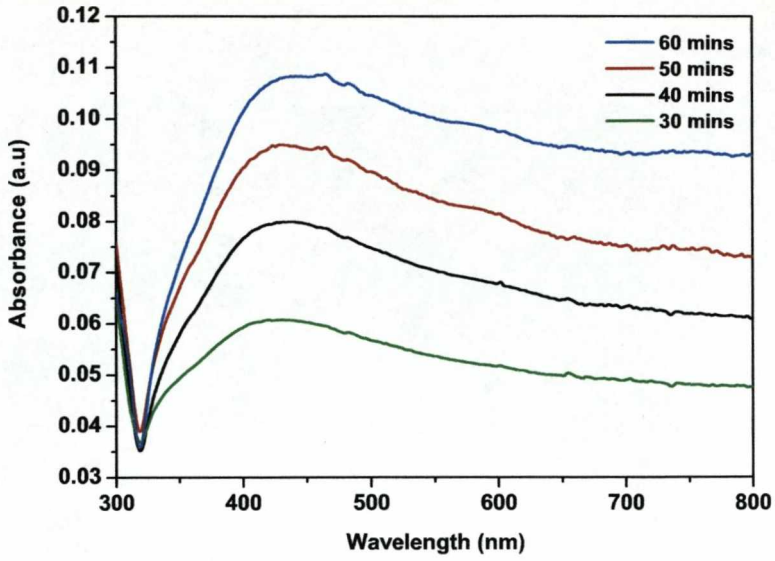


Figure 6.3: UV-Vis spectra of the as-prepared silver nanoparticles formed by repeated nucleation, growth and ultrasonic dislodgement from a 5 mM $AgClO_4$ + 20 mM $HClO_4$ solution from a single growth potential of -0.5 V for 400 ms taken at different times during electrolysis under pulsed conditions.

an increase in the size of the nanoparticles produced. This is probably due to slight aggregation of particles already in solution due to the lack of a stabilising agent. The broad band observed indicates the formation of a variety of shapes.

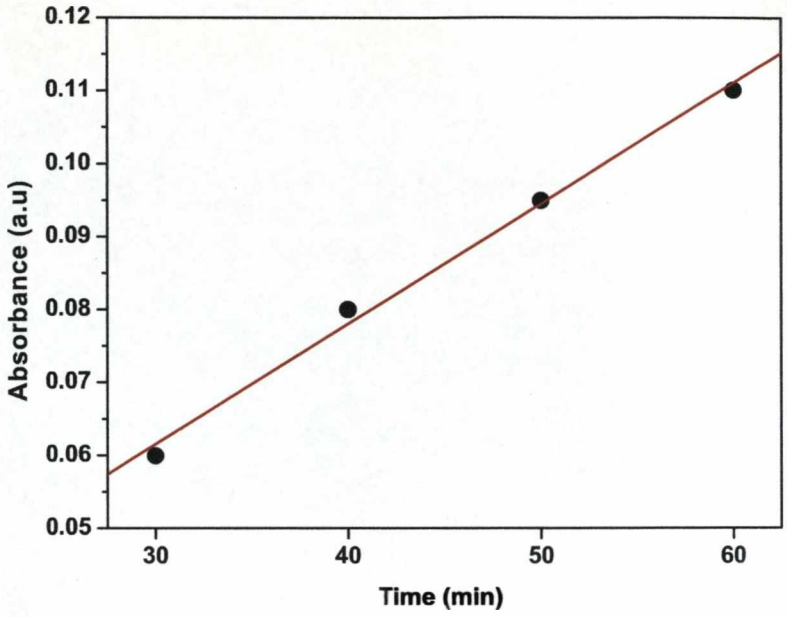


Figure 6.4: Linear dependence of absorbance on pulsed electrolysis time for the formation of silver nanoparticles in a solution of 5 mM $AgClO_4$ + 20 mM $HClO_4$. Conditions as in Figure 6.3

### 6.4.3 2 mM $HAuCl_4$ + 20 mM $H_2SO_4$

Since the stability of gold nanoparticles and nanorods is better than those of silver, the sonoelectrochemical technique was extended to this metal. In addition, gold nanorods are finding applications in medicinal chemistry and a new way of producing this material would be very important. Thus, the nucleation and growth of gold nuclei on a platinum surface was studied to investigate whether the same approach employed for silver could be used to produce gold nanoparticles. Figure 6.5 shows a linear sweep voltammogram for a platinum electrode in a 2 mM $HAuCl_4$ and 20 mM $H_2SO_4$ solution, starting from a potential of 0.8 V. The equilibrium redox potential for $Au/Au^{III}$ in the solution was 0.57 V which is in good agreement with the value reported by Huang et al. [188].

The deposition of gold starts at a potential of ~0.5 V and occurs in two steps. The Au ion has a valence state of 3 and therefore, the reduction of both $Au^{III}$ to

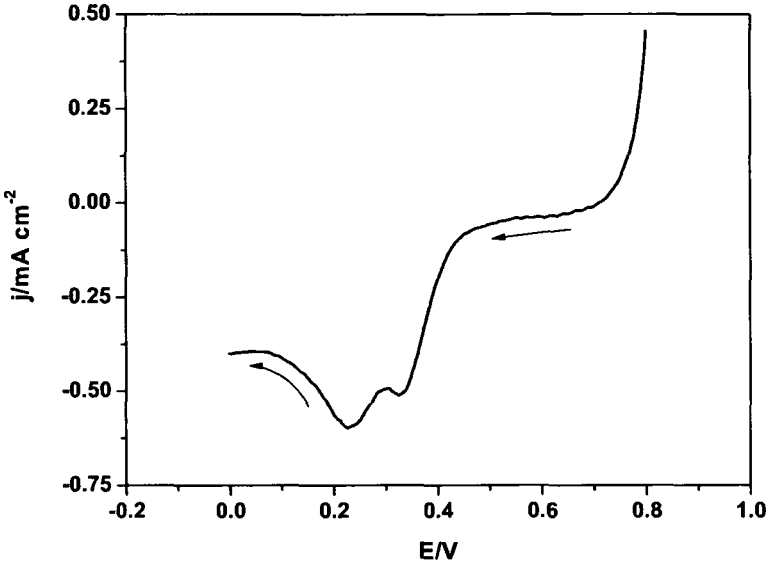


Figure 6.5: Linear sweep voltammogram of the redox reactions of $Au^{III}$ at a Pt electrode in 2 mM $HAuCl_4$ and 20 mM $H_2SO_4$. $\nu = 50$ mV/s

$Au^{I}$ and $Au^{III}$ to $Au^{0}$ is observed. The standard reduction potentials for $AuCl_4^- + 2e^- \longrightarrow AuCl_2^- + 2Cl^-$ and $AuCl_4^- + 3e^- \longrightarrow Au + 4Cl^-$ are 0.93 V and 1.02 V, respectively [188]. The closeness of these values means that electrodeposition appears as a single broad reduction wave. The results shown in Figure 6.5 indicate that they appear resolved into two peaks, although at slightly lower potentials than expected, in good agreement with those reported by Desic et al. [189] for a similar system.

From the cyclic voltammogram in Figure 6.5 it is clear that slow electrodeposition occurs in acid medium and that no nucleation phenomena is observed. The reason for this is not fully understood. This is further observed from a comparison of the cyclic voltammogram recorded before, Figure 6.6 (a), and after, Figure 6.6(b), attempted ultrasonic dislodgement by pulsing to a potential of +0.2 V for 400 ms. Figure 6.6(a) exhibits the characteristic voltammogram for

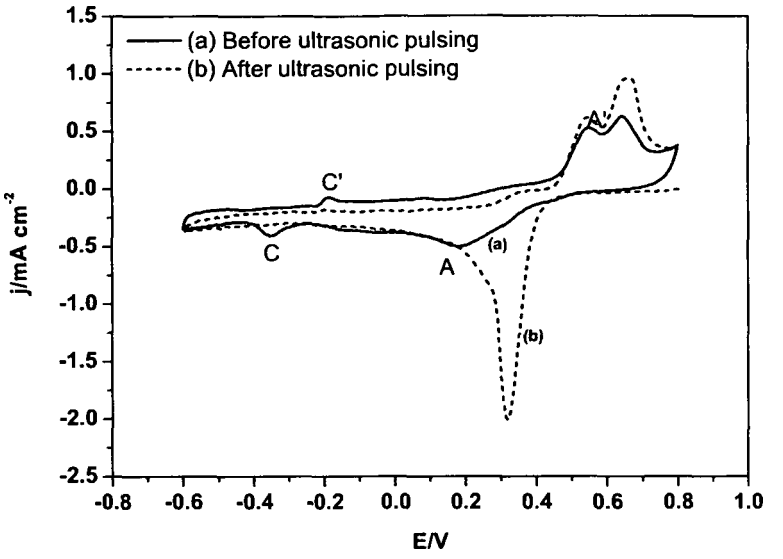


Figure 6.6: Cyclic voltammograms for the redox reactions of $Au^{III}$ at a Pt electrode in 2 mM $HAuCl_4$ and 20 mM $H_2SO_4$ recorded before (a) and (b) after attempted ultrasonic dislodgement. $\nu$ = 50 mV/s.

gold deposition. Peak A is the simultaneous reduction of $Au^{III}$ to $Au^{I}$ and of $Au^{I}$ to $Au^{0}$, and peak A' is the quasi-reversible oxidation peak corresponding to the reduction peak A. As the scan progresses in the cathodic sweep the hydrogen evolution peak, C, is observed at -0.35 V; conversely, peak C' is caused by the desorption of hydrogen from the platinum surface [188]. The large peak present at +0.3 V after attempted ultrasonic dislodgement corresponds to Au oxide reduction indicating gold deposition on the Pt electrode and that the deposit is not removed by the ultrasonic pulse. Furthermore, UV-Vis spectra of the solution taken after 1 hour of pulsing showed no absorbance at ~520 nm where the plasmon band for gold nanoparticles is usually observed. It can be concluded that Au deposition is very uniform.

### 6.4.4 2 mM $HAuCl_4$ + 20 mM KOH

To determine whether nucleation and growth of gold can occur in an alkaline medium the electrodeposition of gold in KOH was investigated, Figure 6.7 shows the corresponding cyclic voltammogram. In comparison to the cyclic voltammogram in acidic medium the current response at the onset of gold deposition is much sharper indicating the presence of a nucleation process. The nucleation of gold centres starts at -0.2 V and this potential was taken as the critical nucleation potential, $E_{CRIT}$. As the scan continued in the cathodic sweep, two peaks appeared at -0.40 V and -0.47 V and on the reverse anodic sweep a small peak was observed at -0.41 V. These are possibly due to secondary nucleation.

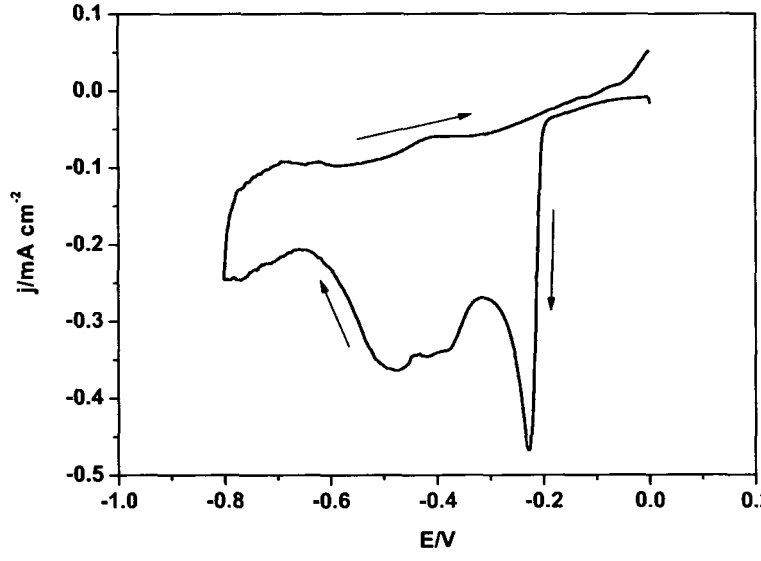


Figure 6.7: Cyclic voltammogram for the electrodeposition of gold at a Pt electrode in 2 mM $HAuCl_4$ and 20 mM KOH. $\nu$ = 50 mV/s.

The kinetics of nucleation was investigated by means of single potential step chronoamperometry. From a rest potential of 0 mV, where no nucleation takes place, the potential was stepped to increasingly cathodic potentials where nucle-

ation and growth is expected. Figure 6.8 shows the corresponding $j-t$ transients for increasing potentials.

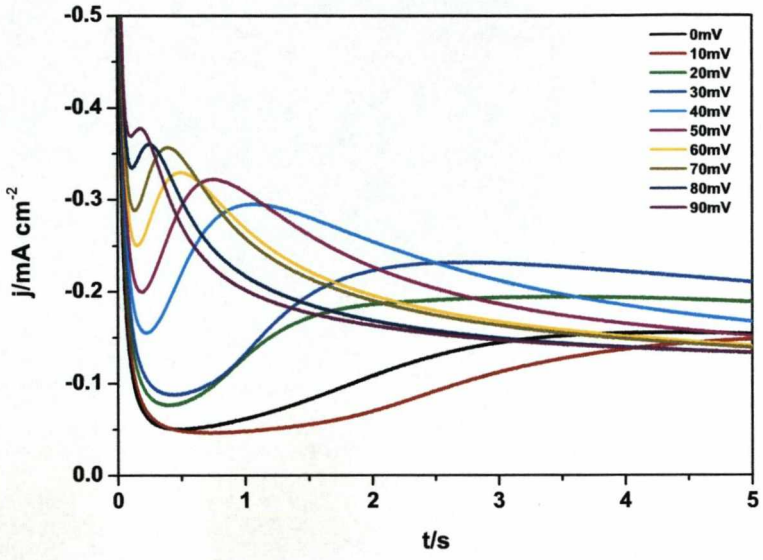


Figure 6.8: Current-time transients for gold electrodeposition on Pt from 2 mM $HAuCl_4$ and 20 mM KOH at the different potentials indicated in the Figure.

The corresponding diffusion coefficient calculated from these $j-t$ transients measured at a very high potential was $1.31\times10^{-6}$ cm$^2$s$^{-1}$. The transients observed are typical of 3D nucleation controlled by hemispherical diffusion and therefore, these can be investigated using the theory set out in Chapter 5, Section 5.2. The parameters calculated from these experiments are shown in Table 6.1.

From Equations 5.18 and 5.21 the term $I_m^2 t_m$ should have values of $7.98\times10^{-9}$ A$^2$ cm$^{-4}$s and $1.27\times10^{-8}$ A$^2$cm$^{-4}$s for instantaneous and progressive nucleation, respectively. The mean value obtained, $(5.4\pm2.5)\times10^{-8}$ A$^2$ cm$^{-4}$s, is closer to that for progressive nucleation, although there is a considerable discrepancy between theory and experiment.

Reduced variable plots were also employed to investigate the type of nucleation

occurring at different potentials and these results are shown in Figure 6.9. Good agreement for progressive nucleation is observed for the three potentials analysed, although the agreement is better at higher potentials.

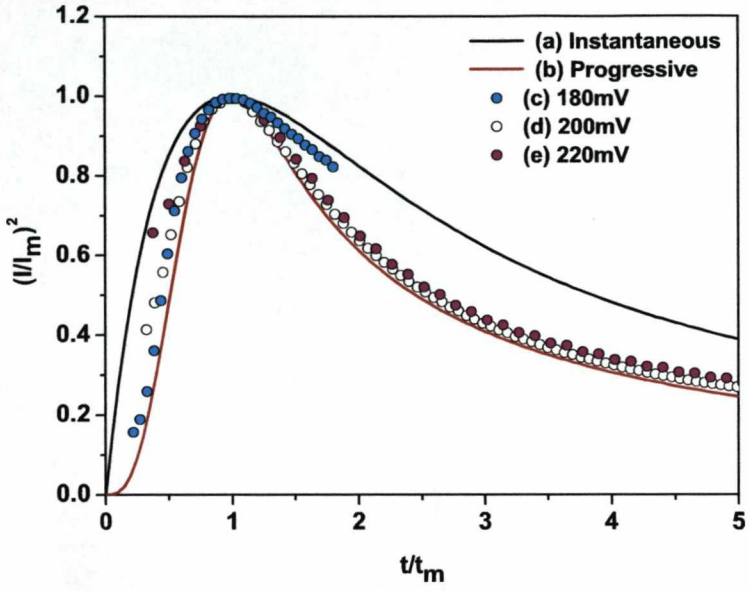


Figure 6.9: Non-dimensional $(I/I_m)^2$ vs $t/t_m$ plots for (a) instantaneous nucleation and (b) progressive nucleation and for potentials of (c) 180 mV, (d) 200 mV and (e) 220 mV.

Considering that the system obeys the laws of progressive nucleation, the corresponding nuclear number density can be calculated from Equation 5.19 and from this, the nucleation rate, $AN_\infty$, can be obtained, which in turn gives the saturation number density, $N_{sat}$, for each potential.

Once it was ascertained that nucleation and growth takes place, the system was investigated under ultrasonic pulse conditions in order to attempt to dislodge the growing nuclei from the electrode surface. The potentials chosen were determined from the cyclic voltammograms. Interestingly, at low potentials (0 mV to 40 mV) the cyclic voltammogram predicts that no nucleation and growth should occur as

Table 6.1: Analysis of the current maxima. Data taken from Figure 6.8.

| $E$ (mV) | $-10^4 I_m$ ($Acm^{-2}$) | $t_m$ (s) | $10^8 I_m^2 t_m$ ($A^2cm^{-4}s$) | $10^{-7} AN_\infty$ ($cm^{-2}s^{-1}$) | $10^{-7} N_{sat}$ ($cm^{-2}$) |
|---|---|---|---|---|---|
| 40 | 2.95 | 1.03 | 8.97 | 3.54 | 2.11 |
| 50 | 3.21 | 0.76 | 7.82 | 6.54 | 2.87 |
| 60 | 3.30 | 0.49 | 5.33 | 15.7 | 4.45 |
| 70 | 3.55 | 0.39 | 4.94 | 24.5 | 5.56 |
| 80 | 3.61 | 0.24 | 3.13 | 65.0 | 9.05 |
| 90 | 3.78 | 0.18 | 2.52 | 121 | 12.3 |

these correspond to potentials more positive than the observed sharp increase in current, Figure 6.7. However, clear nucleation and growth *is* clearly observed in the corresponding $j - t$ transients at those potentials. On the basis of this the following conditions were employed: $E_1$ = -0.25 V, $t_1$ = 5 ms, $E_2$ = -0.15 V and $t_2$ = 400 ms. However, after 1 hour of electrolysis, the UV-Vis spectra showed that no gold nanoparticles were present in solution. The same result was also obtained even when the small nucleation pulse was not included and an extreme potential of -0.5 V was applied for the entire 400 ms. This can be attributed to the high affinity of gold for platinum which means that the ultrasonic pulse is insufficient to dislodge the growing nuclei from the electrode surface.

## 6.5 Glassy Carbon Electrode

The influence of the affinity of the electrode surface on the electrodeposited metal was investigated using glassy carbon as the working electrode. Glassy carbon is commonly used in electrochemistry due to its high resistance to chemical attack. Glassy carbon is also non metallic and therefore, the forces between the nucleating metal and the electrode are far weaker than in the case of platinum. It was considered that this should allow the deposited metal centres to be more easily dislodged when the ultrasonic pulse was applied.

In what follows, the synthesis of silver nanoparticles by the sonoelectrochemical technique is discussed. Experiments have been carried out in the presence and absence of polymer additives to provide stability to the materials produced.

### 6.5.1 5 mM $AgClO_4$ + 20 mM $HClO_4$

Figure 6.10 shows the cyclic voltammogram for this system. As expected, this is similar to that for the nucleation of silver on a platinum electrode. The potential where nucleation occurs, $E_{CRIT}$, is -0.027 V which is slightly more negative than that for platinum, which is -0.018 V.

Cyclic voltammetry was employed for the choice of the nucleation and growth potentials. The double potential step parameters chosen at first were: $E_1$ = -0.15 V, $t_1$ = 5 ms, $E_2$ = -0.035 V and $t_2$ = 400 ms. Once again, a stripping potential of +0.3 V was applied in between deposition periods to clean the electrode surface. However, after 1 hour of pulsing and in stark contrast with the behaviour observed for a platinum electrode 6.4.2, the UV-Vis spectra showed no presence of silver nanoparticles in solution. Therefore, more extreme potentials were employed. The nucleation potential, $E_1$, was increased to -0.3 V and the growth potential, $E_2$, was increased slightly to -0.08 V but this also failed to produce any silver nanoparticles.

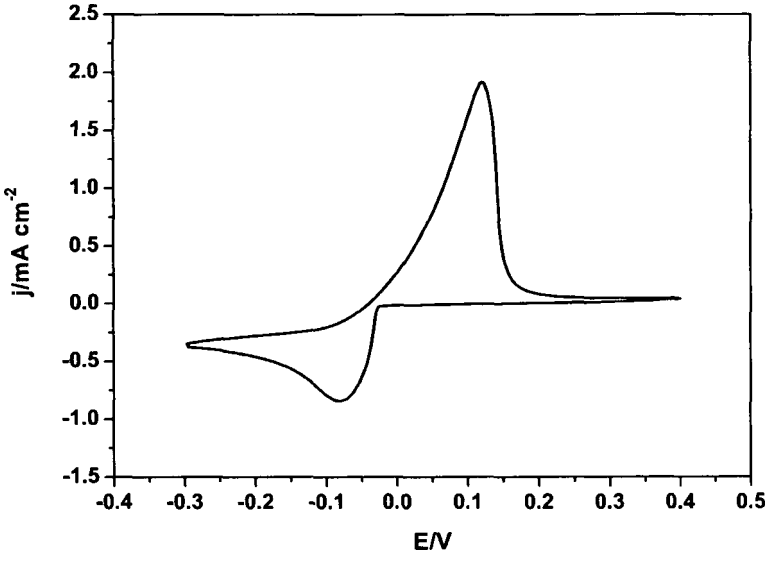


Figure 6.10: Cyclic voltammogram of glassy carbon in 5 mM $AgNO_3$ + 20 mM $HClO_4$ system. The potential scan started at 0.4V toward the negative direction and then reversed at -0.3 V. $\nu$ = 20 mV/s.

From the recorded current responses, it was clear that the moderate nucleation and growth potentials employed were insufficient to grow any stable nuclei at the electrode surface. However, as the nucleation and growth overpotentials were increased to more negative values, Figure 6.11, there was an associated increase in current density. As the potential was switched from $E_1$ to $E_2$, the appearance of an anodic current peak was observed, followed by an increase in current until the ultrasonic burst was applied. The presence of a large anodic peak indicates that significant number of nuclei had not reached the critical size at $E_2$ and hence, they dissolved. The increase in current density following the switch in potential, however, indicates that some nuclei remained on the electrode surface and continued to grow.

It is clear that by using separate nucleation and growth potentials, even when

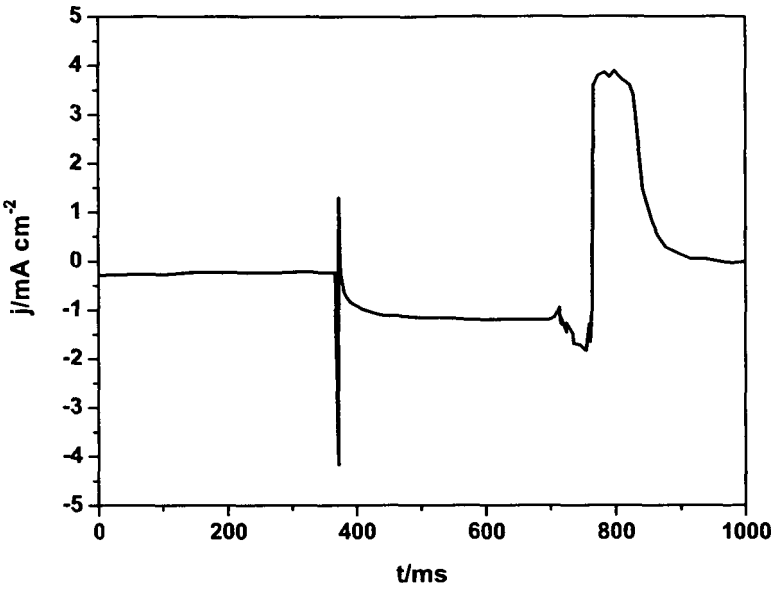


Figure 6.11: Current response for the nucleation and growth of silver on GC from 5 mM $AgClO_4$ + 20 mM $HClO_4$ for the following conditions: $E_1$ = -0.3 V, $t_1$ = 5 ms, $E_2$ = -0.08 V and $t_2$ = 400 ms. The noisy signal at ~700 ms is due to the ultrasonic burst used to dislodge the growing nuclei.

glassy carbon is employed as the working electrode, no stable nanoparticles were successfully produced. The reason for this could be a combination of various factors. It was found from previous experiments that using a high concentration of metal ions, the double potential step approach *does* successfully produce nanoparticles in solution but it was unsuccessful when this technique was applied to less concentrated solutions. It is possible that the technique is in fact working but due to the low concentration employed, the timescale of the experiments needs to be increased considerably. This is unfavourable since at longer times the stability of the nanoparticles in solution decreases. Furthermore, increased reaction time increases the electrodes susceptibility to degradation from prolonged ultrasonication [106].

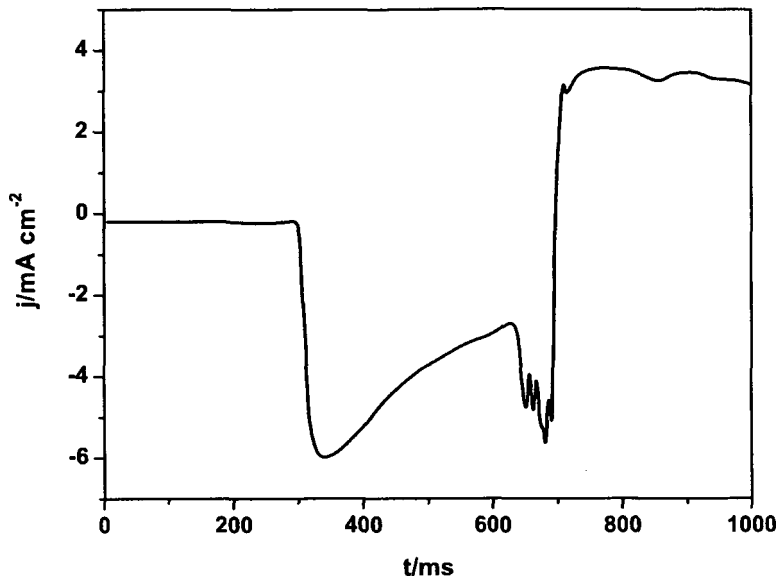


Figure 6.12: Current response for the nucleation and growth of silver on GC from 5 mM $AgClO_4$ + 20 mM $HClO_4$ at a continuous potential of -0.5 V for 400 ms. The large noise at ~700 ms is due to the ultrasonic burst used to dislodge the growing nuclei into solution.

Since the elegant approach of employing a nucleation and a growth pulse failed to produce any nanoparticles in solution, it was investigated whether a large single pulse, sustained for the duration of the pulse profile, could lead to the formation of stable nanoparticles, as previously observed in Section 6.4.2 for a Pt electrode. Figure 6.12 shows the corresponding current response and a significant increase in the current density is observed compared with the results in Figure 6.11. The corresponding UV-Vis spectra of the solution is shown in Figure 6.13. The characteristic plasmon band associated with silver nanoparticles is observed at ~420 nm, indicating their presence in solution.

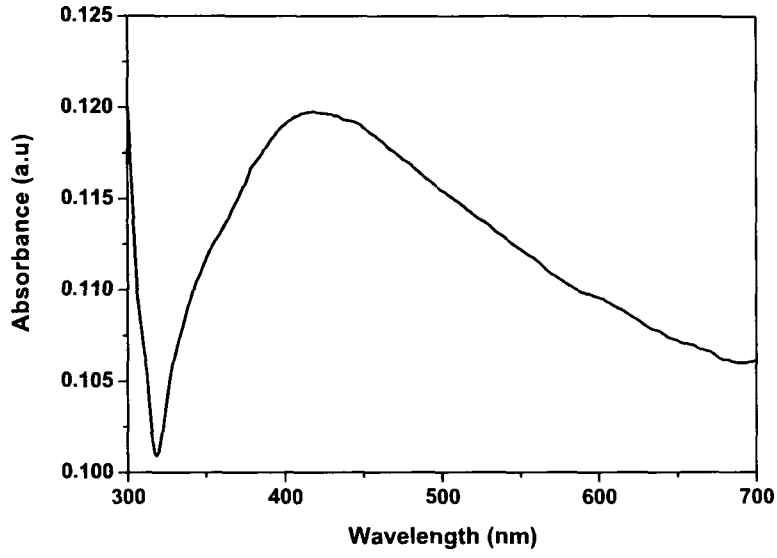


Figure 6.13: UV-Vis spectra of the as-prepared silver nanoparticles formed by repeated nucleation, growth and ultrasonic dislodgement from glassy carbon in a 5 mM $AgClO_4$ + 20 mM $HClO_4$ solution from a single growth potential of -0.5 V for 400 ms.

### 6.5.2 5 mM $AgClO_4$ + 20 mM $HClO_4$ + 0.2 g/l PVP55

PVP was employed as a stabilising agent in the preparation of silver nanoparticle dispersions. In the first experiments, a low concentration of a high molecular weight polymer (PVP55, $M_w$=55,000) was employed in order to minimise its effect on nucleation but maximise the interaction between the nanoparticles and the long alkane chain of the polymer .

The voltammetric behaviour of $AgClO_4$ at the glassy carbon electrode changed greatly after the addition of PVP55. By comparing the CV's in the presence and absence of PVP55, Figure 6.14, it is found that PVP shifts the deposition potential to a more negative value (-0.08 V) compared to -0.035 V without PVP. This shift is most probably due to competition for surface sites of $Ag^+$ ions with adsorbed PVP. PVP is a large polymeric molecule and will be strongly specifically

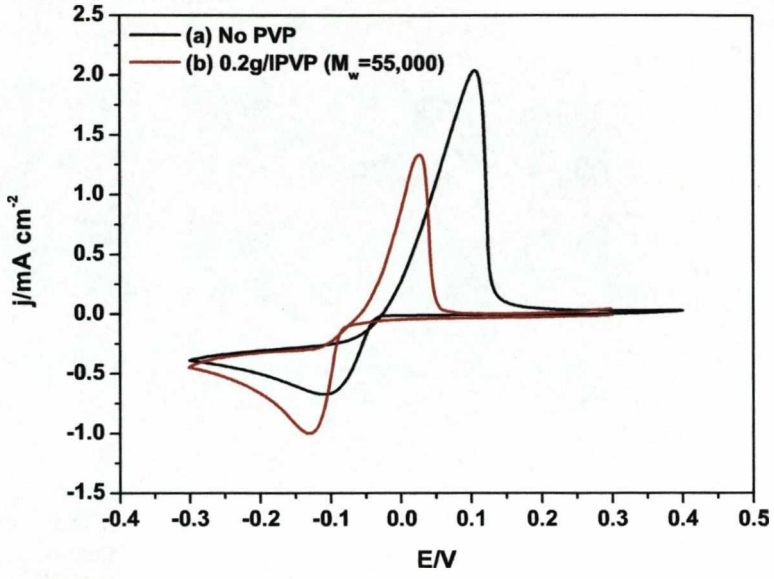


Figure 6.14: Cyclic voltammograms for the reduction of silver species at a GC electrode in 5 mM $AgClO_4$ + 20 mM $HClO_4$ (a) without and (b) with the addition of 0.2 g/l PVP55. $\nu = 20$ mV/s.

adsorbed through the lone electron pairs at the oxygen atoms. This restricts the availability of surface sites resulting, therefore, in a larger nucleation overpotential. The increase in current density of the nucleation peak is a consequence of the increase in the nucleation overpotential, this causes a sudden decrease in the surface concentration of the $Ag^+$ ions at the onset of the electrodeposition at potentials more negative than the corresponding reversible value. The total charge of the cathodic sweep in the absence and presence of PVP55 is $-1.9\times10^{-3}$ C and $-2.2\times10^{-3}$ C, respectively, indicating that PVP has little effect on the amount of silver deposited. However, the total charge of the stripping peaks are $1.6\times10^{-3}$ C and $6.4\times10^{-4}$ C. If dendritic or 1D diffusional growth occurs it is possible that these deposits are cut off by silver dissolution close to the electrode surface during the anodic sweep, thereby promoting the formation of silver nanostructure

in solution but also decreasing the total anodic charge measured in the cyclic voltammogram.

The lower value of the oxidation peak charge could be attributed to direct reduction of $Ag^+$ ions to nanoparticles in the negative sweep. It has been observed that the use of PVP greatly inhibits the electroreduction of $Au^{III}$ [188] and $Ag^+$ [113, 190], making particle formation dominate over electrodeposition.

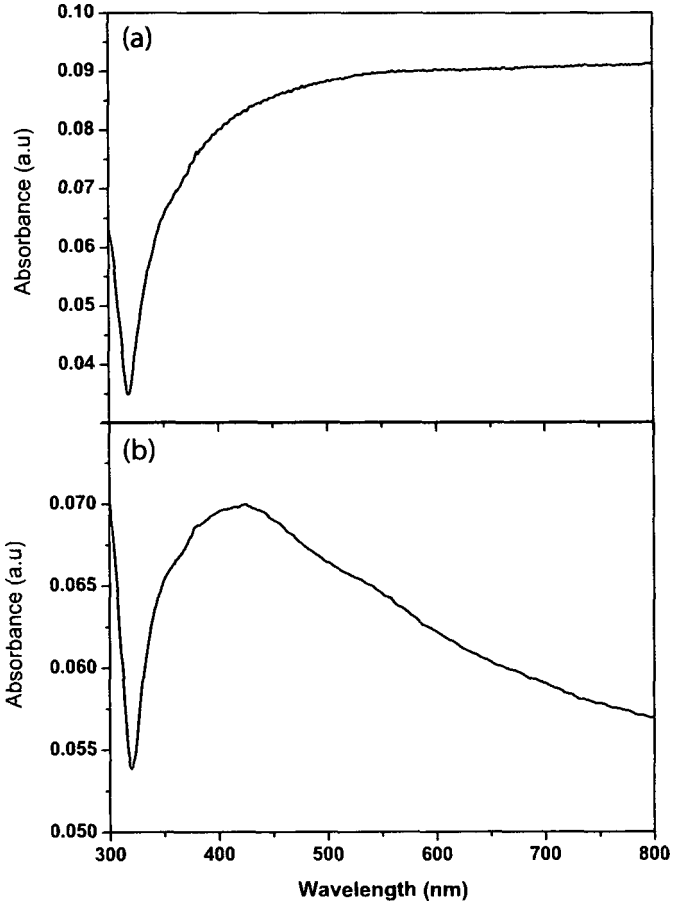


Figure 6.15: UV-Vis spectra of silver nanoparticles formed by repeated nucleation, growth and ultrasonic dislodgement from GC /5 mM $AgClO_4$ + 20 mM $HClO_4$ + 0.2 g/l PVP55 solution from a single growth potential of -0.5 V for 400 ms. (a) original solution and (b) after centrifugation at 500 rpm for 10 minutes.

Figure 6.15 shows the UV-Vis spectra of the 5 mM $AgClO_4$ + 20 mM $HClO_4$ + 0.2 g/l PVP55 solution after 30 minutes of electrolysis at a potential of -0.5 V

for 400 ms followed by dislodgement using ultrasound. The as-prepared solution, Figure 6.15 (a), exhibits a very broad absorbance compared to the UV-Vis spectra in the absence of PVP55, Figure 6.13. This is most probably a direct result of the stabilising effect of PVP on a wide range of sizes of nanoparticles formed. It is very probable that dendritic growth is observed at the extreme potential employed during growth. These structures are then stabilised by the PVP in solution and contribute to the broad absorption band observed. Furthermore, it is possible that PVP directs growth at the electrode surface. In the absence of PVP, nucleation can readily occur at any site on the electrode surface but with the addition of PVP, it is likely that nucleation can only occur at certain interstitial sites inhibiting normal 3D hemispherical diffusional growth and hence promoting 1D diffusional growth. This would lead to a broad distribution of shapes produced in solution.

In addition, silver ions are coordinated by the nitrogen groups in the polymer and these localised $Ag^{+}$-PVP complexes can generate many silver nuclei along the polyvinyl chain of PVP, which could subsequently grow into larger nanoparticles. Since PVP adopts a random coil configurations, PVP could greatly increase the probability of 1-D nanoparticle aggregate formation [188].

If this were the case then it should be possible to removed these larger nanoparticles by centrifugation. Figure 6.15 (b) shows the remarkable spectral changes taking place after centrifugation at 500 rpm for 10 minutes. A plasmon band becomes clearly visible with a peak at ~420 nm. The band is still broader than expected indicating the presence of larger shapes still in solution. The nanoparticles produced were only stable for a few hours after formation and precipitated from solution when left overnight. This could be attributed to the low PVP/Ag ratio employed.

Under similar conditions, Jiang et at. [114], produced stable PVP stabilised silver nanoparticles. In their approach nanoparticles were formed in the absence

of a complex nucleation and growth pulse profile but instead, a constant current regime was employed coupled with alternate ultrasonic pulses to dislodge the grown deposit from the electrode. The same concentration of PVP as employed in the present work was also used as a stabilising agent for the silver nanoparticles. It was observed that as the concentration of PVP was increased, spherical monodisperse nanoparticles were formed. Since stabilisation is a key factor in this work, a higher concentration of PVP was investigated.

### 6.5.3 5 mM $AgClO_4$ + 20 mM $HClO_4$ + 1 g/l PVP55

To increase the stability of the silver nanoparticles synthesised by the method described in Section 6.5.2, the concentration of PVP was increased from 0.2 to 1 g/l. The cyclic voltammogram for the higher concentration of PVP55, compared with that of 5mM $AgClO_4$ + 20mM $HClO_4$ in the absence of PVP, is shown in Figure 6.16. The voltammetric response is similar to that observed for the lower concentration of PVP55, with a shift in the potential at which silver deposition occurs to more negative values. However, there is a minor shift in the nucleation potential, which is unexpected. Similarly, there is also a negative shift in the potential of the anodic peak which could be a consequence of the coordination of $Ag^+$ ions by the polymer.

The corresponding UV-Vis spectra is shown in Figure 6.17 (a). Similarly to the results obtained with the 0.2 g/l PVP55 solution, a broad adsorption was observed after 30 minutes of electrolysis at -0.5 V. Interestingly, when the solution was centrifuged, initially at 500 rpm for 10 minutes and then at 1000 rpm for a further 10 minutes, the plasmon band remained unchanged, Figure 6.17 (b)-(c). It has been shown in previous experiments that centrifugation successfully removes larger nanoparticles from solution, making the plasmon band better defined. There is, however, a decrease in the absorbance observed as the centrifugation time is increased, indicating a decrease in the concentration of the nanoparticles.

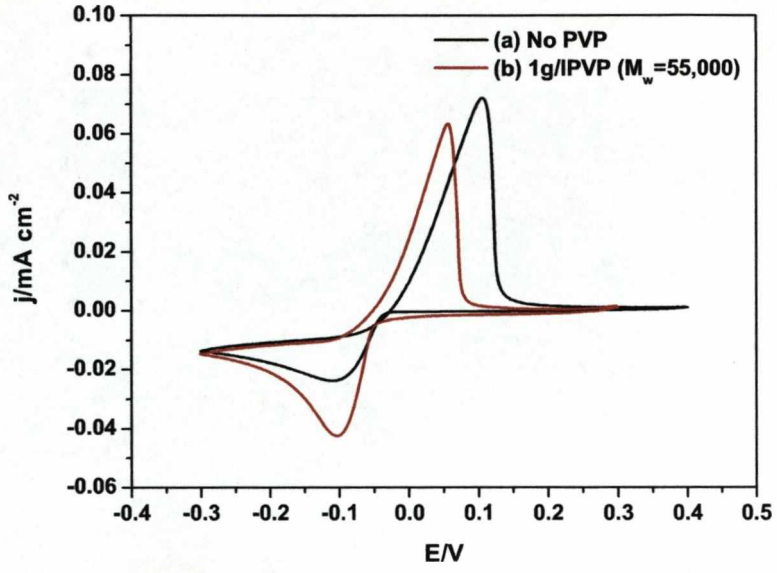


Figure 6.16: Cyclic voltammograms for silver electroreduction at a GC electrode in 5 mM $AgClO_4$ + 20 mM $HClO_4$ (a) without and (b) with the addition of 1 g/l PVP55. $\nu = 20$ mV/s.

The similarity of these spectra indicates that there are no significantly large particles in solution that can be removed by centrifugation at the rotational speed employed, as compared with the results for the lower concentration of PVP55. This infers that the nanoparticles synthesised are smaller than those obtained at the lower concentration of PVP55. A large size dispersion of nanoparticles is still observed, albeit of smaller sizes than those previously synthesised. TEM images of the as-prepared solution confirmed a large distribution of sizes. These images can be seen in Figure 6.25 at the end of this Chapter.

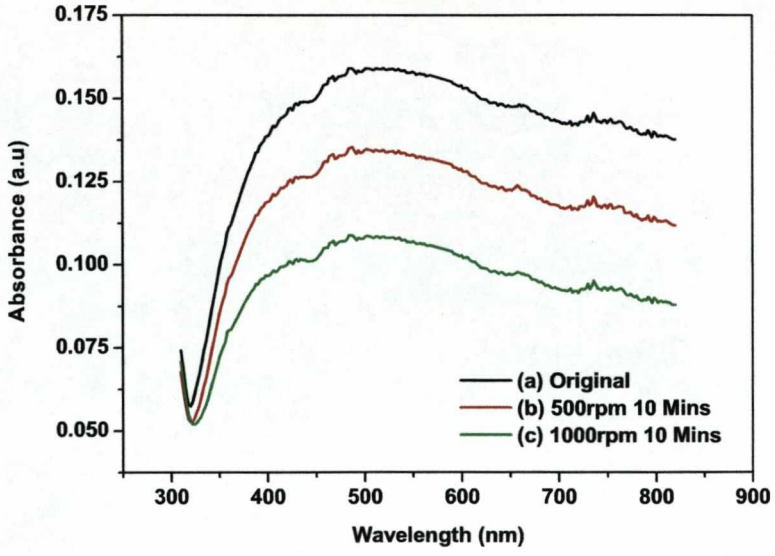


Figure 6.17: UV-Vis spectra of silver nanoparticles formed by repeated nucleation, growth and ultrasonic dislodgement from GC/5 mM $AgClO_4$ + 20 mM $HClO_4$ + 1 g/l PVP55 solution from a single growth potential of -0.5 V for 400 ms. (a) as-prepared solution and after centrifugation at (b) 500 rpm for 10 minutes and (c) 1000 rpm for 10 minutes.

### 6.5.4 5 mM $AgClO_4$ + 20 mM $HClO_4$ + 10 g/l PVP55

The role of PVP as a stabilising agent for metallic nanoparticles is well documented [32, 38, 113, 114, 186, 190, 191] and PVP plays a crucial part in the formation of nanosized materials. The reported concentration of PVP employed in the stabilisation of nanoparticles varies greatly. In aqueous medium, a PVP concentration as low as 0.2 g/l produces monodisperse silver nanoparticles in a high yield [114]. Yin et al. observed that by increasing the mass concentration ratio of PVP/$Ag^+$ from 50:1 to 1000:1 (30 g/l), the surface plasmon band of the synthesised silver nanoparticles became more symmetrical and a blue shift in the maximum of the plasmon peak was observed, indicating small particle size and uniform size distribution [113]. Similarly, Huang et al. investigated the effects of

increasing PVP concentration from 10 g/l to 30 g/l in the electrochemical synthesis of gold nanoparticles and observed the same effect as Yin et al. [188]. However, a high PVP monomeric unit/$Ag^+$ ratio can also be disadvantageous for the electrochemical synthesis of nanoparticles, since a high PVP concentration greatly increases the viscosity of the solution and therefore lowers the transfer rate of silver ions to the electrode, which increases the time necessary to complete the nucleation and growth cycles.

To study the effect of increasing significantly the concentration of PVP on the formation of nanoparticles an increased concentration of 10 g/l was investigated. Figure 6.18 compares the corresponding cyclic voltammogram (a) without and (b) with the addition of 10 g/l PVP55.

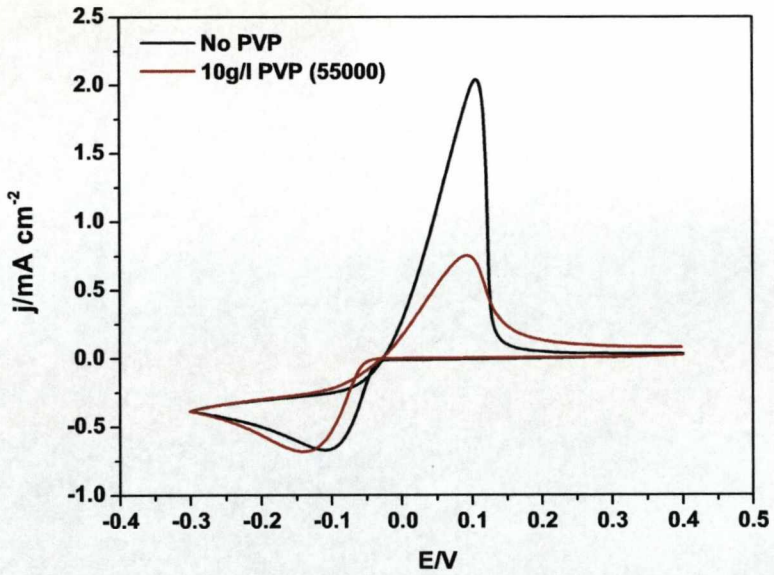


Figure 6.18: Cyclic voltammograms for the electrodeposition of silver species at a GC electrode in 5 mM $AgClO_4$ + 20 mM $HClO_4$ (a) without and (b) with the addition of 10 g/l PVP55. $\nu = 20$ mV/s.

As observed with the lower concentrations of PVP55 (Figures 6.14 and 6.16),

the current density of the oxidation peak is greatly reduced by the addition of PVP compared to a solution in its absence. As discussed earlier, this decrease is probably due to the dissolution or dislodgement of silver nanoparticles stabilised by PVP formed when the potential was scanned in the negative direction [113]. It was observed for both 0.2 g/l and 1 g/l PVP55 solution that the addition of the polymer greatly affected the cathodic voltammetric behaviour. As the PVP concentration was increased to 10 g/l this remains relatively unchanged with only a slight negative shift of the cathodic peak, showing that the electrodeposition rate is slightly lowered [190].

The nucleation and growth cycle was repeated by applying a potential of -0.5 V for 400 ms and the growing nuclei were dislodged using ultrasound. The observed current response is shown in Figure 6.19. The current density of the transient observed is significantly lower than that in the absence of PVP, Figure 6.12. The results in Figure 6.12 clearly show the rising section of a typical $j-t$ transient indicating that nucleation and 3-D growth is occurring. In contrast in the presence of PVP55, Figure 6.19 (a), after the current maximum is reached, a slowly decaying current transient is observed indicating the possible formation of 1-D structures at the electrode surface. After 1 hour of electrolysis there is a change in the current transient with the nucleation and growth regions occurring in a much shorter time scale, probably due to the presence of nuclei remaining on the surface. The similarity in the growth region of the pulse indicates that the nanoparticles formed are probably of similar size.

Figure 6.20 shows the UV-Vis spectra of the solution taken after 1 hour of electrolysis (trace (a)) and that of a control solution of aqueous 10 g/l PVP55 (trace (c)). A very broad absorbance peak is observed indicating a large dispersion of shapes in solution. Upon centrifugation at 1000 rpm for 10 minutes the spectrum becomes better defined indicating the removal of the larger particles, Figure 6.20 (b). Broad bands between 500 nm and 700 nm are observed in both

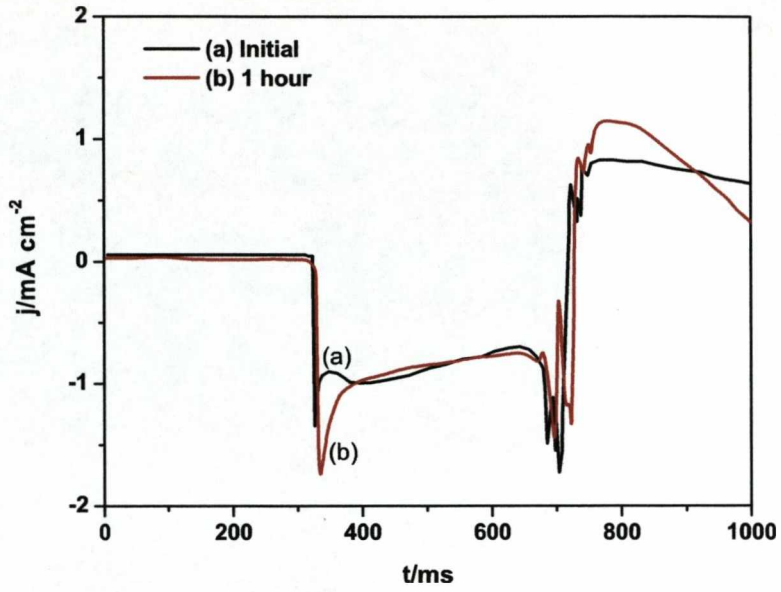


Figure 6.19: Current response for the nucleation and growth of silver on glassy carbon from 5 mM $AgClO_4$ + 20 mM $HClO_4$ + 10 g/l PVP55 at a continuous potential of -0.5 V for 400 ms recorded (a) initially and (b) after 1 hour of pulsing. The large noise at ~700 ms is due to the ultrasonic burst used to dislodge the growing nuclei.

spectra. From trace (c) it is clear that these features can be attributed to the PVP present in a high concentration. The origin of these is not fully understood and these peaks were not observed by Yin, Huang and co-workers. This is probably due to the high yield of nanoparticles synthesised in their work masking the weak absorbance bands of PVP55. However, due to the low yield of nanoparticles formed by the present method, these additional peaks are visible. The presence of silver nanoparticles, however, is confirmed in both spectra (a) and (b) from the presence of the ~400 nm characteristic band.

Using the PVP spectra as a background, a more realistic plasmon absorbance was obtained by subtracting this contribution from the absorbance of the original

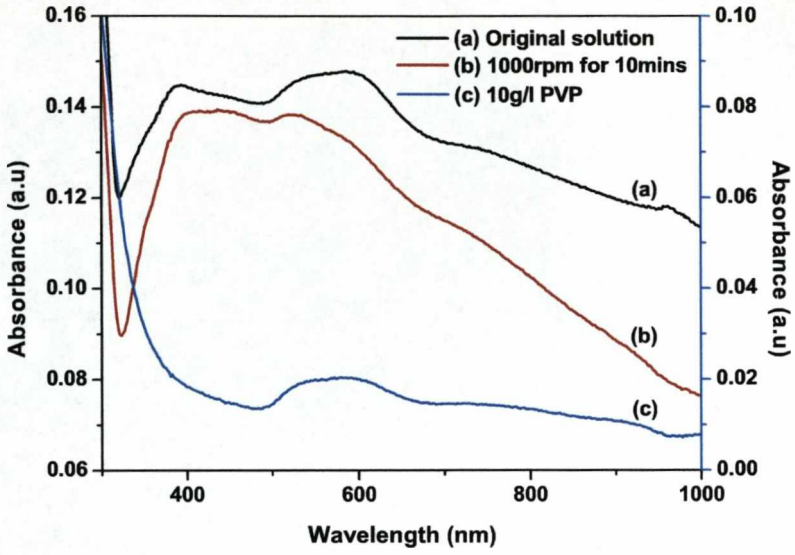


Figure 6.20: UV-Vis spectra of (a) the as-prepared silver nanoparticles, (b) after centrifugation at 1000 rpm for 10 minutes and (c) an aqueous solution of 10 g/l PVP55.

solution and the results are shown in Figure 6.21 (a) and (b), showing a much better defined and characteristic plasmon band. Upon centrifugation two bands become clear at ~400 nm and ~460 nm indicating the presence of at least two different size distributions of nanoparticles. However, the broad band at higher wavelengths shows that a large distribution of sizes is present although the samples were centrifuged. TEM images of the prepared solution confirmed this. These images can be seen in Figure 6.26 at the end of this Chapter.

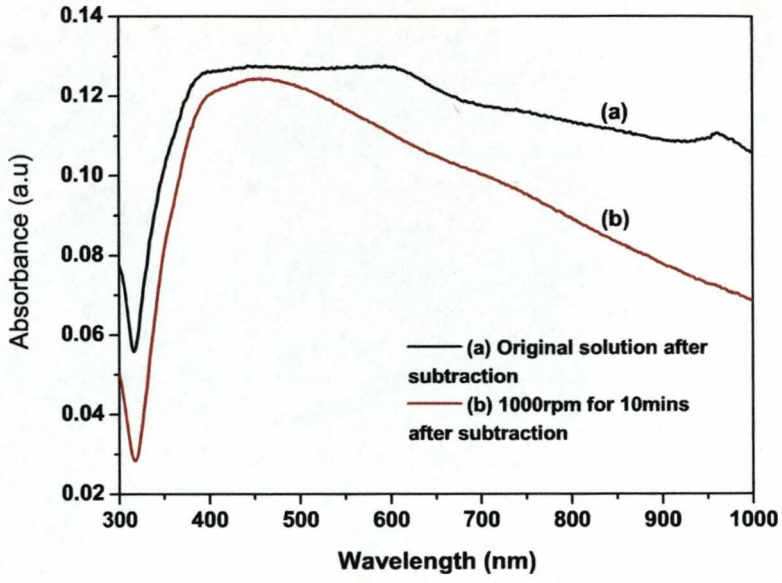


Figure 6.21: UV-Vis spectra obtained by subtraction of the absorption spectrum of 10 g/l PVP55 (Figure 6.20 (c)) for (a) as-prepared solution and (b) after centrifugation at 1000 rpm for 10 minutes.

### 6.5.5 5 mM $AgClO_4$ + 20 mM $HClO_4$ + 2 g/l PVP10

To investigate the influence of PVP chain length on nanoparticle formation, PVP10 was employed. This polymer has a molecular weight of 10,000. For comparison with the results described in Section 6.5.2, the polymer concentration was increased by a factor of 10 so that the number of PVP active sites available for coordination to $Ag^+$ was the same as in the previous experiments.

Figure 6.22 compares the cyclic voltammograms for silver electrodeposition with the addition of (a) 0.2 g/l PVP55 and (b) 2 g/l PVP10. The voltammetric behaviour showed minor changes when the PVP chain unit length was decreased. There is, however, a slight positive shift in the nucleation potential to -0.06 V compared with PVP55. This value is still more negative than the potential observed in the absence of PVP (-0.035 V), which indicates that PVP10 does influence

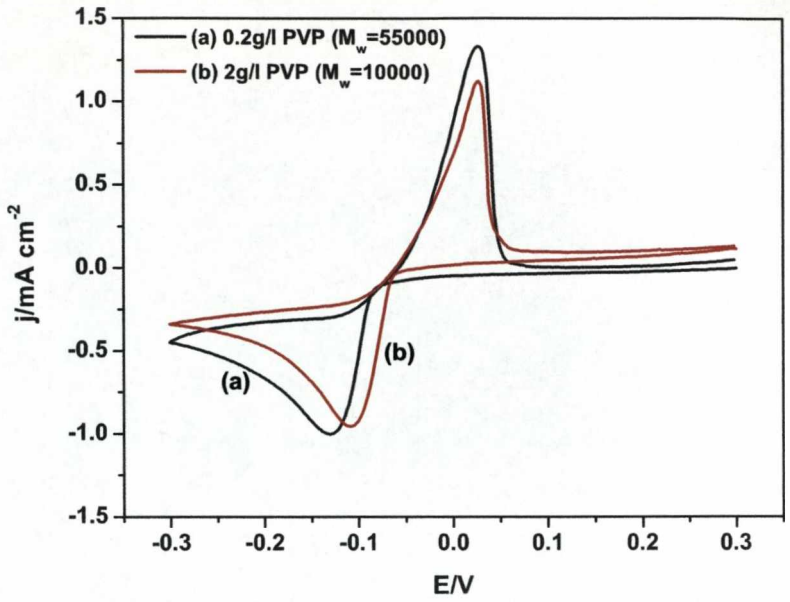


Figure 6.22: Cyclic voltammograms for the electrodeposition of silver at a GC electrode in 5 mM $AgClO_4$ + 20 mM $HClO_4$ with the addition of (a) 0.2 g/l PVP55 ($M_w$=55,000) and (b) 2 g/l PVP10 ($M_w$=10,000). $\nu$ = 20 mV/s.

silver nucleation, albeit to a lesser extent than PVP55. Furthermore, a small decrease in the current density of the oxidation peak is observed which indicates that electrodeposition is slightly suppressed.

The same experimental conditions used for the formation of silver nanoparticles stabilised by PVP55 were applied for the PVP10 system. Figure 6.23 (a) shows the UV-Vis spectra of the solution after 1 hour of electrolysis at a constant potential of -0.5 V. As previously observed, the spectrum is very broad indicating a large size distribution of particles in solution, although, the characteristic plasmon resonance of silver nanoparticles is observed at ~428 nm. Centrifugation at 1000 rpm for 10 minutes reduced the broadness of the plasmon band and a second peak became visible, Figure 6.23 (b). Deconvolution of the plasmon band using a Lorentzian peak fitting algorithm (Origin Software, ver. 7) showed an excellent fit employing three peaks. Two distinct peaks are observed at 410 nm and 490 nm, respectively and a broad band at ~590 nm. The predominant peak at 490 nm did not appear

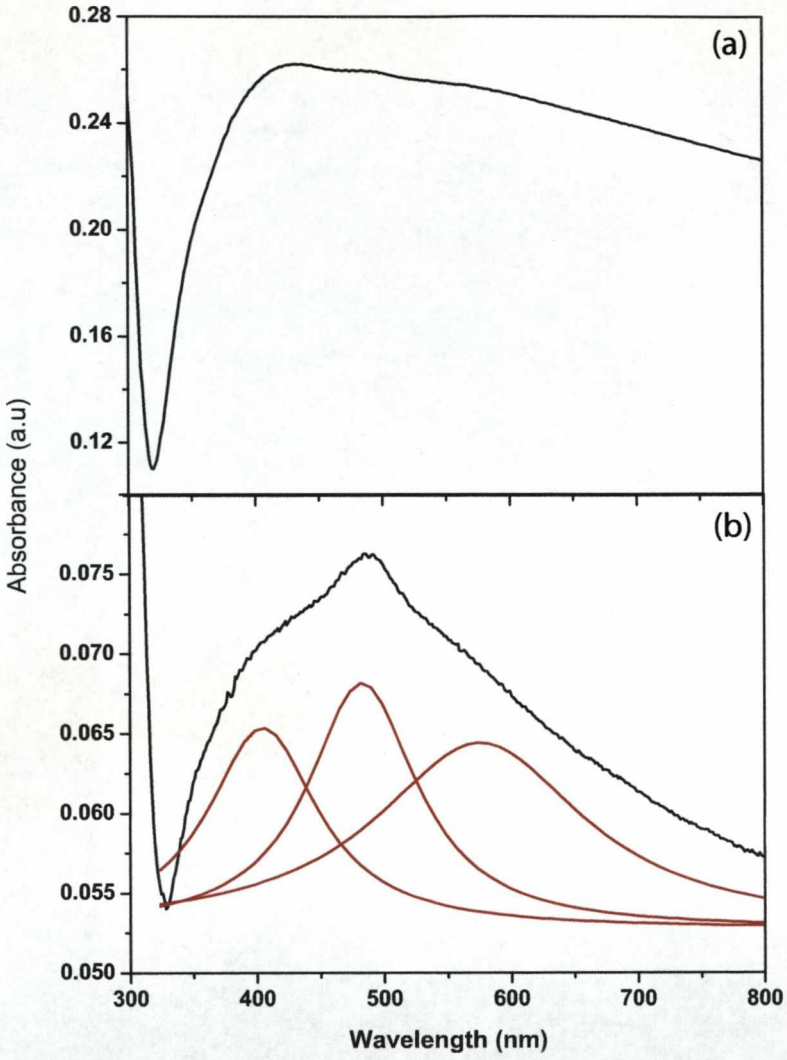


Figure 6.23: UV-Vis spectra of silver nanoparticles formed by repeated nucleation, growth and ultrasonic dislodgement from glassy carbon in a 5 mM $AgClO_4$ + 20 mM $HClO_4$ + 2 g/l PVP10 solution from a single growth potential of -0.5 V for 400 ms. (a) original solution obtained and (b) after centrifugation at 1000 rpm for 10 minutes. The corresponding deconvolution peaks using a Lorentzian peak fitting algorithm are also shown in the figure.

when PVP55 was employed as a stabilising agent which indicates that the PVP chain length does influence the size and morphology of the particles formed by this synthetic method.

It is clear that by altering the concentration and chain length of PVP used for

the stabilisation of nanoparticles it is possible to influence the sizes and shapes obtained. Yin et al. [113] and Huang et al. [188] observed that the length of PVP10, was insufficient to fully stabilise the synthesised gold nanoparticles and produced large aggregated particles and gold nanoparticles of various shapes such as triangular, hexagonal and polyhedral geometries were obtained. Wang et al. [188] proposed that PVP10 is expected to play an important role in the synthesis of gold nanoparticles with special shapes.

The UV-Vis spectra of PVP10 itself was measured to investigate whether any of the band observed in the spectrum in Figure 6.23 (b) where associated with PVP. This is shown in Figure 6.24. Clearly, PVP10 has a weak absorbance in aqueous solution at this concentration and the bands observed in Figure 6.23 (b) are solely due to the plasmon resonance of the silver nanoparticles.

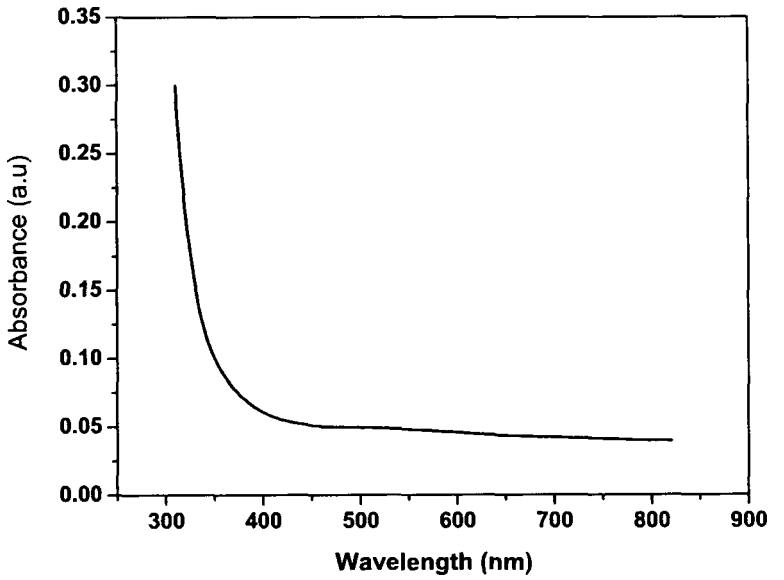


Figure 6.24: UV-Visible absorption spectrum of an aqueous 2 g/l PVP10 solution.

As a control experiment, a solution of 5 mM $AgClO_4$ + 20 mM $HClO_4$ + 10

g/l PVP55 was investigated without the addition of the ultrasonic pulse employed to remove the growing nuclei from the electrode surface. All other experimental conditions remained the same as detailed in Section 6.5.3. After 1 hour of electrolysis no colour change in the solution was observed and the UV-Vis spectra of the solution showed no absorption. Upon inspection of the glassy carbon, at the end of electrolysis, silver deposition was observed. Evidently, the ultrasonic pulse plays a crucial role in the formation of nanoparticles in the method used in the present work.

## 6.6 Mechanism of nanoparticle stabilisation by PVP

The mechanism of PVP protection can be divided into three parts. 1) Initial coordination, 2) assisted reduction and 3) protection from agglomeration.

1. The lone pair electrons of both the oxygen and nitrogen atoms in the PVP monomers can occupy two sp orbitals of the $Ag^+$ ions and form a dative coordination complex. Two possible complex structures have been proposed. Electron donation from a single PVP unit may occupy the two sp orbitals of a silver ion or two oxygen atoms from two neighbouring PVP units may simultaneously coordinate with one silver ion [180, 188]; in both cases, this effectively stabilizes the $Ag^+$ ions. The importance of this is that the polymer confines $Ag^+$ ions within a semi-rigid structure and this restricts their mobility thus meaning that well defined growth sites are available by coordination. Information reported in the literature on the changes in the reduction potential of $Ag^+$ by coordination by PVP are misleading [113, 186].

2. Due to its structure, PVP allows many silver ions to be anchored to the hydrophobic groups situated along its chain length. Once an attached silver

ion accepts an electron, either by chemical reduction from a reducing agent or by electron transfer from an electrode surface, the formation of metal nanocluster becomes possible. These clusters can then act as growth centres by electron transfer and promote further electrochemical reduction of other silver ions down the PVP chain, leading to the formation of more silver nuclei. Ma et al. [190] proposed that due to the dynamic curl and stretch of the PVP backbone even metal nuclei far removed from the electrode can come sufficiently close to the surface for electron transfer to occur and hence form new silver clusters, increasing significantly the yield of nanoparticles formed.

3. The steric effect of PVP also prevents the coalescence of the silver clusters during growth since the hydrophobic backbone of the PVP wraps tightly around the silver particles inhibiting particle-particle contact. This means that PVP not only promotes the nucleation of silver nanoparticles but also inhibits their aggregation [192]. From an FTIR investigation Yin et al. [113] observed from a comparison of PVP and PVP stabilised silver nanoparticles, that the stretching vibration band of C=O at 1665 $cm^{-1}$ disappeared indicating that the PVP molecules are indeed strongly adsorbed onto the surface of the silver particles through coordination between the silvers atom and the oxygen atom of the carbonyl group.

For the above reasons, PVP appears to be a very useful stabilising agent for the sonoelectrochemical synthesis of silver nanoparticles as demonstrated in the present work by the several systems investigated.

## 6.7 TEM characterisation

Transmission electron microscopy was employed to image the as-prepared nanoparticles synthesised from the technique described in this Chapter. Figure 6.25 shows TEM images of samples of silver nanoparticles synthesised from 5 mM $AgClO_4$ + 20 mM $HClO_4$ employing 1 g/l PVP55 is a stabilising agent after centrifugation. A broad distribution of shapes is observed even after centrifugation at 1000 rpm for 10 minutes. This confirms the results obtained from the corresponding UV-Vis spectra shown in Figure 6.17 where a broad surface plasmon resonance was observed for the same solution. Partial aggregation is also observed indicating that the concentration of PVP employed in this preparation was not high enough to fully stabilise the nanoparticles formed.

Three distinct sizes of nanoparticles are apparent as shown in Figure 6.25. Large nanocrystals with an average size of (167±41) nm, Figure 6.25 (a) and two smaller sized particles with an average size of (7.5±1.7) nm and (3.5±0.5) nm, respectively, Figure 6.25 (b) and (c). The size distribution of both the smaller nanoparticles is much narrower than that of the larger nanocrystals, which showed significant polydispersity. Many of the larger sized particles were hexagonal, well-defined geometric shapes showing preferential crystallographic growth directions. This could be due to crystal growth during sample preparation. PVP is known to interact with the FCC faces promoting growth on the 100 direction [193]. It is unclear from the results in Figure 6.25 (b) and (c) whether the smaller sized nanoparticles were produced at the electrode surface during electrolysis or if the larger of the two were formed from partial aggregation of the smaller particles due to an insufficiently high PVP concentration. The formation of such small uniform monodispersed nanoparticles was unexpected since the extreme potential applied during nucleation and growth (-0.5 V) would be expected to result in dendritic growth.

As the PVP concentration in solution was increased to 10 g/l (PVP55), the size

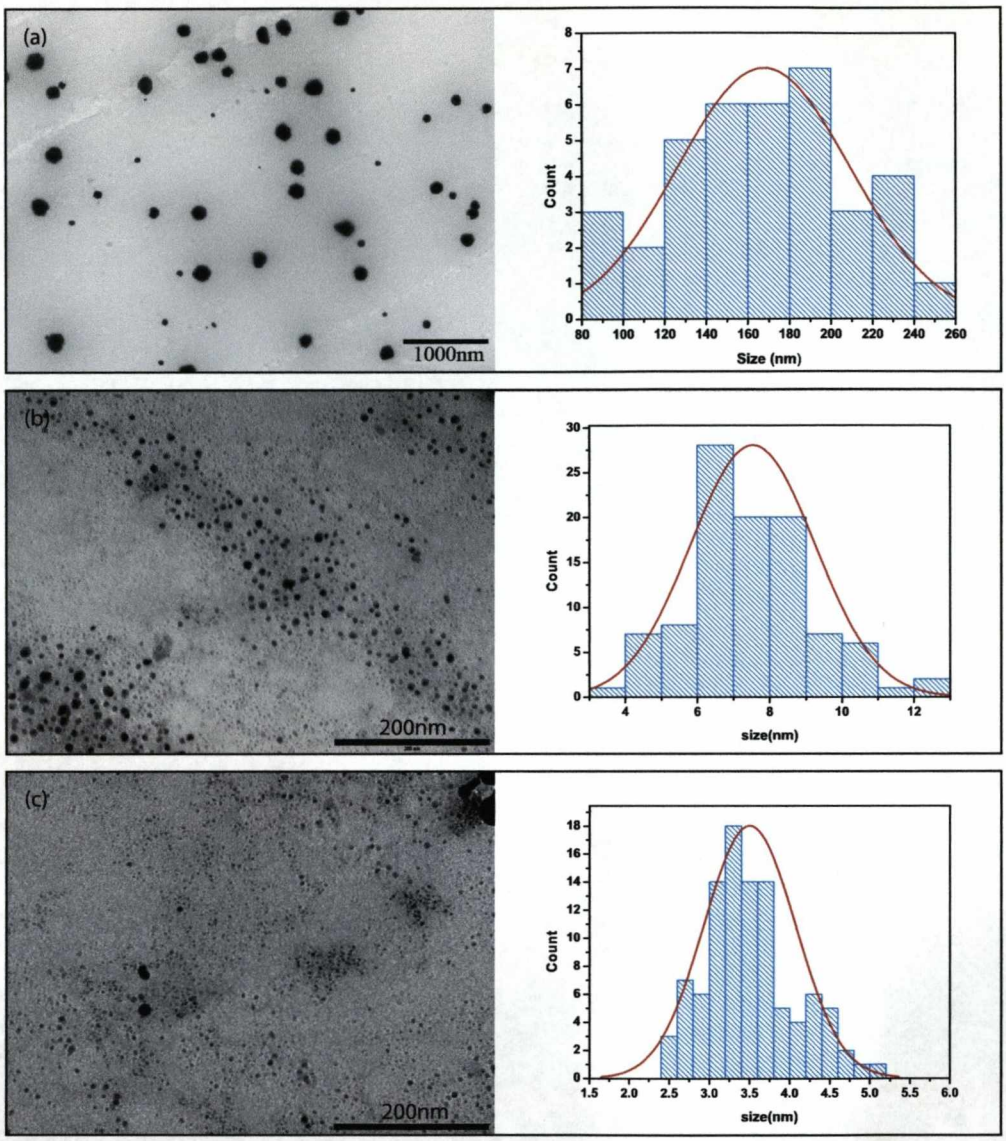


Figure 6.25: TEM images (a)-(c) of the different sized silver nanoparticles formed by repeated nucleation, growth and ultrasonic dislodgement from GC/5 mM $AgClO_4$ + 20 mM $HClO_4$ + 1 g/l PVP ($M_w$=55,000) solution from a single growth potential of -0.5 V for 400 ms along with their corresponding particle size distribution histograms.

and morphology of the nanoparticles synthesised changed significantly compared with the lower concentration of PVP. Three distinct sizes of particles were again observed in the as-prepared solution. Spherical particles with an average size of

(50±5) nm, which were observed over the entire area of the TEM grid, Figure 6.26 (a), and were monodisperse in size and shape. Dog-bone shaped nanorods were also observed with an average length and width of (60±8) nm and (25±4) nm giving an average aspect ratio of 2.4, Figures 6.26 (b) and (c), and finally, large dendritic formations, Figure 6.26 (d), were also observed.

The presence of these three types of objects in solution explains the broad plasmon band observed in the UV-Vis spectra of their solution, Figure 6.21. The two clear plasmon resonances observed at ~400 nm and ~460 nm can be attributed to the spherical particles and dog-bone shaped nanorods. As observed in Chapter 3, Section 3.5 for gold nanorods, their shape and aspect ratio greatly influences the position of the longitudinal plasmon resonance. The low aspect ratio of the silver nanorods produced means the longitudinal plasmon band should be observed at a slightly higher wavelength than the transversal plasmon band, as observed. Furthermore, the presence of large dendritic structures in solution explains the broad shape of the plasmon resonance at higher wavelengths.

As the PVP55 concentration was increased to 30 g/l only large dendrites and spherical nanoparticles were produced and no rod shaped nanoparticles were observed, Figure 6.27. The spherical nanoparticles were polydisperse with an average size of (34±9) nm. Evidently, increasing the PVP55 concentration above 10 g/l is unfavourable in this synthetic route. This is possibly due to reduced mass transport of the $Ag^+$ ions in solution due to the increased viscosity and perhaps more importantly, increased competition of the $Ag^+$ ions with PVP at the electrode surface.

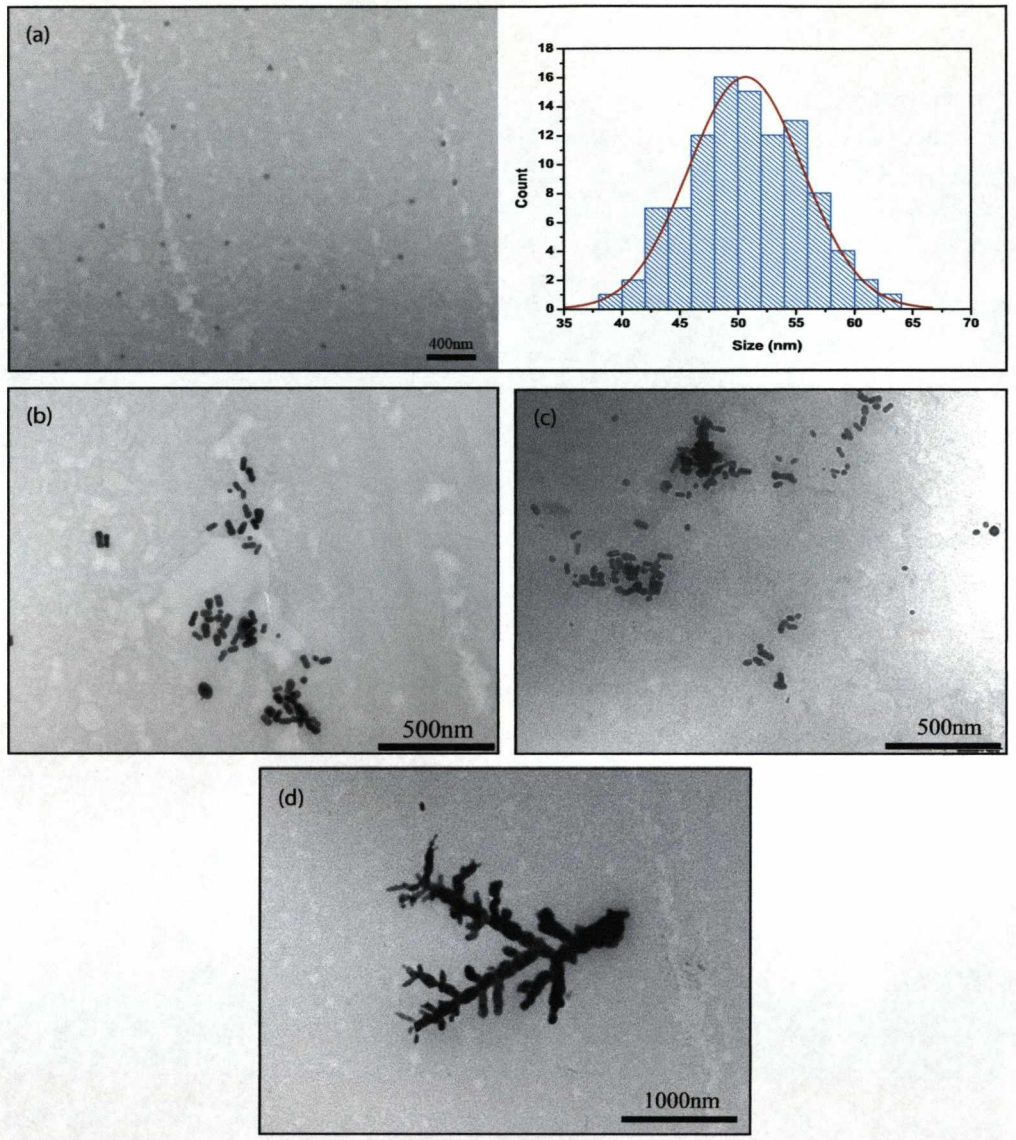


Figure 6.26: TEM images (a)-(d) of the variety of different shaped silver nanoparticles formed by repeated nucleation, growth and ultrasonic dislodgement from GC/5 mM $AgClO_4$ + 20 mM $HClO_4$ + 10 g/l PVP ($M_w$=55,000) solution from a single growth potential of -0.5 V for 400 ms along with their corresponding particle size distribution histograms.

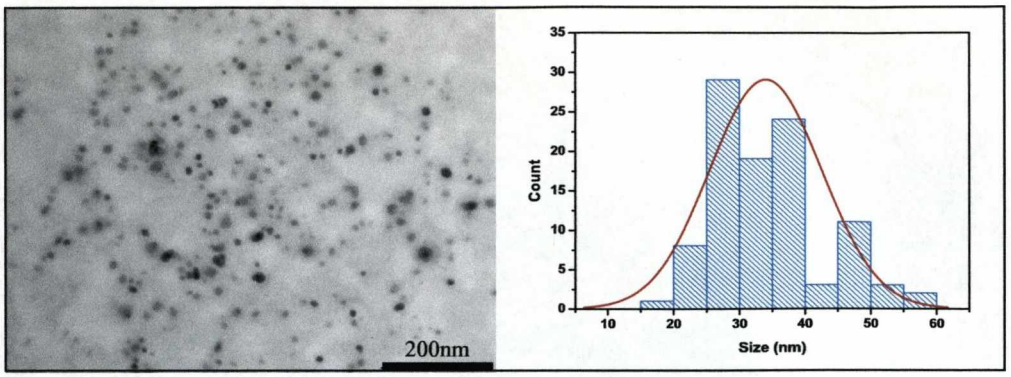


Figure 6.27: TEM image of the silver nanoparticles formed by repeated nucleation, growth and ultrasonic dislodgement from GC/5 mM $AgClO_4$ + 20 mM $HClO_4$ + 30 g/l PVP ($M_w$=55,000) solution from a single growth potential of -0.5 V for 400 ms along with its corresponding particle size distribution histogram.

## 6.8 Summary

A novel synthetic method coupling electrochemical nucleation and growth of silver at an electrode surface with pulsed ultrasonic assisted dislodgement is described. An initial pulse profile employing separate nucleation and growth potentials failed to produce nanoparticles in solution. At extreme potentials applied for the entire pulse profile, however, the formation of silver nanoparticles was observed.

PVP was employed as a stabilising agent for the prepared silver nanoparticles. Two different molecular weights of PVP were investigated, PVP55 and PVP10, with molecular weights of 55,000 and 10,000 respectively. The addition of PVP greatly influenced the voltammetric behaviour observed with a reduction in the current density of the anodic stripping peak, indicating preferential nanoparticle formation and separation from the electrode over electrodeposition. A shift in the nucleation potential was also observed caused by the increased competition between silver ions and PVP at the electrode surface. Increasing the concentration of PVP55 from 0.2 to 10 g/l further reduced the current density of the anodic peak.

For all the PVP concentrations investigated the UV-Vis spectra showed a broad plasmon band after 1 hour of electrolysis indicating a large size distribution of nanoparticles in solution. Centrifugation of the as-prepared solutions produced a better defined plasmon band, demonstrating the removal of the larger particles.

TEM images of the as-prepared nanoparticles confirmed the results obtained from the UV-Vis spectra showing a dispersion of sizes and shapes. Increasing the PVP55 concentration to 10g/l produced monodisperse spherical nanoparticles and dog-bone shaped nanorods, as well as large dendritic formations. However, any further increase in PVP55 concentration became unfavourable producing only large polydisperse spherical nanoparticles.

The possible formation of gold nanoparticles was also investigated using the technique described in this Chapter. However, no gold nanoparticles were produced in both acid and alkaline media. This is attributed to the high affinity of gold for platinum which means that the ultrasonic pulse is insufficient to dislodge the growing nuclei from the electrode surface.

It should be mentioned that the concentration of particles observed was always small (low absorbance values) but the spectra and TEM results clearly identified the formation of nanoparticles. More work is required to achieve high concentrations of nanoparticles using this technique.

# Chapter 7

# Surface Enhanced Raman Spectroscopy

## 7.1 Introduction

Since its accidental discovery in 1974 [140], the interest in Surface Enhanced Raman Spectroscopy (SERS) has grown considerably. This is mainly due to the many analytical applications of Raman spectroscopy as a powerful technique for the fast characterisation of functional groups. In spite of this, the mechanism by which the enhancement occurs is still unclear and there are still many unanswered questions relating to this phenomenon, for instance, why some metals are better than others as substrates for enhancement and what are the essential properties needed for enhancement to actually occur. One requirement that has been established is the need for a roughened surface. This roughening has been achieved by various techniques such as electrochemical [153, 194], chemical reductions [195, 196], electrodeposition methods [197] and by the addition of metallic colloids of varying morphologies to a surface [198–202]. It is the latter with which we are concerned in this Chapter.

As discussed in Chapter 2, Section 2.2.6, the most commonly accepted the-

ory for enhancement by nanoparticles is a combination of a chemical and an electromagnetic effect, the latter providing the largest contribution. Chemical enhancement is thought to act through the formation of a surface charge-transfer complex [203], whereas electromagnetic enhancement contributes in a far more complex manner. The electric field of the incident laser radiation causes collective oscillations in the conduction electrons of the nanoparticle and these oscillations, or surface plasmons, induce a greatly enhanced electromagnetic field which decays rapidly away from the nanoparticle surface [204].

Due to the origin of this large electromagnetic effect, it is easy to see why factors such as size, morphology, crystallinity, inter-particle distance and choice of metal affect considerably the degree of enhancement achievable. For these reasons, investigations into the optimum conditions needed to provide a large enhancement are proving of great interest. Xu et al. [204] observed a significant Raman scattering enhancement for molecules residing in the inter-spacial region between aggregated colloidal nanoparticles. This was attributed to plasmonic coupling between nanoparticles in close proximity to each other, which results in a very large increase in the electromagnetic field in these confined spaces or SERS 'hot spots'.

Although the use of colloids as SERS substrates is now well established, the study of different morphologies is relatively new. The main reason for the study of nanostructures with differing geometries is their optical properties, which are unique to each particle shape. By changing the shape, the optical properties vary and this leads to the possibility of tuning the properties to a desired application. An example of such a shape is the nanorod which not only exhibits a transversal plasmon band, but also a longitudinal plasmon band, the latter at higher wavelengths. The resulting optical absorbance is highly dependent on the aspect ratio of the nanorods. By tuning the wavelength of this longitudinal band to coincide with the wavelength of the laser employed for Raman excitation, maximum elec-

tromagnetic enhancement can be achieved. Gersten et al. [205] and more recently Zhue et al. [206] observed extremely high local field enhancements produced by 'sharp surface features' such as the tips on needle-like and elliptical nanoparticles. This phenomenon is known as the lightening rod effect.

In this Chapter, the gold nanorods synthesised by the procedure detailed in Section 3.2 were used as a SERS substrate. The enhancement achieved was investigated using 4-mercaptobenzioc acid (MBA) attached to a gold-on-glass surface. Various linker molecules were investigated along with pretreatment methods of the gold-on-glass slides in order to achieve reproducible results. The preparation of the gold nanorod solution employed was described in Section 3.2. For each layer deposited ellipsometry was employed as a characterisation tool in order to establish whether deposition had occurred and where applicable to estimate the film thickness.

## 7.2 Chemicals and Materials

3-mercaptobenzoic acid (MBA, 95%), mercaptoundecanoic acid (MUA, 99%), benzoic acid (99.5%), diaminononame (98%), nonanedithiol (95%) and chloroform ($CHCl_3$, 99.9%) were all purchased from Aldrich. All chemicals were used as received. All experiments were performed on gold-on-glass slides (11 mm $\times$ 11 mm, Arrandee, Germany).

## 7.3 Ellipsometry Measurements

The ellipsometer was calibrated using the supplied silicon wafer. The laser was allowed to warm up for at least 30 minutes prior to taking any measurements. The same analysis procedure was performed for each gold film slide. The measurements were carried out in the pattern described in Figure 7.1. Briefly, 20 measurements

of Delta ($\Delta$) and Psi ($\Psi$) were taken for a pattern of 4 rows with 5 measurements taken on each row. This ensured that a representative sampling of the entire slide was observed. The values of $\Delta$ and $\Psi$ were averaged and these, together with their standard deviations, are reported in this Chapter.

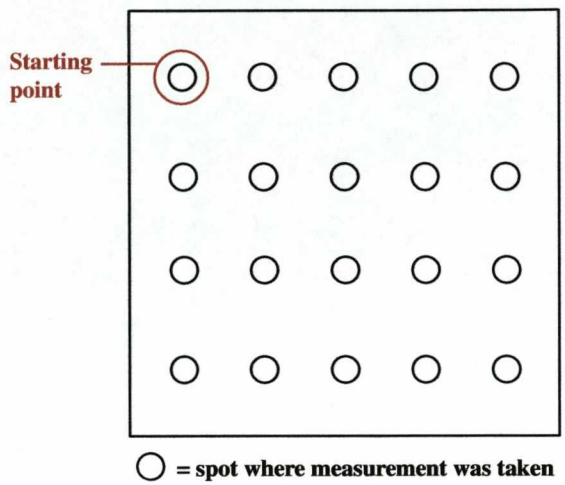


Figure 7.1: Schematic diagram showing the positions where the ellipsometer measurement points were taken on each gold-on-glass slide.

## 7.4 Sample Pre-treatment

The effect of pre-treatment of the gold film slides on their optical properties was investigated. The product specification of the slide is as follows. A layer of chromium (2.5±1.5) nm is deposited on a base of borosilicate glass (thickness 0.7±0.1) mm. This not only acts as an adhesive film for the gold but also provides a uniform surface for the next layer. A layer of gold (250±50) nm is finally deposited on top [207]. The manufacturer recommends that flame annealing is the preferred method of pretreatment since 100 x 100 nm Au(111) terraces can be easily obtained following this procedure. However, it was discovered through AFM and XPS measurements that flame annealing can also allow the chromium underlayer to become visible [208] and this is unfavourable for the present experiments.

Table 7.1 shows the different optical constants measured for the bare gold film slide with no pretreatment and for one that had been flame annealed following the procedure described by the manufacturer.

Table 7.1: Ellipsometry results showing the effects of flame annealing on the optical constants of the gold-on-glass slide

| | Bare Gold on Glass | | | | Flame Annealed | | | |
|---|---|---|---|---|---|---|---|---|
| | Delta | Psi | Ns | Ks | Delta | Psi | Ns | Ks |
| Average | 106.18 | 43.89 | 0.14 | 3.30 | 109.48 | 43.95 | 0.15 | 3.53 |
| Stan Dev | 0.05 | 0.03 | 0.00 | 0.00 | 0.18 | 0.01 | 0.00 | 0.01 |

As can be seen, the optical constants (Ns and Ks) remain relatively unchanged. This is to be expected as flame annealing should mainly alter the topography of the gold layer. However, the $\Delta$ value does differ. There was a noticeable increase from a bare slide to one that had been flame annealed. More interestingly, the standard deviation for the bare slide is lower than that for the flame annealed slide, indicating that the bare slide is more uniform. Since the optical constants remain largely unaffected by the pre-treatment, the consequence of this is minimal. However, for clarity for each set of ellipsometry data, it will be stated whether the slide had undergone any pretreatment or not.

## 7.5 Linker Molecules

### 7.5.1 Diaminononane

The method of sample preparation was essentially the same for each experiment performed with only slight changes, mainly in the immersion period of each deposited layer but for clarity each sample preparation will be explained in detail. In this set of experiments the gold film slides were flame annealed.

Diaminonane (DAN) was employed as a bifunctionalised ligand to construct multi-layers. Although the exact nature of bonding between an amine and a metal surface is still not completely understood, it is known that bonding of amines to gold is preferential at adatom sites [209]. Figure 7.2 shows a schematic diagram of the proposed layer formation employing DAN as a linker molecule.

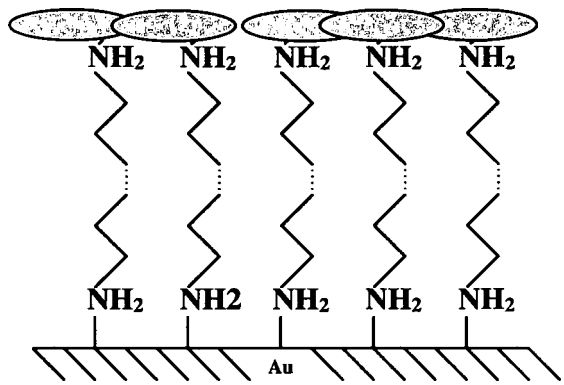


Figure 7.2: Scheme of the DAN/gold nanorod sandwich geometry.

#### 7.5.1.1 Sample Preparation and Results

A gold film slide was immersed for 3 hours into a 5 mL solution of 50 mM diaminononane (DAN) in methanol. The slide was then washed in methanol and dried in a stream of oxygen free argon. The slide was then immersed for 1 hour in a 5 mL solution of the gold nanorod solution synthesised as described in Section 3.2, washed in ultra pure water, dried in argon and then once again immersed in the DAN solution. At each stage ellipsometric data was obtained and the results are shown in Table 7.2.

From an initial value of $\Delta$ of 107.28° for the bare gold slide there is a decrease to 105.75° after the deposition of the first DAN layer. A decrease in $\Delta$ indicates an increase in the thickness of a film on the surface. To determine the thickness of the layer of DAN only the values of $\Delta$ were used. The changes in the values of $\Psi$ were very small and as a consequence, it was found that the commercial software of the

Table 7.2: Ellipsometry data for a gold on glass slide composed of DAN/AuNR/DAN layers

| | Bare Gold on Glass | | | | DAN Layer | | | |
|---|---|---|---|---|---|---|---|---|
| | Delta | Psi | Ns | Ks | Delta | Psi | Ns | Ks |
| Average | 107.28 | 43.93 | 0.14 | 3.39 | 105.75 | 43.88 | 0.14 | 3.28 |
| Stan Dev | 0.06 | 0.02 | 0.00 | 0.01 | 0.18 | 0.03 | 0.00 | 0.01 |
| | Gold Nanorod Layer | | | | DAN Layer | | | |
| | Delta | Psi | Ns | Ks | Delta | Psi | Ns | Ks |
| Average | 105.21 | 43.87 | 0.14 | 3.24 | 105.87 | 43.84 | 0.15 | 3.28 |
| Stan Dev | 1.29 | 0.05 | 0.01 | 0.08 | 0.49 | 0.03 | 0.01 | 0.03 |

instrument was unable to return a value for the thickness. For this reason, the thickness was calculated using a $\Delta$-d simulation obtained from the ELLGRAPH software (Dr R. Greef, Southampton University). This used the refractive index, Nf, of DAN, which was taken as 1.46 [210] and the measured optical constants of the substrate to simulate the dependence of $\Delta$ on layer thickness. Results of this simulation are shown in Figure 7.3. A linear dependence is observed with a calculated gradient $\delta\Delta/\delta$d = -1.08° $\AA^{-1}$. From the measured change in the value of $\Delta$ a thickness of the DAN layer of 14.2Å could be estimated. This is close to the calculated value of 12.5Å obtained through an ab initio calculation employing a Hartree-Fock/3-21G approximation (Spartan Pro, Wavefunction, Inc.)

This -$NH_2$- terminated slide was then immersed in the gold nanorods solution for 1 hour in the expectation of attaching a layer of nanorods. However, only a very slight decrease in the value of $\Delta$ was observed indicating only a very slight change in thickness. The average size of the gold nanorods used, measured by TEM ( Figure 3.6), was (54±11) nm by (21±11) nm and therefore, the expected change in $\Delta$, even for a SAM where the nanorods are ordered into a planar orientation to the surface, should have been much larger than the value measured. When the

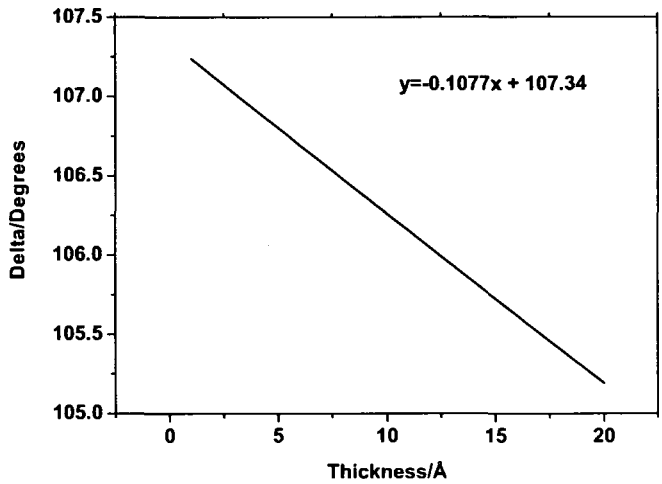


Figure 7.3: Calculated dependence of $\Delta$ on layer thickness of DAN adsorbed on gold.

slide was immersed in the DAN solution once more, the measured $\Delta$ value actually increased, indicating a decrease in the overall thickness. This is a surprising result since further attachment of the bifunctional ligand would have been expected.

It is proposed that immersing the slide in the DAN solution results in the dissolution of the previous weakly bound gold nanorod layer as the $\Delta$ values for the second DAN layer are almost identical to those obtained for the initial layer. There is also a marked increase in the standard deviation of $\Delta$ after immersion in the gold nanorod solution, indicating that the coverage by nanorods is not uniform. To further investigate this, the same slide was re-immersed in the DAN solution for 18 hours to detect possible slow reactions on the film and the results are shown in Table 7.3. As before, the value of $\Delta$ increased slightly after further exposure to DAN.

This effect of the ligand could be a attributed to the high concentration solution (50 mM) used. To examine this effect, a lesser concentrated solution (2 mM) was employed without altering any of the other experimental conditions. In this

Table 7.3: Ellipsometer results after immersion in DAN solution for 18 hours

| | DAN - 18 hours | | | |
|---|---|---|---|---|
| | Delta | Psi | Ns | Ks |
| Average | 106.05 | 43.87 | 0.15 | 3.30 |
| Stan Dev | 0.29 | 0.02 | 0.00 | 0.02 |

experiment, the gold film slide was flame annealed.

The ellipsometry results for this experiment are shown in Table 7.4. The main effect of lowering the DAN concentration is that the thickness of the initial DAN layer is considerably lower compared to that of the 50mM solution originally employed, with a calculated average thickness of 7.9Å. However, the standard deviation for both sets of results is ~0.17Å. If the lowering in film thickness was simply associated with irregularities of the packing of the DAN molecules on the slide then a large standard deviation would be expected and this is not the case.

The lowering in film thickness could be attributed to the orientation of the DAN molecule on the gold surface. For bifunctional molecules such as dithiols, the surface concentration significantly affects the structure of the SAM formed [211]. It has been proposed that alkyl dithiol molecules bind to the gold surface in two stages. Initially, they bond in a 'lying down' position, where the alkyl chains molecules lie flat on the gold surface. With increasing coverage, the interactions between adsorbed molecules increases and at some point the alkyl chains lift off the substrate and point outwards, tethered to the surface by the thiol anchor. Both the immersion time and solution concentration influence the degree of each type of bonding on the surface [212]. Therefore, using a highly concentrated solution should result in the formation of a densely packed SAM orientated perpendicular to the surface, with the possibility of multilayer formation, whereas solutions of low concentration should initially adopt a flat orientation leading to a lower

observed layer thickness.

Table 7.4: Ellipsometry data for a gold on glass slide composed of DAN/AuNR/DAN using a 2 mM DAN solution

| | Bare Gold on Glass | | | | DAN Layer | | | |
|---|---|---|---|---|---|---|---|---|
| | Delta | Psi | Ns | Ks | Delta | Psi | Ns | Ks |
| Average | 109.48 | 43.95 | 0.15 | 3.53 | 108.62 | 43.79 | 0.17 | 3.47 |
| Stan Dev | 0.18 | 0.01 | 0.00 | 0.01 | 0.17 | 0.02 | 0.01 | 0.01 |
| | Gold Nanorod Layer | | | | DAN Layer | | | |
| | Delta | Psi | Ns | Ks | Delta | Psi | Ns | Ks |
| Average | 107.40 | 43.82 | 0.16 | 3.38 | 108.20 | 43.82 | 0.16 | 3.436 |
| Stan Dev | 0.22 | 0.01 | 0.00 | 0.02 | 0.16 | 0.02 | 0.00 | 0.01 |

After immersion in the gold nanorod solution, a slight decrease of $\Delta$ was observed, but upon immersion back in the 2 mM DAN solution for a further hour, an increase in the value of $\Delta$ was noted, the same trend observed when the higher concentrated DAN solution was employed. This indicates that the gold nanorods are easily displaced by re-immersion in even a dilute DAN solution and therefore, a stronger linker molecule to support the gold nanorod layer was required. For this reason, a dithiol was employed as the ligand.

### 7.5.2 Nonanedithiol

Due to the high affinity of sulphur to gold to form a strong covalent bond not only should nonanedithiol (NDT) provide a greater uniformity for the initial layer but also result in a better coverage of the gold nanorod layer. The proposed structure of the layer formed is shown in Figure 7.4.

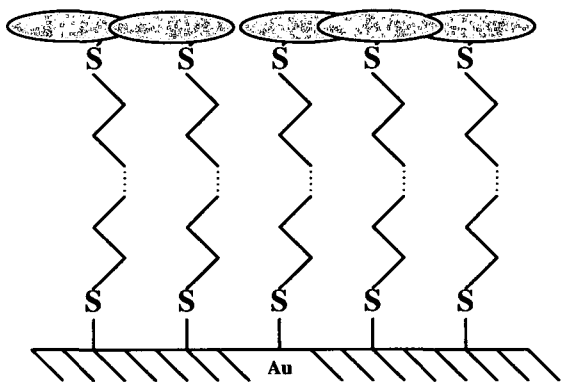


Figure 7.4: Scheme of the NDT/gold nanorod sandwhich geometry.

#### 7.5.2.1 Sample Preparation and Results

A gold film slide was immersed for 3 hours into a 5 mL solution of 50 mM nonanedithiol (NDT) in methanol. The slide was then washed with methanol and dried in a stream of oxygen free argon. The slide was then immersed in a 5 mL solution of the gold nanorod solution for 1hr, washed in ultra pure water, dried in argon and then once again immersed in the NDT solution. This was repeated for forming up to 13 bi-layers of NDT and gold nanorods. Ellipsometric data was obtained at each stage of film growth. The results for the first NDT layer are shown in Table 7.5.

Table 7.5: Ellipsometer results from the first layer of NDT on a bare gold film slide.

| | Bare Gold on Glass | | | | First NDT Layer | | | |
|---|---|---|---|---|---|---|---|---|
| | Delta | Psi | Ns | Ks | Delta | Psi | Ns | Ks |
| Average | 109.99 | 43.99 | 0.14 | 3.56 | 108.65 | 43.84 | 0.16 | 3.47 |
| Stan Dev | 0.31 | 0.06 | 0.01 | 0.02 | 0.14 | 0.06 | 0.01 | 0.01 |

Employing the same technique as for diaminonane, the thickness of the first layer was estimated through a computer simulation of the dependence of $\Delta$ on

thickness. The refractive index of NDT was taken to be the same as that of nonane, which is 1.46 [210]. The calculated gradient $\delta\Delta/\delta$d taken from Figure 7.5 was -1.10° $\AA^{-1}$. This results in an estimated thickness of 12.1Å for the initial NDT layer. This is close to the calculated value of 13.1Å obtained through an ab initio calculation employing a Hartree-Fock/3-21G approximation (Spartan Pro, Wavefunction Inc.)

The slight difference between the results in Figure 7.3 and 7.5 is due to the difference in the optical properties of the substrate; as expected, the slope for the two is very similar.

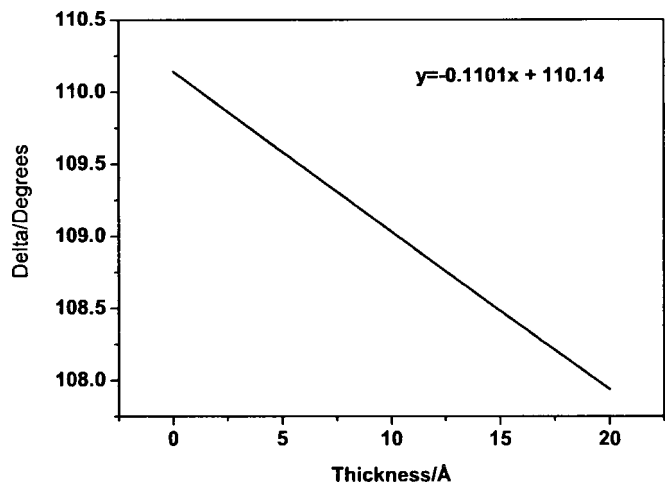


Figure 7.5: The simulated effect of the change in layer thickness on the associated delta values of NDT.

After immersion in the gold nanorod solution for 1 hour a slight decrease in the value of $\Delta$, from 108.65° to 108.01°, was observed indicating a slight increase in thickness. The data from the subsequent 25 layers is displayed in Figure 7.6. A large number of layers were deposited in the expectation of obtaining a constant and stable background in terms of the optical constants of the film, i.e, the surface became homogeneous. It was considered that the effects resulting from

additional gold layers would be independent of the number of layers since the optical properties of the substrate would not change as linker and nanorod layers were added.

It was expected that multilayer formation would also lead to a highly disordered topography which would emulate the roughened surface needed for SERS. However, the experimental results proved that this was not the case. Although all the measured parameters followed the correct trends to conclude that additional layers were being deposited, no constancy in the optical properties was reached indicating that the surface is highly heterogeneous, that is each layer is still well defined based on the ellipsometric data.

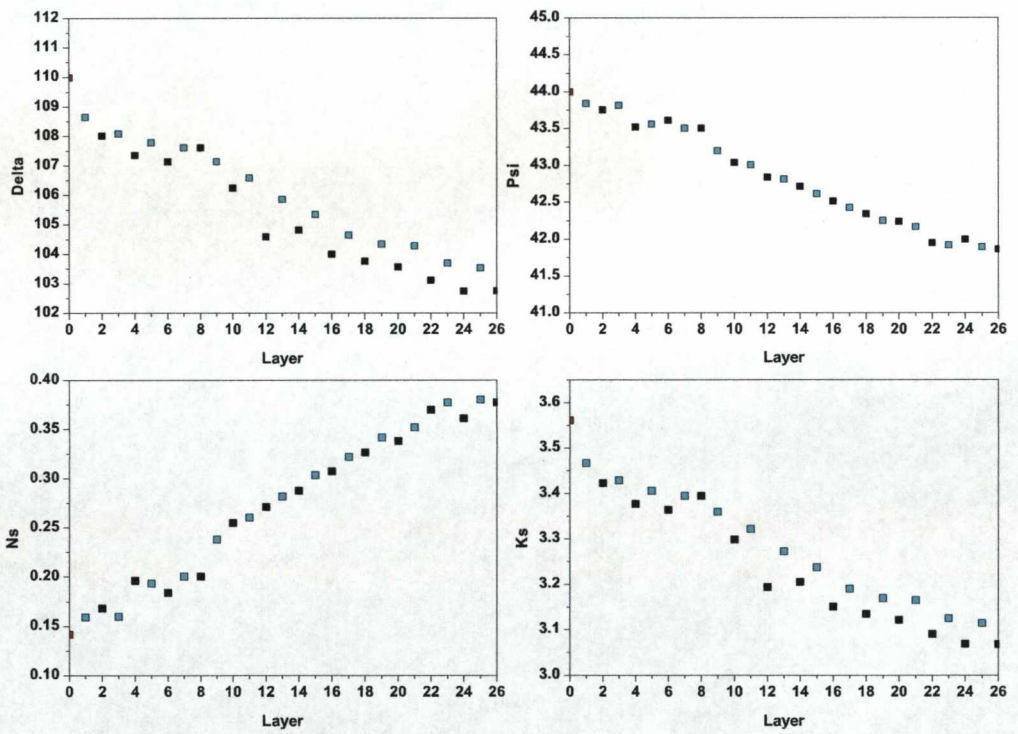


Figure 7.6: Ellipsometric data for multilayer formation of NDT and gold nanorods. Red = gold-on-glass slide, blue = NDT layer and black = AuNR layer

Although the general trend in the data obtained from ellipsometry for NDT was as expected for layer growth, some anomalous results could be observed e.g,

increases in the values of $\Delta$ for additional layers of NDT when an actual decrease should have been observed. In order to ascertain if washing alone after the slide had been immersed was sufficient to remove any unbound material, a chloroform cleaning procedure was tested. Briefly, after each new layer was added, the slide was rinsed in the same solvent used to deposit the layer, the average values of $\Delta$ and $\Psi$ were measured and the slide was then cleaned by immersing it in the vapour of boiling chloroform in a beaker. This ensures the condensation of pure hot chloroform on the slide. The solvent on the slide was allowed to evaporate and this procedure was repeated three times and the slide was then allowed to cool. Finally, the slide was washed once more in the initial solvent and $\Delta$ and $\Psi$ were then measured again. Although the results from this cleaning method showed that this step was successful at removing some of the anomalous results others still remained. Therefore, the results proved overall inconclusive and further investigation is needed.

Due to the inconsistencies observed in the attempted covalent attachment of nanorods to a gold substrate it was clear that this approach proved unsuccessful. Therefore, a new approach using electrostatic interactions for attaching the nanorods to the gold surface was employed, as described in the next Section.

# 7.6 Electrostatic Layer Deposition

## 7.6.1 Introduction

Electrostatic interaction was investigated as a possible route for the deposition of SERS active molecules onto a layer of electrostatically bound gold nanorods. As previously discussed in Chapter 1, Section 1.2.2 the surface composition of CTAB stabilised gold nanorods consists of a bi-layer structure which is known to have a net positive charge, comfirmed by both electrophoresis [213] and zeta potential measurements [214]. On this basis, the electrostatic sandwich structure shown in Figure 7.7 is proposed for use as a SERS substrate.

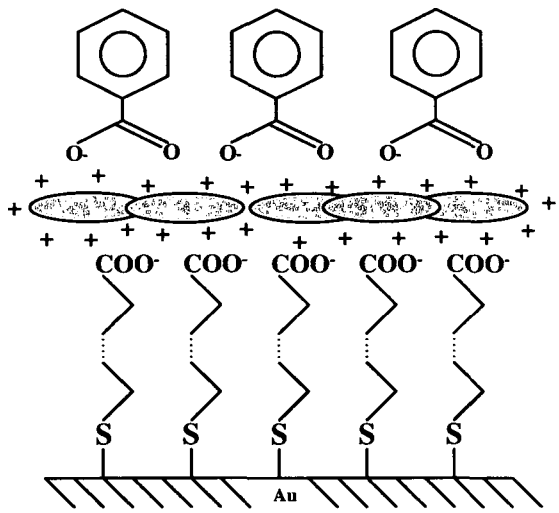


Figure 7.7: Scheme showing the proposed electrostatic route for the formation of a surface suitable for SERS.

## 7.6.2 Preparation of Multilayer Structures

An initial linker molecule SAM was first deposited onto a bare gold film slide. The linker was a bifunctional alkane containing a thiol and a carboxylate group at each end of the molecule, respectively. The gold nanorods were bound to this $-COO^-$ terminated layer by strong electrostatic attraction as shown in Figure 7.7. Onto

this gold nanorod layer, which should still carry a net positive charge, benzoic acid in its ionised form was attached. The enhancement associated with the gold nanorods should provide an excellent surface for SERS. The success of this approach relies, however, on the appropriate selection of experimental conditions. The initial linker SAM produced should have a net negative charge in order for the positively charged gold nanorods to bind. Therefore, the pH of the nanorod solution had to be adjusted so that it was greater than the pKa of the terminal -COOH group of the linker molecule to ensure total ionisation.

To investigate whether the nanorods synthesised were actually capable of producing a SERS effect, a simple experiment was preformed following the method outlined by Orendorffa et al. [215]. Briefly, a gold film slide was immersed into a 1 mM ethanoic solution of 4-mercaptobenzoic acid for 72 hours to ensure full coverage by 4-MBA, then rinsed thoroughly with ethanol and dried in argon. The gold nanorods were then immobilised onto the 4-MBA SAM by immersing the slide for three hours into a 5 mL solution of the as-prepared gold nanorods. In this case, the SERS active molecule acts as the linker molecule. The pH of the nanorod solution was 5.4 to be compared with the pKa of 4-MBA of 5.8 [216]. Therefore, for the nanorods to bind electrostatically to MBA, the pH of the solution had to be adjusted so that it was greater than 5.8 to ensure ionisation of the carboxylate group. The net positive charge of the nanorods is pH independent within the pH range employed [214] and is therefore unaffected by the change in solution pH. Figure 7.8 shows schematically the structure of this proposed sandwich geometry used for acquiring the SERS spectra of 4-MBA.

The Raman spectra of solid 4-MBA is shown in Figure 7.9 and the corresponding peak frequency assignments are given in Table 7.6. The characteristic vibrational modes at $\sim$1100 $cm^{-1}$ and $\sim$1600 $cm^{-1}$ corresponding to the aromatic ring breathing modes are clearly visible [215]. Since these two peaks are the most predominant, these were used as an indication of SERS enhancement. Other less

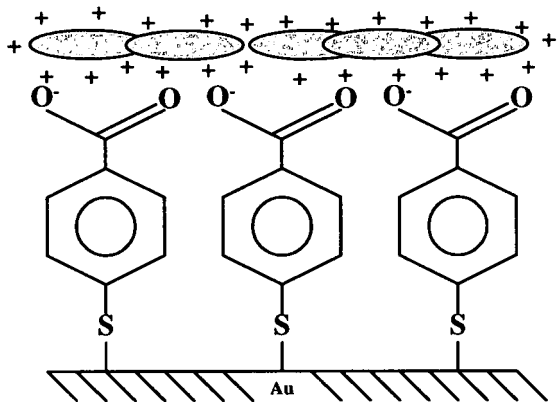


Figure 7.8: Scheme showing the proposed electrostatic sandwich geometry for SERS of 4-MBA.

predominant bands including the $\delta$(CH) at ~1190 cm$^{-1}$, the $\nu_s$(COO$^-$) at ~1400 cm$^{-1}$ and the $\nu$(SH) at ~2560 cm$^{-1}$ are also observed. The presence of the thiol stretching band is important as its presence or absence is a good indication of the mode of bonding of 4-MBA. The acquisition time for all the Raman experiments was 240 seconds, performed in eight 30 second blocks, which were averaged to obtain the spectra.

The orientation of the molecule with respect to the surface can also be determined from the SERS spectra . For example, the presence of a band at ~720 cm$^{-1}$ which is assigned to the out of phase $\gamma$(CCC) vibration mode of the aromatic ring, would indicate that the 4-MBA molecule is orientated parallel to the surface [217]. The absence of this band is an indicator of a perpendicular orientation of the 4-MBA on the surface. This is further supported by the corresponding absence of the carboxyl modes at ~1700 cm$^{-1}$ [63].

Figure 7.10 shows the SERS spectra obtained from the structure proposed in Figure 7.8. After the initial layer of 4-MBA was deposited, Figure 7.10 (a), no signal is observed from either of the aromatic ring-breathing modes. However, after the same slide was immersed into the gold nanorod solution adjusted to a pH of 7.5 by the addition of dilute NaOH, Figure 7.10 (b), a very large increase

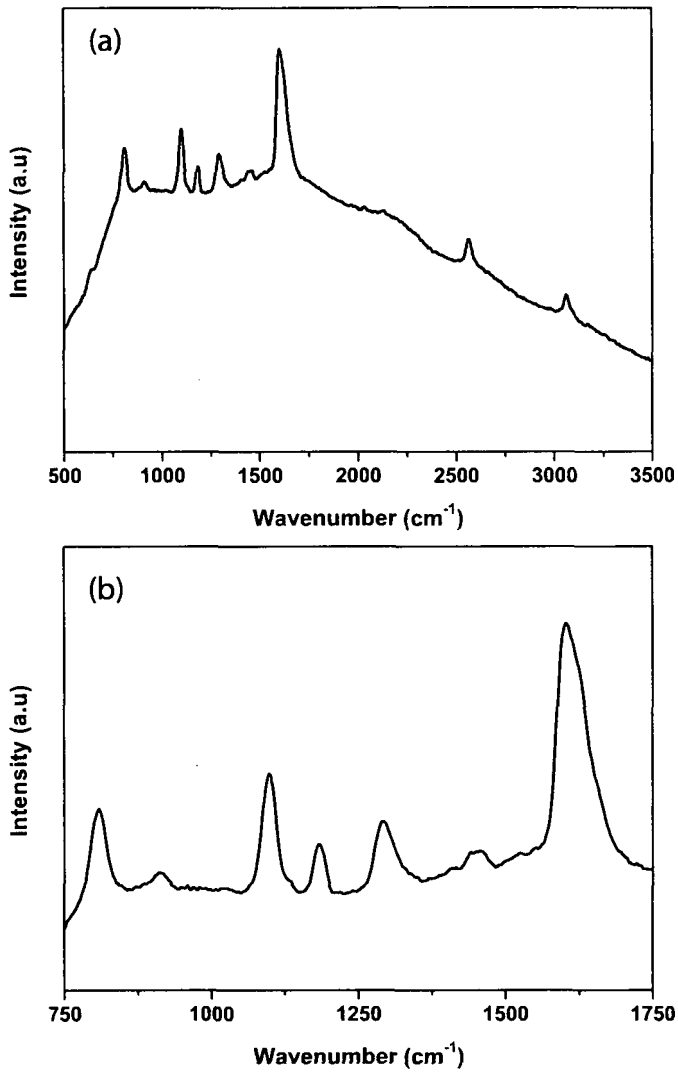


Figure 7.9: Raman spectra of solid 4-MBA. (a) overall spectra and (b) detail of the region between 750 $cm^{-1}$ and 1750 $cm^{-1}$.

in signal was observed. Two bands are clearly visible, along with a number of less predominant bands observed in the Raman spectrum of solid 4-MBA. From these results, it is clear that great enhancement is observed by the deposition of a layer of gold nanorods. The distinct lack of any enhancement of the band at ~2560 $cm^{-1}$ in Figure 7.10 (b) assigned to the stretching mode of the thiol indicates that indeed the 4-MBA is bound to the gold by this thiol group [66].

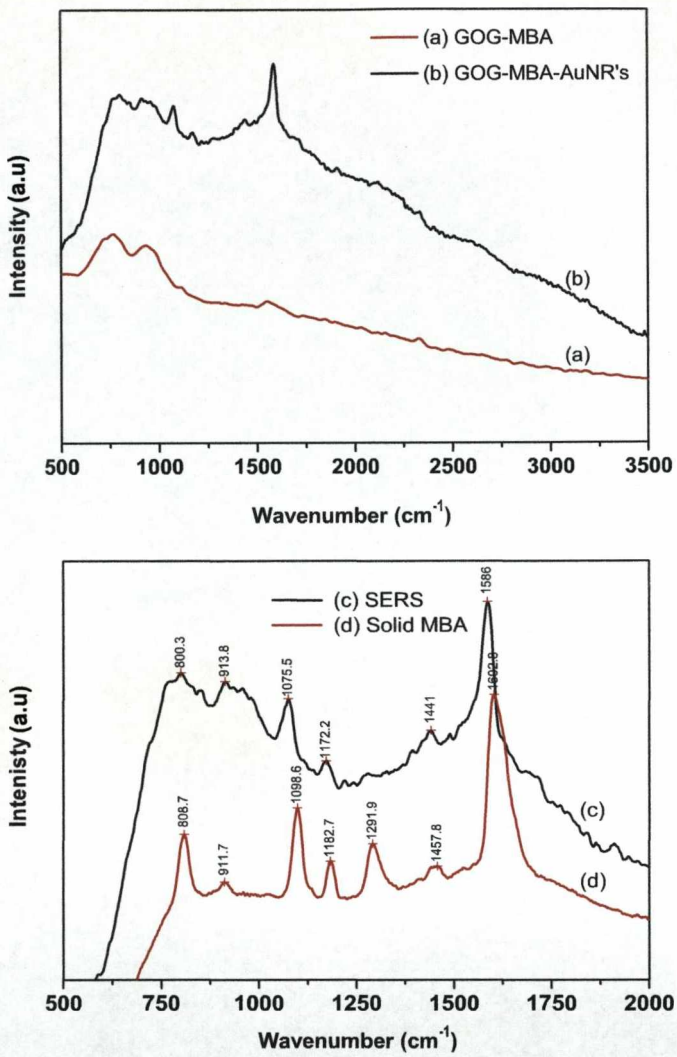


Figure 7.10: (a) Raman spectra of a SAM of 4-MBA on a gold film slide, (b) SERS spectra of the sandwich geometry shown in Figure 7.8, (c) SERS spectra of (b) in closer detail and (d) Raman spectra of solid 4-MBA.

The slide took a uniform dark brown colour and had a redish tint on reflection indicating that nanorod deposition had occurred. This had not been observed in the previous experiments discussed above. A comparison of the bands observed for solid 4-MBA and in the SERS spectra in Figure 7.10 (b) is shown in spectra (c) and (d). All the bands present in the Raman spectrum of solid 4-MBA are also present in the SERS spectrum measured, with the exception of the aromatic ring

Table 7.6: Peak frequency assignments for solid 4-MBA

| Peak frequency ($cm^{-1}$) | Assignment |
|---|---|
| 808 | possible $\delta(COO^-)$ [218] |
| 911 | $\beta$(SH) [63] |
| 1099 | $\nu_{12}$ Aromatic Ring Vibration [63,66,218] |
| 1184 | $\delta$(CH) [215] |
| 1292 | Aromatic Ring Stretch [63] |
| 1450 | $\nu_s(COO^-)$ (*Non H-bonded*) [63] |
| 1603 | $\nu_{8A}$ Aromatic Ring Vibration [63,66,218] |
| 2564 | $\nu$(SH) [63] |
| 3059 | Aromatic $\nu$(CH) Stretch [218] |

stretch modes at ~1290 $cm^{-1}$ and ~3060 $cm^{-1}$. Michota et al. [63] and Talley et al. [66] reported the same observation. The relative intensities of these CH stretching bands gives an indication of the orientation of the molecule with respect to the surface. Talley et al. suggested that the disappearance of these bands once immobilisation had occurred, indicates that the 4-MBA molecule probably adopts a tilted orientation with respect to the metal surface. A shift in the peak positions of the SERS spectra to higher wavenumbers is also observed indicating that the 4-MBA molecules are bonded to the surface.

## 7.7 SERS pH Dependence Experiments

To investigate the electrostatic deposition of gold nanorods on a gold film, a series of five solutions at different pH values were examined. Extreme pH's (<3 and >11) have been observed to induce aggregation and precipitation of metallic nanostructures [219] and therefore, a pH range within these values was chosen. Mercaptoundecanoic acid (MUA) was employed as the linker between the gold

film surface and the gold nanorods.

### 7.7.1 Sample Preparation and Results

A gold film slide, used as-received, was immersed for 24 hours in a 5 mL ethanol solution of 1 mM MUA. In preliminary experiments, a 10 mM solution was employed and the immersion time lowered to 3 hours but this produced a surface which displayed a large standard deviation in ellipsometric thickness. This was also supported by the patchy nature of the slides appearance after nanorod deposition. By lowering the concentration and increasing the immersion time, a far more uniform SAM was obtained and this was reflected in the ellipsometry data measured. The slide was then rinsed with ethanol, dried in a stream of argon and then immersed in 5 mL of a pH adjusted gold nanorod solution for 2 hours. The pH of the nanorod solution was controlled by the addition of dilute HCl or NaOH. The slide was then rinsed with ultra pure water and dried once again in argon. The deposited layers were monitored using ellipsometry.

Table 7.7 shows the ellipsometry data obtained after the addition of each layer for each pH investigated. For each addition of the MUA SAM, a decrease in the value of $\Delta$ is observed. The results for benzoic acid will be discussed later on. Due to MUA's structural similarity with NDT it was assumed that the refractive index is also similar. Therefore, the calculated gradient taken from Figure 7.5 for NDT was used to estimate the average thickness of the MUA SAM. The average value obtained for all five pH's is (16±4) Å. Although the estimated thickness is close to the value of 16.2Å, calculated through an ab initio calculation employing a Hartree-Fock/3-21G approximation, the standard deviation is quite large. For each pH, an extremely large decrease in the values of $\Delta$ and a corresponding change in the optical constants is observed for each gold nanorod layer attached. This change in the value of $\Delta$ follows a linear negative trend with a larger decrease occurring as the pH is increased, which implies that there is an increase in layer

Table 7.7: Ellipsometric data for layer structure MUA/Au Nanorods/Benzoic Acid at different pH's.

**pH 6.6**

| | Bare Gold on Glass | | | | MUA | | | |
|---|---|---|---|---|---|---|---|---|
| | Delta | Psi | Ns | Ks | Delta | Psi | Ns | Ks |
| Average | 105.70 | 43.92 | 0.14 | 3.27 | 104.07 | 43.82 | 0.15 | 3.17 |
| Stan Dev | 0.09 | 0.02 | 0.00 | 0.01 | 0.16 | 0.02 | 0.00 | 0.01 |
| | Gold Nanorod Layer | | | | Benzoic Acid | | | |
| | Delta | Psi | Ns | Ks | Delta | Psi | Ns | Ks |
| Average | 84.58 | 38.78 | 0.55 | 2.11 | 84.32 | 38.65 | 0.56 | 2.10 |
| Stan Dev | 1.93 | 0.54 | 0.04 | 0.09 | 1.46 | 0.51 | 0.04 | 0.07 |

**pH 7.6**

| | Bare Gold on Glass | | | | MUA | | | |
|---|---|---|---|---|---|---|---|---|
| | Delta | Psi | Ns | Ks | Delta | Psi | Ns | Ks |
| Average | 106.02 | 43.96 | 0.13 | 3.29 | 103.82 | 43.69 | 0.16 | 3.15 |
| Stan Dev | 0.14 | 0.05 | 0.01 | 0.01 | 0.26 | 0.07 | 0.01 | 0.02 |
| | Gold Nanorod Layer | | | | Benzoic Acid | | | |
| | Delta | Psi | Ns | Ks | Delta | Psi | Ns | Ks |
| Average | 80.31 | 38.32 | 0.57 | 1.92 | 80.99 | 38.64 | 0.57 | 1.96 |
| Stan Dev | 1.05 | 0.19 | 0.01 | 0.04 | 1.69 | 0.46 | 0.02 | 0.07 |

**pH 8.5**

| | Bare Gold on Glass | | | | MUA | | | |
|---|---|---|---|---|---|---|---|---|
| | Delta | Psi | Ns | Ks | Delta | Psi | Ns | Ks |
| Average | 105.57 | 43.90 | 0.14 | 3.26 | 103.74 | 43.84 | 0.14 | 3.15 |
| Stan Dev | 0.08 | 0.02 | 0.00 | 0.01 | 0.55 | 0.03 | 0.01 | 0.03 |
| | Gold Nanorod Layer | | | | Benzoic Acid | | | |
| | Delta | Psi | Ns | Ks | Delta | Psi | Ns | Ks |
| Average | 74.54 | 37.86 | 0.57 | 1.69 | 75.11 | 37.77 | 0.58 | 1.71 |
| Stan Dev | 0.62 | 0.16 | 0.01 | 0.02 | 1.85 | 0.27 | 0.02 | 0.08 |

**pH 9.6**

| | Bare Gold on Glass | | | | MUA | | | |
|---|---|---|---|---|---|---|---|---|
| | Delta | Psi | Ns | Ks | Delta | Psi | Ns | Ks |
| Average | 105.72 | 43.93 | 0.14 | 3.27 | 104.52 | 43.76 | 0.16 | 3.20 |
| Stan Dev | 0.45 | 0.04 | 0.01 | 0.03 | 0.26 | 0.03 | 0.00 | 0.02 |
| | Gold Nanorod Layer | | | | Benzoic Acid | | | |
| | Delta | Psi | Ns | Ks | Delta | Psi | Ns | Ks |
| Average | 69.38 | 36.86 | 0.63 | 1.49 | 69.89 | 36.71 | 0.64 | 1.51 |
| Stan Dev | 0.31 | 0.21 | 0.02 | 0.01 | 1.08 | 0.32 | 0.02 | 0.04 |

thickness as the pH increases. This can be observed more clearly in Figure 7.11. The pH at which these experiments were conducted were selected considering the acid-base equilibrium:

$$HA \rightleftharpoons H^+ + A^- \tag{7.1}$$

The pKa is related to the ratio of HA to $A^-$ by:

$$pKa = pH + \log \frac{[HA]}{[A^-]} \tag{7.2}$$

When pKa = pH, [HA] = [$A^-$] and equal amount of both forms exist. The pH of 1 mM MUA in water is calculated to be 4.75 and its pKa is 6.5 [220]. Therefore, in aqueous solutions, MUA exists almost completely in its protonated form. Ionisation will be even less extensive in an ethanol solution due to the lower dielectric permittivity of the solvent. When the MUA SAM is placed in contact with the aqueous nanorod solution, the degree of ionisation of the SAM depends on the pH of the nanorod solution.

Table 7.8: Ellipsometric data for layer structure MUA/Au Nanorods/Benzoic Acid at pH 4.5.

| | **pH 4.5** | | | | | | | |
|---|---|---|---|---|---|---|---|---|
| | Bare Gold on Glass | | | | MUA | | | |
| | Delta | Psi | Ns | Ks | Delta | Psi | Ns | Ks |
| Average | 105.72 | 43.91 | 0.14 | 3.27 | 104.61 | 43.76 | 0.16 | 3.20 |
| Stan Dev | 0.13 | 0.02 | 0.00 | 0.01 | 0.12 | 0.03 | 0.00 | 0.01 |
| | Gold Nanorod Layer | | | | Benzoic Acid | | | |
| | Delta | Psi | Ns | Ks | Delta | Psi | Ns | Ks |
| Average | 103.88 | 42.77 | 0.28 | 3.15 | 103.38 | 42.60 | 0.29 | 3.12 |
| Stan Dev | 0.56 | 0.22 | 0.02 | 0.04 | 0.60 | 0.32 | 0.04 | 0.04 |

The results in Figure 7.11 also shows that at pH 4.5 no nanorod deposition occurs since only a very slight decrease in the value of $\Delta$ after immersion in the gold nanorod solution, 103.9°, is observed compared to that of the bare gold film slide, 105.7°. This is due to the fact that at this pH the protonated form of MUA

dominates. The ellipsometric data obtained for this pH is shown in Table 7.8.

Once the pH is increased above the pKa of MUA nanorod attachment is observed. Since total deprotonation should occur at pH 7, increasing the pH should have little effect on the thickness of the gold nanorod layer in terms of the electrostatic attraction between the negatively charged MUA and the positively charged nanorods. The present results indicate, however, that this is not the case. As the pH is increased a noticeable change in the thickness is observed. Such a large decrease in the value of $\Delta$ indicates that multilayer deposition takes place under these conditions. From TEM images of the gold nanorods (Figure 3.6) the average nanorod height was (21±11) nm. If it as assumed that the nanorods bind

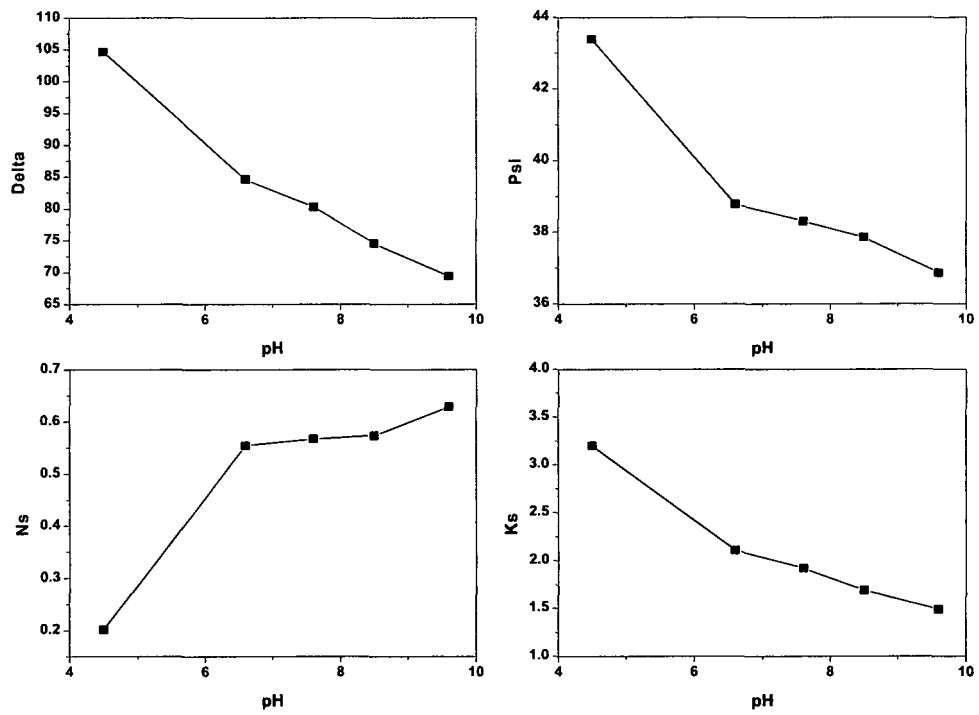


Figure 7.11: Ellipsometric data of the gold nanorod layer taken from Table 7.7.

parallel to the surface forming a monolayer, then the associated change in the

value of $\Delta$ should be far less. It is possible that the nanorods are bound in a close packed structure perpendicular to the surface. However, due to the decreased packing of the CTAB molecules at the ends of the nanorods this would be thermodynamically unfavorable. The stability of a multilayer would also be low due to the repulsive electrostatic interactions between two or more layers of positively charged nanorods. As a consequence, washing the slides after deposition should be sufficient to remove any unbound nanorods. Once again the appearance of the slide indicated nanorod attachment with each slide turning dull brown. Gole et al. [219] observed an optimum pH of 6.5 for the electrostatic immobilisation of gold nanorods on a SAM of 16-mercaptohexadecanoic acid (MHA). At higher pH's, extreme aggregation was observed by SEM, with the nanorods completely precipitating out of solution at pH >10. Although immobilisation was observed in the present work at pH 9.6, the stability of the nanorod solution was severely affected and precipitation occurred after 1-2 hours. The optimum pH calculated by Gole is based solely upon the dispersion of the nanorods on the MHA SAM and the use of the substrate for SERS was not considered.

To investigate if the scheme proposed in Figure 7.7 would produce a SERS enhancement, each slide was immersed into a 10 mM methanol solution of benzoic acid for 2 hours. The pH of this solution was adjusted to 7.5 to ensure ionisation of the carboxylate group, therefore allowing electrostatic binding to the gold nanorods. The ellipsometry data for this experiment is shown in Table 7.7. After 2 hours no change in the measured values of $\Delta$ and $\Psi$ was observed indicating that no benzoic acid was bound. This was corroborated by the lack of any SERS signal from the slide. No enhancement was observed even when the immersion time was increased to 24 hours. It is possible that the net positive charge of the nanorods is being lost when the slide is dried after it has been immersed [44].

In the previous work presented in this Chapter, 4-mercaptobenzoic acid (4-MBA) was directly bound to the gold on glass slide and Raman enhancement

was achieved by the electrostatic immobilisation of gold nanorods to the 4-MBA. To ascertain whether direct attachment of a Raman active molecule to the gold nanorods was possible, 4-MBA was again investigated. The same 10 mM concentration of benzoic acid was employed but the choice of solvent was changed from methanol to toluene, due to its better wetting properties.

Briefly, a gold on glass slide was immersed into 5 mL of a 1 mM ethanol solution of MUA for 24 hours, rinsed in ethanol, dried with argon and the slide was then immersed into 5 mL of the gold nanorod solution adjusted to pH 7.5. The slide was then rinsed with ultra pure water, dried in argon and then immersed into the 10 mM 4-MBA solution in toluene for 1 hour. Figure 7.12 (a) shows the Raman spectra of the gold nanorods immobilised onto the MUA SAM and (b) the SERS spectra from 4-MBA. The ellipsometry results for the layers presented in Figure 7.12 (b) are shown in Table 7.9.

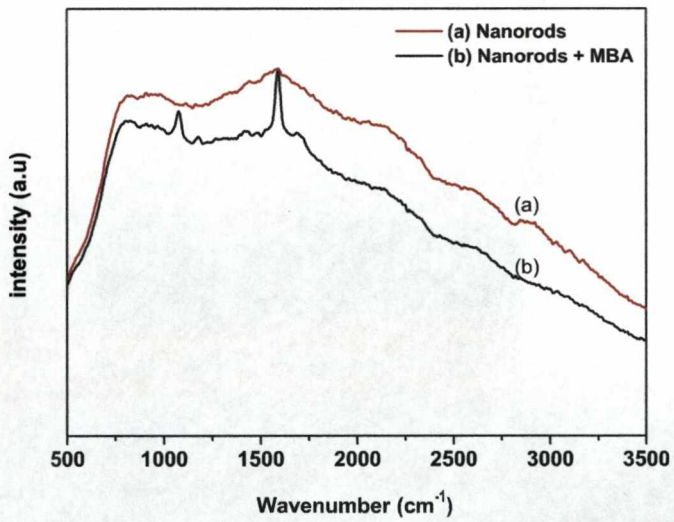


Figure 7.12: (a) Raman spectra of the MUA/gold nanorod geometry and (b) SERS spectra of 4-MBA immobilised onto the gold nanorods.

It is clear that after immersion in the 4-MBA solution Raman enhancement is observed as the two aromatic ring vibrations, along with the much weaker $\gamma$(CH) band at 1171 $cm^{-1}$ become clearly visible. The presence of two weak

Table 7.9: Ellipsometry data for a gold on glass slide composed of MUA/AuNR/MBA from Figure 7.12.

| | Bare Gold on Glass | | | | MUA Layer | | | |
|---|---|---|---|---|---|---|---|---|
| | Delta | Psi | Ns | Ks | Delta | Psi | Ns | Ks |
| Average | 105.960 | 43.889 | 0.143 | 3.289 | 104.414 | 43.758 | 0.155 | 3.190 |
| Stan Dev | 0.098 | 0.033 | 0.004 | 0.006 | 0.101 | 0.031 | 0.004 | 0.006 |
| | Gold Nanorod Layer | | | | 4-MBA Layer | | | |
| | Delta | Psi | Ns | Ks | Delta | Psi | Ns | Ks |
| Average | 85.142 | 38.693 | 0.566 | 2.132 | 84.597 | 38.886 | 0.546 | 2.111 |
| Stan Dev | 0.528 | 0.178 | 0.014 | 0.024 | 0.599 | 0.164 | 0.012 | 0.027 |

bands at ~1450 $cm^{-1}$ and ~1700 $cm^{-1}$, corresponding to the $\nu_s(COO^-)$ and $\nu(C{=}O)$, respectively, indicates that MBA is not bound by the carboxylate group and therefore must be bound by the thiol. This is supported by the absence of the $\nu(SH)$ band at ~2560 $cm^{-1}$. As a control experiment, benzoic acid dissolved in toluene was examined to see whether the SERS enhancement observed was a solvent effect resulting from the use of toluene instead of methanol. The same procedure was followed but this time the slide was first immersed in 10 mM benzoic acid in toluene and the Raman spectra measured. The same slide was then immersed in 10 mM 4-MBA in toluene and once again the Raman spectra measured.

Figure 7.13 (a) shows the Raman spectra of the immobilised gold nanorods. Following immersion in the benzoic acid solution, no enhancement was observed, Figure 7.13 (b). However, when the same slide was immersed in the 4-MBA solution, the characteristic aromatic ring vibration bands appeared, Figure 7.13 (c). This confirms that the MBA indeed bonds to the gold nanorods by the thiol group and that the high intensity of the SERS signal observed is not just the result of the use of toluene as the solvent. The sandwich film structure corresponding to

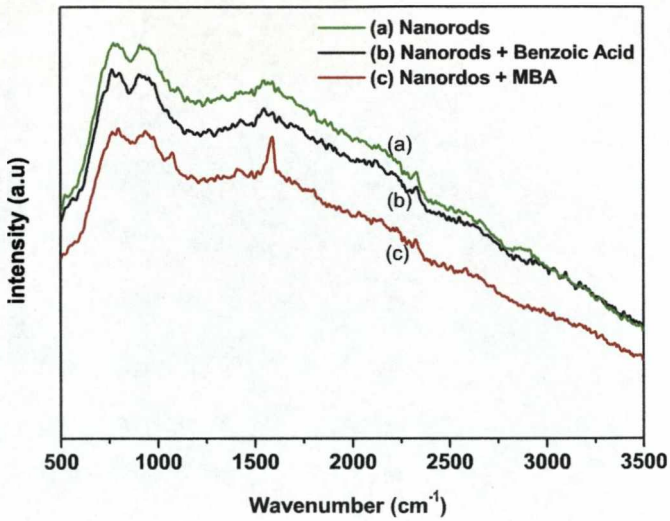


Figure 7.13: (a) Raman spectra of the MUA/gold nanorods, (b) SERS spectra of Benzoic Acid and (c) SERS spectra of 4-MBA immobilised onto the gold nanorods.

the results shown in Figure 7.13 is different from that first proposed in Figure 7.7, where the MBA molecules are chemisorbed as opposed to being electrostatically bound to the gold nanorods layer. This structure was employed for the investigation of the SERS effects of 4-MBA bound to the gold nanorods. The ellipsometry results from the previous pH experiment showed that no benzoic acid was bound to the gold nanorods and for consistency in the analysis, the same slides were used to investigate the SERS effect on MBA.

A Raman spectra of each slide was taken prior to immersion in a 5 mL solution of 10 mM 4-MBA in toluene to measure the SERS background signal. The slide was then immersed into the 4-MBA solution for 1hr, rinsed with toluene, dried in a stream of argon and the Raman spectra was then measured. Figure 7.14 shows the SERS spectra of 4-MBA chemisorbed onto a sandwich geometry of MUA/gold nanorods where the nanorods were immobilised at the different pH's indicated. A dependence of the intensity of the SERS signal on the pH used to bind the gold nanorods electrostatically to the MUA SAM is evident. For comparison, the Raman spectra of solid 4-MBA is also shown. A plot of the relative intensities of

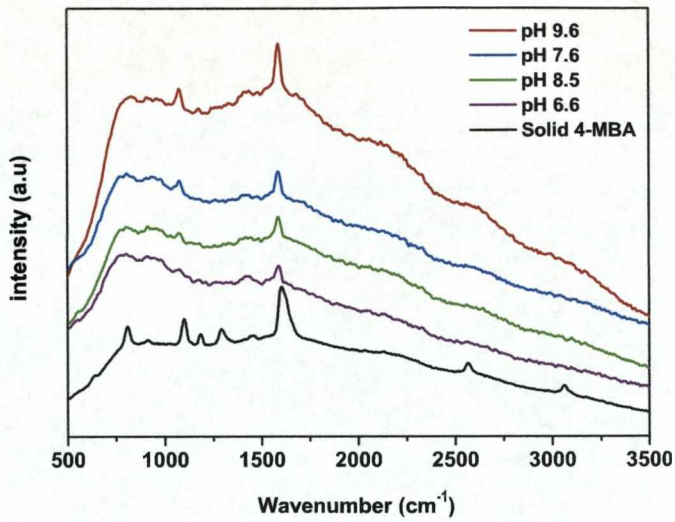


Figure 7.14: SERS spectra of 4-MBA immobilised on a sandwich structure of MUA/gold nanorods showing the effect of pH used to immobilise the gold nanorods on the intensity of the SERS signal.

the two aromatic ring vibration modes at ~1100 $cm^{-1}$ and ~1600 $cm^{-1}$ against pH is shown in Figure 7.15. The same trend for increasing thickness of the gold nanorod layer with increasing pH is also observed for the relative intensities of the SERS bands.

### 7.7.2 Sandwhich Geometry

Hu et al. [64] presented a new approach for the determination of SERS enhancement using a metal-molecule-metal sandwich architecture by the self-assembly of silver nanoparticles and gold nanorods interconnected with 4-aminothio phenol. Hu showed that this sandwich geometry produces enhancement factors of the order of $10^8$. This approach was investigated to see if a greater enhancement could be achieved.

A fresh gold film slide was coated with the MUA/gold NR/4-MBA structure following the procedure explained above using a pH of 9 for the immobilisation of the gold nanorods. The slide was then re-immersed for 2 hours into the gold

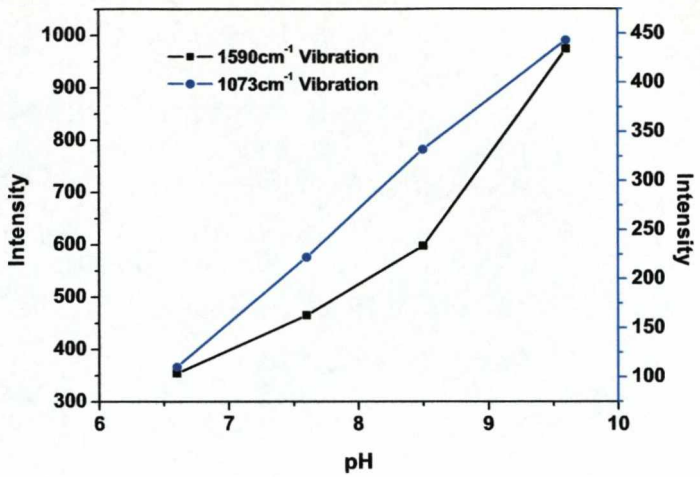


Figure 7.15: Dependance of the relative intensities of the observed SERS bands with respect to pH.

nanorod solution once again adjusting the pH to 9. By using a similar geometry of gold nanoparticles/4-ATP/gold dog bones, Hu observed a noticeable SERS enhancement when compared to the SERS spectra of 4-ATP on a monolayer of gold dogbones. Unfortunately, no further enhancement was observed using the sandwich structure described above. However, this approach was not studied in depth and further investigation would be required.

## 7.8 Summary

The preparation of a proposed sandwich structure geometry of gold nanorods for the investigation of the SERS active molecule 4-mercaptobenzoic acid (4-MBA) is described. The initial route employed the bifunctional linker molecules 1,9-diaminononanel and 1,9-nonanedithiol but both molecules failed to immobilise successfully gold nanorods by direct chemical bonding. Electrostatic immobilisation using the ionised form of a carboxylic linker molecule proved more successful

with the thickness of the bound nanorod layer being directly related to the pH of the solution employed. A proposed fully electrostatic sandwich geometry culminating in a SERS active 4-MBA layer being immobilised also proved unsuccessful although, a combination of both electrostatic immobilisation of the gold nanorods and chemisorption of the 4-MBA molecules resulted in a strong SERS signal being observed. The intensity of this signal was also found to be directly related to the thickness of the nanorods layer deposited and therefore, directly related to the pH used in the immobilisation stage of the gold nanorods.

# Chapter 8

# Conclusions and Proposal for Further Work

## 8.1 Conclusions

In order to investigate the use of non-spherical metallic nanoparticles as the base for a SERS substrate, the preparations of silver and gold nanorods have been carried out in two different ways in this Thesis, thorough a coupling of ultrasound to the electrochemically controlled nucleation and growth of metallic nuclei at an electrode surface and through a surfactant stabilised seed mediated wet chemical method.

In the sonoelectrochemical approach, two complex experimental configurations were designed. The first setup employed computer control of nucleation, growth and ultrasound conditions used in the formation of metallic nanoparticles in solution, whereas, in the second setup two waveform generators were employed to control the experimental conditions. It was observed that the latter approach proved successful in nanoparticle formation, whereas the former did not. Although the former allowed greater and more precise control over the experimental conditions used, the inherent instrumental delay when relaying these conditions to

the electrochemical cell meant the speed at which the experimental cycle could be repeated was compromised. In order to achieve a greater control over the size and density of the nuclei formed a double potential step pulse profile was employed. This allowed separate control of the nucleation and growth potentials along with their durations.

Prior to the attempted sonoelectrochemical formation of silver nanoparticles, the kinetics of electrodeposition of silver onto both platinum and glassy carbon, along with the influence of pulse parameters on current density in varying conditions were systematically studied by means of cyclic voltammetry and single/double potential step experiments. It was observed that changes in the potentials employed and their duration, along with analyte concentration, the addition of base electrolytes and different stabilising agents all caused significant changes in the type of nucleation occuring at the electrode surface. By simple addition of sodium perchlorate, a change from instantaneous to progressive nucleation was observed. Furthermore, with the addition of PVP to the silver salt solution a constant current in the current-time transients was observed indicating possible 1-D growth at the electrode surface instead of the 3-D hemispherical growth observed in the absence of this additive.

Based on the results of these experiments the growth of silver nuclei was coupled with a high intensity ultrasonic burst used to dislodge the growing nuclei from the electrode surface. A platinum working electrode was initially employed, but this was later replaced by a glassy carbon electrode due to the absence of strong metal interactions between the electrode and silver nuclei. Using this strategy and in solutions of high concentration, the use of the double potential pulse profile was successfully employed for the preparation of silver nanoparticles in solution. However, the use of a high concentration meant that the nanoparticles formed were unstable. For solutions at a lower concentration, more stable silver nanoparticles were synthesised. This approach employed an elegant double potential pulse

profile but proved unsuccessful and a constant potential applied throughout the entire pulse was finally used. Polyvinylpyrrolidone (PVP) was employed as a stabilising agent for the silver nanoparticles prepared by this route and its presence has a significant effect on the voltammetric behaviour of the system. By varying the concentration used a wide dispersions of shapes were formed with an optimum concentration of 10g/l producing both monodisperse silver nanoparticles and small aspect ratio nanorods.

By employing the same strategy used in the sonoelectrochemical formation of silver nanoparticles, the use of gold as a starting material has been also investigated in both acid and alkaline medium. Whereas nucleation and growth was observed in an alkaline medium, this was not observed under acid conditions. The reason for this is still unclear.

A series of CTAB stabilised gold nanorods have been synthesised by a seed mediated method. By varying the silver nitrate concentration within the growth solution and the amount of seed added a variety of different polydisperse sizes and aspect ratios were observed by TEM. The growth of the gold nanorods was followed by UV-Vis spectroscopy. It was observed that, during the initial stages of growth, the $\lambda_{max}$ of the longitudinal plasmon band increased, which was then followed by a subsequent decrease. This indicated that the gold nanorods initially elongate and then widen. Using a constant temperature of 40°C in the growth solution, more uniform nanorods of average length and width of (54±11) nm and (21±11) nm, respectively (average aspect ratio of 2.8±0.8) were prepared.

The synthesis of CTAB stabilised silver nanorods was attempted following a similar preparative route to that used in the formation of gold nanorods. By varying the concentration of silver seeds added to the growth solution the aspect ratio of the as-prepared silver nanorods could be controlled. This was observed by UV-Vis spectroscopy where a red shift in the $\lambda_{max}$ of the longitudinal plasmon band occurred with decreasing seed concentration. Although the absorption spectra for

each seed concentration showed two distinct plasmon resonances, TEM images of the solutions failed to show the presence of silver nanorods in high yield. As discussed in Chapter 3, there could be numerous reasons for this outcome; from an inadequate centrifugation separation stage to the greater instability of silver nanorods compared to those of gold.

The mechanism leading to anisotropic growth of silver and gold nanorods in a surfactant medium is still a matter of great debate. It has been proposed that an insoluble AgBr precursor plays a crucial role in the initial shape directed growth of the seeds added. To investigate this further, the growth of silver nanorods in the surfactant cetyltrimethylammonium nitrate was carried out. If indeed a silver-halide precursor was crucial for the shape directed growth of the silver seeds, then using CTAN should lead to the formation of soluble silver nitrate. When employing CTAN as the surfactant no nanorod formation was observed indicating that the presence of was $Br^-$ critical in the seed mediated growth of silver nanorods.

The effect of $Br^-$ concentration on the formation of silver nanorods was also investigated by the addition of KBr to the growth solution. As the total concentration of $Br^-$ was increased the disappearance of the longitudinal plasmon band of the nanoparticles prepared was observed by UV-Vis spectroscopy. It was calculated that the increase in the total concentration of $Br^-$ caused a large increase in the total concentration of free silver available in solution. Therefore, as the concentration of free silver in solution is increased, the formation of spherical particles is favoured. Although the data obtained from these sets of experiments cannot provide a mechanism for the anisotropic formation of silver nanorods, it does indicate that bromide is an essential component in their formation.

Finally, gold film slides were functionalised with gold nanorods to act as a subtrate for Surface Enhanced Raman Spectroscopy. The covalent attachment of the gold nanorods was initially investigated. Two molecules, 1-9,diaminononane (DAN) and 1-9,nonanedithiol (NDT) were employed as linkers between the nanords

and the gold surface, but no nanorod deposition was observed.

The electrostatic attachment of gold nanorods was then investigated. This was achieved through the interaction of the net positively charged gold nanorods, a direct consequence of the stabilising CTAB bilayer bound to the surface, and a SAM of the linker molecule 11-mercaptoundecanoic acid (MUA). The pH of the nanorod solution was adjusted to deprotonate the carboxylic group of the MUA to allow electrostatic attachment. The nanorod layer deposition was performed at pH 6.6, 7.6, 8.5 and 9.6 and the optical constants and thickness of each deposited layer was measured by ellipsometry. The Raman active molecule 4-mercaptobenzoic acid was covalently and not electrostatically bound to the nanorod layer. This was confirmed by the absence of the $\nu$(SH) band in the SERS spectra obtained. A linear increase in the SERS signal with the linear increase in the pH at which the gold nanorod layer was deposited was observed.

## 8.2 Further Work

The main section of the work carried out in this Thesis concentrated on the sonoelectrochemical synthesis of metallic nanoparticles. Although the technique described in the present work proved successful in this aim it was not through the approach initially proposed i.e., through the use of separate nucleation and growth potentials. Due to the complexity of the technique and the number of influencing factors which could affect the size and morphology of the products formed, such as the type of stabilising agents employed and the potentials and times at which the particles are nucleated and grown, more work is needed in order to investigate these in more detail.

Furthermore, the use of a sonotrode, i.e. a working electrode embedded into the tip of the ultrasonic horn, would be beneficial since this would increase the likelihood of the nucleated and growing particles to be removed from the electrode

surface.

Due to the obvious inconsistencies observed in the reproducible formation of silver nanorods in a high yield noted in this work, further studies should be performed to improve both the synthetic preparation and subsequent separation and isolation of the products obtained through centrifugation.

Another area worthy of further study would be the use of gold nanorods employing both the electrostatic and covalent bonding schemes described in Chapter 7 in both the formation of multilayers and in the formation of metal-molecule-metal sandwich architectures described by Hu et al [64] at different values of pH. The initial results obtained show good enhancement and if investigated further could prove beneficial for obtaining large SERS signals and for possible analytical applications.

# Bibliography


[1] Tong, L.; Zhao, Y.; Huff, T. B.; Hansen, M. N.; Wei, A.; Cheng, J. X. *Adv. Mater.* **2007**, *19*(20), 3136.

[2] Dipti, S. S.; Chung, U. C.; Kim, J. P.; Chung, W. S. *Phys. Status Solidi A* **2007**, *204*(12), 4174–4177.

[3] Sang, Y. M.; Li, F. S.; Gu, Q. B.; Liang, C. Z.; Chen, J. Q. *Desalination* **2008**, *223*(1-3), 349–360.

[4] Noguez, C. *Optical Materials* **2005**, *27*(7), 1204–1211.

[5] Faraday, M. *Philos. Trans.* **1857**, *147*, 145–181.

[6] Frens, G. *Nat. Phys. Sci.* **1973**, *241*(105), 20–22.

[7] Brust, M.; Walker, M.; Bethell, D.; Schiffrin, D. J.; Whyman, R. April **1994**, (7), 801–802.

[8] Camillone, N.; Chidsey, C. E. D.; Liu, G.; Scoles, G. *J. Chem. Phys.* **1993**, *98*(5), 4234–4245.

[9] Luedtke, W. D.; Landman, U. *J. Phys. Chem.* **1996**, *100*(32), 13323–13329.

[10] Templeton, A. C.; Wuelfing, M. P.; Murray, R. W. *Acc. Chem. Res.* **2000**, *33*(1), 27–36.

[11] Brust, M.; Fink, J.; Bethell, D.; Schiffrin, D. J.; Kiely, C. *Chem. Commum.* **1995**, (16), 1655–1656.

[12] Sauer, G.; Brehm, G.; Schneider, S.; Nielsch, K.; Wehrspohn, R. B.; Choi, J.; Hofmeister, H.; Gosele, U. *J. Appl. Phys.* **2002**, *91*(5), 3243–3247.

[13] Corish, J.; Obriain, C. D. *J. Mater. Sci.* **1971**, *6*(3), 252–&.

[14] Yu, Y. Y.; Chang, S. S.; Lee, C. L.; Wang, C. R. C. *J. Phys. Chem. B* **1997**, *101*(34), 6661–6664.

[15] Zhu, J. J.; Liao, X. H.; Zhao, X. N.; Chen, H. Y. *Mater. Lett.* **2001**, *49*(2), 91–95.

[16] Jin, R. C.; Cao, Y. W.; Mirkin, C. A.; Kelly, K. L.; Schatz, G. C.; Zheng, J. G. *Science* **2001**, *294*(5548), 1901–1903.

[17] He, R.; Qian, X. F.; Yin, J.; Zhu, Z. K. *Chem. Phys. Lett.* **2003**, *369*(3-4), 454–458.

[18] Jana, N. R.; Gearheart, L.; Murphy, C. J. *J. Phys. Chem. B* **2001**, *105*(19), 4065–4067.

[19] Jana, N. R.; Gearheart, L.; Murphy, C. J. *Adv. Mater.* **2001**, *13*(18), 1389–1393.

[20] Jana, N. R.; Gearheart, L.; Murphy, C. J. *Langmuir* **2001**, *17*(22), 6782–6786.

[21] Jana, N. R.; Gearheart, L.; Murphy, C. J. *Chem. Commun.* **2001**, (7), 617–618.

[22] Jana, N. R.; Gearheart, L.; Obare, S. O.; Murphy, C. J. *Langmuir* **2002**, *18*(3), 922–927.

[23] Murphy, C. J.; Jana, N. R. *Adv. Mater.* **2002**, *14*(1), 80–82.

[24] Orendorff, C. J.; Gearheart, L.; Jana, N. R.; Murphy, C. J. *Phys. Chem. Chem. Phys.* **2006**, *8*(1), 165–170.

[25] Delplancke, J. L.; Dille, J.; Reisse, J.; Long, G. J.; Mohan, A.; Grandjean, F. *Chem. Mater.* **2000**, *12*(4), 946–955.

[26] Murphy, C. J.; Gole, A. M.; Hunyadi, S. E.; Orendorff, C. J. *Inorg. Chem.* **2006**, *45*(19), 7544–7554.

[27] Gou, L. F.; Murphy, C. J. *Chem. Mater.* **2005**, *17*(14), 3668–3672.

[28] Sau, T. K.; Murphy, C. J. *J. Am. Chem. Soc.* **2004**, *126*(28), 8648–8649.

[29] Chen, S. H.; Fan, Z. Y.; Carroll, D. L. *J. Phys. Chem. B* **2002**, *106*(42), 10777–10781.

[30] Lu, L.; Kobayashi, A.; Tawa, K.; Ozaki, Y. *Chem. Mater.* **2006**, *18*(20), 4894–4901.

[31] Chen, S. H.; Carroll, D. L. *J. Phys. Chem. B* **2004**, *108*(18), 5500–5506.

[32] Chen, D. L.; Gao, L. *J. Cryst. Growth* **2004**, *264*(1-3), 216–222.

[33] Zhu, J. J.; Liao, X. H.; Chen, H. Y. *Mater. Res. Bull.* **2001**, *36*(9), 1687–1692.

[34] Gao, X. L.; Gu, G. H.; Hu, Z. S.; Guo, Y.; Fu, X.; Song, J. M. *Colloids Surf., A* **2005**, *254*(1-3), 57–61.

[35] Pillai, Z. S.; Kamat, P. V. *J. Phys. Chem. B* **2004**, *108*(3), 945–951.

[36] Mayya, K. S.; Schoeler, B.; Caruso, F. *Adv. Funct. Mater.* **2003**, *13*(3), 183–188.

[37] Gittins, D. I.; Caruso, F. *J. Phys. Chem. B* **2001**, *105*(29), 6846–6852.

[38] Slistan-Grijalva, A.; Herrera-Urbina, R.; Rivas-Silva, J. F.; Avalos-Borja, M.; Castillon-Barraza, F. F.; Posada-Amarillas, A. *Mater. Res. Bull.* **2008**, *43*(1), 90–96.

[39] Jiang, X.; Pileni, M. *Colloids Surf., A* **2007**, *295*(1-3), 228–232.

[40] Gao, J. X.; Bender, C. M.; Murphy, C. J. *Langmuir* **2003**, *19*(21), 9065–9070.

[41] Perez-Juste, J.; Liz-Marzan, L. M.; Carnie, S.; Chan, D. Y. C.; Mulvaney, P. *Adv. Funct. Mater.* **2004**, *14*(6), 571–579.

[42] Lee, G. J.; Shin, S. I.; Kim, Y. C.; Oh, S. G. *Mater. Chem. Phys.* **2004**, *84*(2-3), 197–204.

[43] Murphy, C. J.; San, T. K.; Gole, A. M.; Orendorff, C. J.; Gao, J. X.; Gou, L.; Hunyadi, S. E.; Li, T. *J. Phys. Chem. B* **2005**, *109*(29), 13857–13870.

[44] Nikoobakht, B.; El-Sayed, M. A. *Langmuir* **2001**, *17*(20), 6368–6374.

[45] Mie, G. *Ann. Phys.* **1908**, *25*, 377.

[46] Kelly, K. L.; Coronado, E.; Zhao, L. L.; Schatz, G. C. *J. Phys. Chem. B* **2003**, *107*(3), 668–677.

[47] Gans, R. *Ann. Phys.* **1915**, *47*, 270.

[48] Link, S.; El-Sayed, M. A. *Int Rev Phys Chem* **2000**, *19*(3), 409–453.

[49] Link, S.; Wang, Z. L.; El-Sayed, M. A. *J. Phys. Chem. B* **1999**, *103*(18), 3529–3533.

[50] Link, S.; El-Sayed, M. A. *J. Phys. Chem. B* **1999**, *103*(21), 4212–4217.

[51] Wang, Z. L.; Mohamed, M. B.; Link, S.; El-Sayed, M. A. *Surf. Sci.* **1999**, *440*(1-2), L809–L814.

[52] Link, S.; El-Sayed, M. A. *J. Phys. Chem. B* **1999**, *103*(40), 8410–8426.

[53] Link, S.; Mohamed, M. B.; El-Sayed, M. A. *J. Phys. Chem. B* **1999**, *103*(16), 3073–3077.

[54] Hanessian, S.; Grzyb, J. A.; Cengelli, F.; Juillerat-Jeanneret, L. *Bioorg. Med. Chem.* **2008**, *16*(6), 2921–2931.

[55] Tong, L.; Zhao, Y.; Huff, T. B.; Hansen, M. N.; Wei, A.; Cheng, J. X. *Adv. Mater.* **2007**, *19*(20), 3136–+.

[56] Lee, P. C.; Meisel, D. *J. Phys. Chem.* **1982**, *86*(17), 3391–3395.

[57] Kneipp, K.; Wang, Y.; Kneipp, H.; Perelman, L. T.; Itzkan, I.; Dasari, R.; Feld, M. S. *Phys. Rev. Lett.* **1997**, *78*(9), 1667–1670.

[58] Nie, S. M.; Emery, S. R. *Science* **1997**, *275*(5303), 1102–1106.

[59] Le Ru, E. C.; Etchegoin, P. G.; Meyer, M. *J. Chem. Phys.* **2006**, *125*(20), 204701.

[60] Moskovits, M.; Jeong, D. H.; Livneh, T.; Wu, Y. Y.; Stucky, G. D. *Isr. J. Chem.* **2006**, *46*(3), 283–291.

[61] Ruan, C. M.; Wang, W.; Gu, B. H. *J Raman Spectrosc* **2007**, *38*(5), 568–573.

[62] Vlckova, B.; Pavel, I.; Sladkova, M.; Siskova, K.; Slouf, M. *J. Mol. Struct.* **2007**, *834*, 42–47.

[63] Michota, A.; Bukowska, J. *J. Raman Spectrosc.* **2003**, *34*(1), 21–25.

[64] Hu, X.; Wang, T.; Wang, L.; Dong, S. *J. Phys. Chem. C* **2007**, *111*(19), 6962–6969.

[65] Nikoobakht, B.; Wang, J. P.; El-Sayed, M. A. *Chem. Phys. Lett.* **2002**, *366*(1-2), 17–23.

[66] Talley, C. E.; Jusinski, L.; Hollars, C. W.; Lane, S. M.; Huser, T. *Anal. Chem.* **2004**, *76*(23), 7064–7068.

[67] Vo-Dinh, T.; Allain, L. R.; Stokes, D. L. *J. Raman Spectrosc.* **2002**, *33*(7), 511–516.

[68] Mulvaney, S. P.; Musick, M. D.; Keating, C. D.; Natan, M. J. *Langmuir* **2003**, *19*(11), 4784–4790.

[69] Luo, J.; Maye, M. M.; Kariuki, N. N.; Wang, L. Y.; Njoki, P.; Lin, Y.; Schadt, M.; Naslund, H. R.; Zhong, C. J. *Catal. Today* **2005**, *99*(3-4), 291–297.

[70] Zhang, D. F.; Diao, P.; Liu, P.; Wang, J. Y.; Xiang, M.; Zhang, Q. *Acta Chimica Sinica* **2007**, *65*(21), 2370–2376.

[71] Tominaga, M.; Shimazoe, T.; Nagashima, M.; Kusuda, H.; Kubo, A.; Kuwahara, Y.; Taniguchi, I. *J. Electroanal. Chem.* **2006**, *590*(1), 37–46.

[72] Chen, C. Y.; Yang, P.; Lee, Y. S.; Lin, K. F. *J. Power Sources* **2005**, *141*(1), 24–29.

[73] Gidaspow, D.; Jiradilok, V. *J. Power Sources* **2007**, *166*(2), 400–410.

[74] Wang, Z. B.; Yin, G. P.; Lin, Y. G. *J. Power Sources* **2007**, *170*(2), 242–250.

[75] Jal, P. K.; Patel, S.; Mishra, B. *Talanta* **2004**, *62*(5), 1005–1028.

[76] Sondaghuethorst, J. A. M.; Schonenberger, C.; Fokkink, L. G. J. *J. Phys. Chem.* **1994**, *98*(27), 6826–6834.

[77] Hou, Z. Z.; Abbott, N. L.; Stroeve, P. *Langmuir* **1998**, *14*(12), 3287–3297.

[78] Base, T.; Bastl, Z.; Plzak, Z.; Grygar, T.; Plesek, J.; Carr, M. J.; Malina, V.; Subrt, J.; Bohacek, J.; Vecernikova, E.; Kriz, O. *Langmuir* **2005**, *21*(17), 7776–7785.

[79] Vercelli, B.; Zotti, G.; Berlin, A. *Chem. Mater.* **2007**, *19*(3), 443–452.

[80] Miao, Y. Q.; Chen, J. R.; Wu, X. H.; Fang, K. M. February **2007**, *14*(1), 111–115.

[81] Hu, X. G.; Cheng, W. L.; Wang, T.; Wang, Y. L.; Wang, E. K.; Dong, S. J. *J. Phys. Chem. B* **2005**, *109*(41), 19385–19389.

[82] Brust, M.; Bethell, D.; Kiely, C. J.; Schiffrin, D. J. *Langmuir* **1998**, *14*(19), 5425–5429.

[83] Feringa, B. L. *J. Org. Chem.* **2007**, *72*(18), 6635–6652.

[84] Suslick, K. S.; Didenko, Y.; Fang, M. M.; Hyeon, T.; Kolbeck, K. J.; McNamara, W. B.; Mdleleni, M. M.; Wong, M. *Philos. T. R. Soc. A* **1999**, *357*(1751), 335–353.

[85] Suslick, K. S.; Choe, S. B.; Cichowlas, A. A.; Grinstaff, M. W. *Nature* **1991**, *353*(6343), 414–416.

[86] Gedanken, A. *Ultrason. Sonochem.* **2004**, *11*(2), 47–55.

[87] He, Y. H.; Vinodgopal, K.; Ashokkumar, M.; Grieser, F. *Res. Chem. Intermed.* **2006**, *32*(8), 709–715.

[88] Zhang, G. H.; Guo, W. L.; Wang, X. K. *Mater. Res. Innovations* **2007**, *11*(4), 201–203.

[89] Li, S.; Wang, X. K.; Guo, W. L.; Wang, J. G. *Chin. J. Inorg. Chem* **2007**, *23*(10), 1824–1828.

[90] Pinkas, J.; Reichlova, V.; Zboril, R.; Moravec, Z.; Bezdicka, P.; Matejkova, J. *Ultrason. Sonochem.* **2008**, *15*(3), 257–264.

[91] Mancier, V.; Daltin, A. L.; Leclercq, D. *Ultrason. Sonochem.* **2008**, *15*(3), 157–163.

[92] Arami, H.; Mazloumi, M.; Khalifehzadeh, R.; Sadmezhaad, S. K. *Mater. Lett.* **2007**, *61*(23-24), 4559–4561.

[93] Ding, T.; Zhang, J. R.; Hong, J. M.; Zhu, J. J.; Chen, H. Y. *J. Cryst. Growth* **2004**, *260*(3-4), 527–531.

[94] Li, Q.; Ding, Y.; Shao, M. W.; Wu, J.; Yu, G. H.; Qian, Y. T. *Mater. Res. Bull.* **2003**, *38*(3), 539–543.

[95] Wang, G. Z.; Geng, B. Y.; Huang, X. M.; Wang, Y. W.; Li, G. H.; Zhang, L. D. *Appl. Phys. A: Mater. Sci. Process.* **2003**, *77*(7), 933–936.

[96] Behboudnia, M.; Azizianekalandaragh, Y. *Mater. Sci. Eng., B* **2007**, *138*(1), 65–68.

[97] Kristl, M.; Drofenik, M. *Ultrason. Sonochem.* **2008**, *15*(5), 695–699.

[98] Zhou, S. M.; Feng, Y. S.; Zhang, L. D. *Mater. Lett.* **2003**, *57*(19), 2936–2939.

[99] Qiu, L. H.; Pol, V. G.; Calderon-Moreno, J.; Gedanken, A. *Ultrason. Sonochem.* **2005**, *12*(4), 243–247.

[100] Katoh, R.; Tasaka, Y.; Sekreta, E.; Yumura, M.; Ikazaki, F.; Kakudate, Y.; Fujiwara, S. September **1999**, *6*(4), 185–187.

[101] Zhu, Y. C.; Li, H. L.; Koltypin, Y.; Hacohen, Y. R.; Gedanken, A. *Chem. Commum* **2001**, (24), 2616–2617.

[102] Wang, H.; Lu, Y. N.; Zhu, J. J.; Chen, H. Y. *Inorg. Chem.* **2003**, *42*(20), 6404–6411.

[103] Xiong, Y. J.; Xie, Y.; Du, G. O.; Liu, X. M.; Tian, X. B. *Chem. Lett.* **2002**, (1), 98–99.

[104] Hardcastle, J. L.; Compton, R. G. *Electroanalysis* **2002**, *14*(11), 753–759.

[105] Hardcastle, J. L.; Compton, R. G. *Analyst* **2001**, *126*(11), 2025–2031.

[106] Compton, R. G.; Eklund, J. C.; Marken, F.; Rebbitt, T. O.; Akkermans, R. P.; Waller, D. N. *Electrochim. Acta* **1997**, *42*(19), 2919–2927.

[107] Hyde, M. E.; Compton, R. G. *J. Electroanal. Chem.* **2002**, *531*(1), 19–24.

[108] Mastai, Y.; Polsky, R.; Koltypin, Y.; Gedanken, A.; Hodes, G. *J. Am. Chem. Soc.* **1999**, *121*(43), 10047–10052.

[109] Saez, V.; Gonzalez-Garcia, J.; Iniesta, J. D.; Frias-Ferrer, A.; Aldaz, A. *Electrochem. Commun.* **2004**, *6*(8), 757–761.

[110] Qiu, X. F.; Lou, Y. B.; Samia, A. C. S.; Devadoss, A.; Burgess, J. D.; Dayal, S.; Burda, C. *Angew. Chem., Int. Ed.* **2005**, *44*(36), 5855–5857.

[111] Zhu, J. J.; Qiu, Q. F.; Wang, H.; Zhang, J. R.; Zhu, J. M.; Chen, Z. Q. *Inorg. Chem. Commun.* **2002**, *5*(4), 242–244.

[112] Saterlay, A. J.; Compton, R. G. *J. Anal. Chem.* **2000**, *367*(4), 308–313.

[113] Yin, B. S.; Ma, H. Y.; Wang, S. Y.; Chen, S. H. *J. Phys. Chem. B* **2003**, *107*(34), 8898–8904.

[114] Jiang, L. P.; Wang, A. N.; Zhao, Y.; Zhang, J. R.; Zhu, J. J. *Inorg. Chem. Commun.* **2004**, *7*(4), 506–509.

[115] Durant, A.; Francois, H.; Reisse, J.; KirschDeMesmaeker, A. *Electrochim. Acta* **1996**, *41*(2), 277–284.

[116] Reisse, J.; Francois, H.; Vandercammen, J.; Fabre, O.; Kirschdemesmaeker, A.; Maerschalk, C.; Delplancke, J. L. *Electrochim. Acta* **1994**, *39*(1), 37–39.

[117] Marken, F.; Compton, R. G. *Ultrason. Sonochem.* **1996**, *3*(2), S131–S134.

[118] Hagan, C. R. S.; Coury, L. A. *Anal. Chem.* **1994**, *66*(3), 399–405.

[119] Eklund, J. C.; Marken, F.; Waller, D. N.; Compton, R. G. *Electrochim. Acta* **1996**, *41*(9), 1541–1547.

[120] Compton, R. G.; Eklund, J. C.; Marken, F.; Waller, D. N. *Electrochim. Acta* **1996**, *41*(2), 315–320.

[121] Bard, A.; Faulkner, L. *Electrochemical methods, fundamentals and applications;* Wiley, 1980.

[122] Holt, K. B.; Del Campo, J.; Foord, J. S.; Compton, R. G.; Marken, F. *J. Electroanal. Chem.* **2001**, *513*(2), 94–99.

[123] Gunawardena, G.; Hills, G.; Montenegro, I. *J. Electroanal. Chem.* **1982**, *138*(2), 241–254.

[124] Gunawardena, G.; Hills, G.; Montenegro, I.; Scharifker, B. *J. Electroanal. Chem.* **1982**, *138*(2), 255–271.

[125] Hills, G. J.; Schiffrin, D. J.; Thompson, J. *Electrochim. Acta* **1974**, *19*(11), 657–670.

[126] Serrano, K.; Taxil, P. *J. Appl. Electrochem.* **1999**, *29*(4), 505–510.

[127] Allongue, P.; Souteyrand, E. *J. Electroanal. Chem.* **1990**, *286*(1-2), 217–237.

[128] Tadano, A.; Aogaki, R. *J. Chem. Phys.* **1997**, *106*(14), 6146–6151.

[129] Trivino, G. C.; Garrido, V. L. *J. Chil. Chem. Soc.* **2007**, *52*(2), 1182–1185.

[130] Si, M. Z.; Fang, Y.; Dong, G.; Zhang, P. X. *Spectrosc. Spect. Anal.* **2008**, *28*(1), 117–120.

[131] Radziuk, D.; Shchukin, D.; Mohwald, H. *J. Phys. Chem. C* **2008**, *112*(7), 2462–2468.

[132] Zhang, J. H.; Liu, H. Y.; Zhan, P.; Wang, Z. L.; Ming, N. B. *Adv. Funct. Mater.* **2007**, *17*(9), 1558–1566.

[133] Mazur, M. *Electrochem. Commun.* **2004**, *6*(4), 400–403.

[134] Underwood, S.; Mulvaney, P. *Langmuir* **1994**, *10*(10), 3427–3430.

[135] Baum, T.; Bethell, D.; Brust, M.; Schiffrin, D. J. *Langmuir* **1999**, *15*(3), 866–871.

[136] Joo, S.; Muto, I.; Hara, N. *J. Electrochem. Soc.* **2008**, *155*(4), C154–C161.

[137] Fian, A.; Haase, A.; Stadlober, B.; Jakopic, G.; Matsko, N. B.; Grogger, W.; Leising, G. *Anal. Bioanal. Chem.* **2008**, *390*(6), 1455–1461.

[138] Li, Q. H.; Zhu, D. L.; Liu, W. J.; Liu, Y.; Ma, X. C. *Appl. Surf. Sci.* **2008**, *254*(10), 2922–2926.

[139] Johnson, P. B.; Christy, R. W. *Phys. Rev. B* **1972**, *6*(12), 4370–4379.

[140] Fleischm.M.; Hendra, P. J.; Mcquilla.Aj. *Chem. Phys. Lett.* **1974**, *26*(2), 163–166.

[141] Suzuki, M.; Nidome, Y.; Terasaki, N.; Inoue, K.; Kuwahara, Y.; Yamada, S. *Jpn. J. Appl. Phys 2* **2004**, *43*(4B), L554–L556.

[142] Emory, S. R.; Nie, S. M. *Anal. Chem.* **1997**, *69*(14), 2631–2635.

[143] Doering, W.; Nie, S. *J. Phys. Chem. B* **2002**, *106*(2), 311–317.

[144] Nie, S. M.; Emory, S. R. *Abstr. Pap. Am. Chem S.* **1997**, *213*, 177–PHYS.

[145] Nikoobakht, B.; El-Sayed, M. A. *J. Phys. Chem. A* **2003**, *107*(18), 3372–3378.

[146] Nikoobakht, B.; El-Sayed, M. A. *Chem. Mater.* **2003**, *15*(10), 1957–1962.

[147] Jiang, X.; Brioude, A.; Pileni, M. *Colloids Surf., A* **2006**, *277*, 201–206.

[148] Mostany, J.; Mozota, J.; Scharifker, B. R. *J. Electroanal. Chem.* **1984**, *177*(1-2), 25–37.

[149] Sau, T. K.; Murphy, C. J. *Langmuir* **2004**, *20*(15), 6414–6420.

[150] El-Sayed, M. A. *Acc. Chem. Res.* **2001**, *34*(4), 257–264.

[151] Park, H. J.; Ah, C. S.; Kim, W. J.; Choi, I. S.; Lee, K. P.; Yun, W. S. *J. Vac. Sci. Technol., A* **2006**, *24*(4), 1323–1326.

[152] Chen, S. H.; Carroll, D. L. *Nano Lett.* **2002**, *2*(9), 1003–1007.

[153] Chao, Y. W.; Zhou, Q.; Li, Y.; Yan, Y. R.; Wu, Y.; Zheng, J. W. *J. Phys. Chem. C* **2007**, *111*(45), 16990–16995.

[154] Caswell, K. K.; Wilson, J. N.; Bunz, U. H. F.; Murphy, C. J. *J. Am. Chem. Soc.* **2003**, *125*(46), 13914–13915.

[155] Smith, D. K.; Korgel, B. A. *Langmuir* **2008**, *24*(3), 644–649.

[156] Johnson, C. J.; Dujardin, E.; Davis, S. A.; Murphy, C. J.; Mann, S. *J. Mater. Chem.* **2002**, *12*(6), 1765–1770.

[157] Filankembo, A.; Giorgio, S.; Lisiecki, I.; Pileni, M. P. *J. Phys. Chem. B* **2003**, *107*(30), 7492–7500.

[158] Zheng, X. W.; Zhu, L. Y.; Yan, A. H.; Wang, X. J.; Xie, Y. *J. Colloid Interface Sci.* **2003**, *268*(2), 357–361.

[159] Kameo, A.; Suzuki, A.; Torigoe, K.; Esumi, K. *J. Colloid Interface Sci.* **2001**, *241*(1), 289–292.

[160] Jiang, N.; Li, P. X.; Wang, Y. L.; Wang, J. B.; Yan, H. K.; Thomas, R. K. *J. Colloid Interface Sci.* **2005**, *286*(2), 755–760.

[161] Kawasaki, H.; Nishimura, K.; Arakawa, R. *J. Phys. Chem. C.* **2007**, *111*(6), 2683–2690.

[162] Sillen, L. *Stability constants of metal-ion complexes;* Chemistry Society, London, 2nd ed ed., 1964.

[163] Quirion, F.; Magid, L. J. *J. Phys. Chem* **1986**, *90*(21), 5435–5441.

[164] Scharifker, B.; Hills, G. *Electrochim. Acta* **1983**, *28*(7), 879–889.

[165] Gunawardena, G.; Hills, G.; Montenegro, I.; Scharifker, B. *J. Electroanal. Chem.* **1982**, *138*(2), 225–239.

[166] Tsakova, V.; Milchev, A. *Electrochim. Acta* **1991**, *36*(7), 1151–1155.

[167] Matthijs, E.; Langerock, S.; Michailova, E.; Heerman, L. *J. Electroanal. Chem.* **2004**, *570*(1), 123–133.

[168] Ueda, M.; Dietz, H.; Anders, A.; Kneppe, H.; Meixner, A.; Plieth, W. *Electrochim. Acta* **2003**, *48*(17), 2539–2539.

[169] Sandmann, G.; Dietz, H.; Plieth, W. *J. Electroanal. Chem.* **2000**, *491*(1-2), 78–86.

[170] Scharifker, B. R.; Mostany, J. *J. Electroanal. Chem.* **1984**, *177*(1-2), 13–23.

[171] Tadano, A.; Aogaki, R. *J. Chem. Phys.* **1997**, *106*(14), 6126–6137.

[172] Gunawardena, G. A.; Hills, G. J.; Montenegro, I. *Electrochim. Acta* **1978**, *23*(8), 693–697.

[173] Avrami, M. *J. Chem. Phys.* **1939**, *7*(12), 1103–1112.

[174] Schiffrin, D. J. *J. Electroanal. Chem.* **1986**, *201*(1), 199–203.

[175] Harned, H. S.; Hildreth, C. L. *J. Am. Chem. Soc.* **1951**, *73*(7), 3292–3293.

[176] Fleischmann, M.; Thirsk, H. *Advances in Electrochemistry and Electrochemical Engineering*, Vol. 3; Wiley, 1963.

[177] Milchev, A.; Chierchie, T.; Juttner, K.; Lorenz, W. J. *Electrochim. Acta* **1987**, *32*(7), 1039–1042.

[178] Panda, S. K.; Chaudhuri, S. *Synth. React. Inorg. Me.* **2007**, *37*(6), 397–401.

[179] Kim, J. S. *J. Ind. Eng. Chem.* **2007**, *13*(4), 566–570.

[180] Wang, H. S.; Qiao, X. L.; Chen, J. G.; Wang, X. J.; Ding, S. Y. *Mater. Chem. Phys.* **2005**, *94*(2-3), 449–453.

[181] Wang, H. S.; Qiao, X. L.; Chen, J. G.; Ding, S. Y. *Colloids Surf., A* **2005**, *256*(2-3), 111–115.

[182] Zhang, J. H.; Liu, H. Y.; Wang, Z. L.; Ming, N. B. *Adv. Funct. Mater.* **2007**, *17*(16), 3295–3303.

[183] Wei, G. D.; Nan, C. W.; Deng, Y.; Lin, Y. H. *Chem. Mater.* **2003**, *15*(23), 4436–4441.

[184] Liu, S. W.; Huang, W. P.; Chen, S. G.; Avivi, S.; Gedanken, A. *J. Non-Cryst. Solids* **2001**, *283*(1-3), 231–236.

[185] Kapoor, S. *Langmuir* **1998**, *14*(5), 1021–1025.

[186] Zhang, Z. T.; Zhao, B.; Hu, L. M. *J. Solid State Chem.* **1996**, *121*(1), 105–110.

[187] Jin, R. C.; Cao, Y. C.; Hao, E. C.; Metraux, G. S.; Schatz, G. C.; Mirkin, C. A. October **2003**, *425*(6957), 487–490.

[188] Huang, S. X.; Ma, H. Y.; Zhang, X. K.; Yong, F. F.; Feng, X. L.; Pan, W.; Wang, X. N.; Wang, Y.; Chen, S. H. *J. Phys. Chem. B* **2005**, *109*(42), 19823–19830.

[189] Desic, M.; Popovic, M. M.; Obradovic, M. D.; Vracar, L. M.; Grgur, B. N. *J. Serb. Chem. Soc.* **2005**, *70*(2), 231–242.

[190] Ma, H.; Yin, B.; Wang, S.; Jiao, Y.; Pan, W.; Huang, S.; Chen, S.; Meng, F. *ChemPhysChem* **2004**, *5*(1), 68–75.

[191] Sun, Y. G.; Yin, Y. D.; Mayers, B. T.; Herricks, T.; Xia, Y. N. *Chem. Mater.* **2002**, *14*(11), 4736–4745.

[192] Jin, W. J.; Lee, H. K.; Jeong, E. H.; Park, W. H.; Youk, J. H. *Macromol. Rapid Commun.* **2005**, *26*(24), 1903–1907.

[193] Bregado-Gutierrez, J.; Saldivar-Garcia, A. J.; Lopez, H. F. *J. Appl. Polym. Sci.* **2008**, *107*(1), 45–53.

[194] Mrozek, M. F.; Wasileski, S. A.; Weaver, M. J. *J. Am. Chem. Soc.* **2001**, *123*(51), 12817–12825.

[195] Leopold, N.; Lendl, B. *J. Phys. Chem. B* **2003**, *107*(24), 5723–5727.

[196] Ni, F.; Cotton, T. M. *Anal. Chem.* **1986**, *58*(14), 3159–3163.

[197] Alsmeyer, Y. W.; Mccreery, R. L. *Anal. Chem.* **1991**, *63*(13), 1289–1295.

[198] Chen, H. J.; Wang, Y. L.; Qu, J. Y.; Dong, S. J. *J. Raman Spectrosc.* **2007**, *38*(11), 1444–1448.

[199] Jung, H. Y.; Park, Y. K.; Park, S.; Kim, S. K. *Anal. Chim. Acta* **2007**, *602*(2), 236–243.

[200] Yang, Y.; Shi, J. L.; Tanaka, T.; Nogami, M. *Langmuir* **2007**, *23*(24), 12042–12047.

[201] Sha, M. Y.; Xu, H.; Penn, S. G.; Cromer, R. *Nanomedicine* **2007**, *2*(5), 725–734.

[202] Maruyama, Y.; Futamata, M. *Chem. Phys. Lett.* **2007**, *448*(1-3), 93–98.

[203] Kambhampati, P.; Child, C. M.; Foster, M. C.; Campion, A. *J. Chem. Phys.* **1998**, *108*(12), 5013–5026.

[204] Xu, H.; Aizpurua, J.; Käll, M.; Apell, P. *Phys. Rev. E* **2000**, *62*(3), 4318–4324.

[205] Gersten, j. i. *J. Chem. Phys.* **1980**, *72*(10), 5779–5780.

[206] Zhu, J.; Liu, X. *Chem. Phys.* **2006**, *323*(2-3), 446–450.

[207] http://www.arrandee.com/.

[208] Bayati, M. *Electrocatalysis by Nanoparticles* PhD thesis, University of Liverpool, **2007**.

[209] Venkataraman, L.; Klare, J. E.; Tam, I. W.; Nuckolls, C.; Hybertsen, M. S.; Steigerwald, M. L. *Nano Lett.* **2006**, *6*(3), 458–462.

[210] Lide, D. R., Ed. *CRC Handbook of Chemistry and Physics, 82nd Edition.;* CRC Press, Boca Raton, 2001.

[211] Joo, S. W.; Han, S. W.; Kim, K. *J. Colloid Interface Sci.* **2001**, *240*(2), 391–399.

[212] Bain, C. D.; Evall, J.; Whitesides, G. M. *J. Am. Chem. Soc.* **1989**, *111*(18), 7155–7164.

[213] Wu, A. G.; Cheng, W. L.; Li, Z. A.; Jiang, J. G.; Wang, E. K. *Talanta* **2006**, *68*(3), 693–699.

[214] Orendorff, C.; Hankins, P.; Murphy, C. *Langmuir* **2005**, *21*(5), 2022–2026.

[215] Orendorff, C. J.; Gole, A.; Sau, T. K.; Murphy, C. J. *Anal. Chem.* **2005**, *77*(10), 3261–3266.

[216] Cros, E.; Planas, M.; Bardaj, E. *Lett. Pept. Sci.* **2002**, *9*(1), 1–4.

[217] Lee, S. B.; Kim, K.; Kim, M. S. *J. Raman Spectrosc.* **1991**, *22*(12), 811–817.

[218] Suh, J. S.; Kim, J. *J. Raman Spectrosc.* **1998**, *29*(2), 143–148.

[219] Gole, A.; Orendorff, C. J.; Murphy, C. J. *Langmuir* **2004**, *20*(17), 7117–7122.

[220] Pishko, M. V.; Revzin, A.; Simonian, A. L. *Sensors* **2002**, *2*(3), 79–90.